# A microcalorimetric study of concentration effects on the reaction entropy during Al- and Li- bulk deposition and of phase transitions during Li intercalation in graphite electrodes

Zur Erlangung des akademischen Grades eines

DOKTORS DER NATURWISSENSCHAFTEN

(Dr. rer. nat.)

von der Fakultät für Chemie und Biowissenschaften

des Karlsruher Instituts für Technologie (KIT)

genehmigte

Dissertation

von

Junjie Xu

| | |
|---|---|
| 1. Referent : | Prof. Dr. Rolf Schuster |
| 2. Referent : | Priv. Doz. Dr. Andreas-Neil Unterreiner |
| Tag der mündlichen Prüfung : | 18.10.2018 |

# Zusammenfassung

In der vorliegenden Arbeit wurde der Einfluss der Konzentration auf die Entropieänderung bei der elektrochemischen Abscheidung von Al und Li und die Interkalation von Lithium in Graphit untersucht. Die Messung der Wärmeentstehung erfolgte mittels elektrochemischer Mikrokalorimetrie unter inerten Bedingungen in einer Glovebox. Die reversibel ausgetauschte Wärme entspricht gerade der Entropieänderung des Systems bei der Reaktion und beinhaltet die Beiträge aller ablaufenden Prozesse.

Die Al Bulkabscheidung wurde in Aluminiumchlorid und 1-Butyl-3-methylimidazoliumchlorid (BMIMCl) mit unterschiedlichen Verhältnissen von $AlCl_3$ zu BMIMCl (von 1,1:1 bis 1,7:1) durchgeführt. Die Reaktionsentropie für die Aluminiumabscheidung betrug ca. $33\,\mathrm{J/(mol\,K)}$ für ein Verhältnis von $AlCl_3$ zu BMIMCl von 1,7:1. Eine positive Abscheidungsentropie bedeutet, dass die Arbeitselektrode sich während der Abscheidung abkühlt. Die Reaktionsentropie für die Aluminiumabscheidung nahm mit dem Verhältnis von $AlCl_3$ zu BMIMCl ab.

Die Lithiumabscheidung wurde aus 0,01 M, 0,1 M und 1 M Lösung von $LiPF_6$ in einer 1:1 Mischung aus Ethylencarbonat (EC) und Dimethylcarbonat (DMC) ($EC : DMC = 1 : 1$) als Elektrolyt durchgeführt. Die Peltierwärme nahm um 5 kJ/mol bei einer Verdünnung von 1:10 und um 10 kJ/mol bei einem Verdünnungsfaktor von 100 ab. Die gemessenen Variationen des Peltier-Koeffizienten können gut durch die Änderung der Entropie des solvatisierten $Li^+$ Ions bei Verdünnung erklärt werden.

Die Reaktionsentropie für die Lithiuminterkalation in Graphit wurde in Abhängigkeit vom Ladezustand der Graphitelektrode untersucht. Es wurde im Mittel ein linearer Zusammenhang zwischen dem Interkalationspotential und der Interkalationsentropie zwischen 0,3 V und 0,07 V gefunden. Der Proportionalitätsfaktor entsprach der Faraday-Konstante. Die reversible Wärme und die Reaktionsentropie für die Phasenübergänge der coexistierenden Stufenphasen in Graphit wurden bestimmt, was dem Beitrag der Reaktionsenthalpie während Phasenübergängen entspricht. Die Änderung der Reaktionsentropie wurde durch das Gittergasmodell beschrieben und kann als Mischungsentropie von Lithium in Graphit interpretiert werden.

Bei der Bildung von SEI-Schichten wurde eine Kälteentwicklung beobachtet, was auf die reversible Reaktionen schließen ließ, da eine irreversible Reaktion nur einen Erwärmungseffekt der Elektrode bewirken würde.

## Summary

The concentration effects on the reaction entropy of electrochemical Al and Li deposition and the reaction entropy of phase transition during lithium intercalation and deintercalation in graphite was studied. Using electrochemical microcalorimetry under inert conditions, we employed pulse measurements to obtain the molar heat and reaction entropy of these reactions.

The aluminium bulk deposition was conducted in aluminium chloride and 1-butyl-3-methylimidazolium chloride (BMIMCl) ionic liquids with different ratios of $AlCl_3$ to BMIMCl (from 1.1:1 to 1.7:1). The reaction entropy for aluminum deposition was about 33 J/(mol K) when the ratio of $AlCl_3$ to BMIMCl was 1.7:1. It demonstrated a cooling effect for aluminium deposition and a warming effect for aluminium dissolution. As the ratio of $AlCl_3$ to BMIMCl decreased, the reaction entropy for the aluminium deposition decreased.

The lithium deposition was conducted using 0.01 M, 0.1 M and 1 M $LiPF_6$ in ethylene carbonate (EC) and dimethyl carbonate (DMC) ($EC : DMC = 1 : 1$) as electrolyte. The corresponding Peltier coefficient was found to decrease by 5 kJ/mol when the dilution factor was 10 and by 10 kJ/mol when the dilution factor was about 100. The measured variations of the Peltier coefficient can be well explained by the change of entropy of the solvated $Li^+$ ion upon dilution.

The reaction entropy for lithium intercalation in graphite was measured at various state of charge. The reversible heat was found to change linearly on the average (between 0.3 V to 0.07 V). The slope for the curve of the reversible heat vs. open circuit voltage was close to the Faraday constant. The reversible heat and the reaction entropy for the phase transitions of the co-existing staged phases in graphite were determined, which corresponded to the contribution of reaction enthalpy during phase transitions. The change of reaction entropy was interpreted with a lattice-gas model and can be derived from the partial molar entropy of mixture for lithium in graphite.

During the formation of SEI layers, a cooling effect on the graphite electrode was found, which also indicated some reversible reactions were involved, since an irreversible reaction would only cause a warming effect of the working electrodes.

# Contents

# 1. Introduction and motivation

The demand of green and clean energy promotes the development of renewable energies, such as wind and solar energy. Yet, the discontinuous nature (at night or when the wind stops) of the renewable energy and the increasing use of portable devices provide an urgent need for the development of energy storage devices.

Batteries, which are widely used as energy storage devices, are composed of several cells that are usually combined to provide required voltage and capacity, respectively[1]. In each of the cells, there are a positive electrode, a negative one and a separator in between. An electrolyte solution containing dissociated salts is filled between the two electrodes to transfer the charge carriers[1]. Among the various developed battery systems, Li-based batteries, due to the high energy density and flexibility of design, accounted for 63% of worldwide sales values in portable batteries[2].

The reason for using a Li-based batteries technology is the fact that Li is the most electropositive ($-3.04$ V versus standard hydrogen electrode) as well as the lightest metal (equivalent weight: $46.94\,\mathrm{g/mol}$, specific gravity: $40.53\,\mathrm{g/cm^3}$), thus making the high energy density of the storage systems feasible.

Lithium-ion batteries, firstly produced by Sony as commercial rechargeable batteries[3], are currently the most widely used and investigated energy storage devices. The characteristic parameters for lithium-ion batteries are power/energy density (gravimetric and volumetric), cyclability, rate capability and safety[4]. There are many studies to improve these properties. Some studies focus on the improvement of the electrode materials and the understanding of their structure[5]. Other studies include the choosing of suitable electrolyte and the improving of batteries performance by adding binders and conductive additives[6, 7].

Due to safety considerations, pure lithium is usually replaced by carbonaceous materials as anode for lithium-ion batteries[8], with a general formula of $Li_xC_6$. Graphite is an important anode material for lithium-ion batteries because of the advantages of low voltage range, low cost and high reversible capacity (theoretical capacity: $372\,\mathrm{mA\,h/g}$)[9]. In lithium-ion batteries, ethylene carbonate (EC) and dimethyl carbonate (DMC) are used as solvent for the electrolyte ($LiPF_6$). Nevertheless, there could be side reactions of the graphite with the solvent of the electrolyte. In order to maximize the state of charge (x in $Li_xC_6$), the irreversible capacity loss due to the reaction between the graphite and the solvent should be minimized (i.e. the formation of the solid electrolyte interface

layer). Various factors, such as the properties of the electrode, temperature, current density, solvent and impurities, contribute to this irreversible process. To control irreversible processes, the understanding of electrode reaction is a prerequisite.

Beside the lithium-ion batteries, aluminium batteries are also a promising alternative due to its numerous advantages, e.g. low-cost, low-flammability, light weight and three-electron redox system reaction. Even though the gravimetric capacity of aluminum is very comparable to that of lithium (2.98 A h/g for Al vs. 3.86 A h/g for Li), the volumetric capacity of Al (8.04 A h/cm$^3$), is by a factor of three larger than that of Li[10]. However, Al is inapplicable as electrode in common electrolytes, because a repeatable deposition is hard to accomplish. Thus, ionic liquids were proposed as electrolyte for aluminium batteries based on the fact that the aluminium could be repetitively deposited and exfoliated in ionic liquids. Yet, most of the reports focus on the study of the structure and composition of the ionic liquids, using infrared spectroscopy[11, 12], Raman spectroscopy[13] and neutron diffraction[14].

In spite of the progress achieved for the development of lithium-ion and aluminium batteries, there are still open questions, such as safety problems and the insufficient capacity. To face these challenges and improve the battery performance, it is a prerequisite to understand the mechanism of the battery processes, such as the structure change of the electrode materials and the electrolyte or the mechanism of the electrode reaction. Since the entropy includes all side processes, such as coadsorption and ordering of the solvent (charge-neutral processes), it can provide complementary information to the current–potential relation, which will shed light on the mechanism of the electrochemical reaction. By combining electrochemical measurement and simulation, we can understand more about the battery system, which should be beneficial for the improvement of battery performance. Several groups have reported the measurement of heat flow during the electrode reaction with microcalorimetry. The thermal effects of charging and discharging of Ni-MH batteries (Nickel–metal hydride batteries) have been studied by Zhang *et al*[15], which showed a different heat dissipation between charging and discharging processes. Using isothermal microcalorimetry and operando X-ray absorption spectroscopy, Huie[16] demonstrated that the heat flow from the initial lithiation of $Fe_3O_4$ could be successfully modeled using only polarization and entropic contributions. A method of quantifying the parasitic heat flow during open circuit and voltage hold conditions was implemented using isothermal microcalorimetry on Li-ion pouch cells to investigate the effect of additives[17]. Hall[18] showed that isothermal microcalorimetry can be used in conjunction with electrochemical measurements to study solid–electrolyte interphase (SEI) formation reactions as they occur in a Li-ion cell. With isothermal microcalorimetry, by varying the current over narrow voltage ranges, the relative contributions of each of the heat flow sources (polarization, entropy and parasitic reactions) as a function of state of charge are determined for the $LiCoO_2$/graphite system[19]. Other thermodynamic stu-

dies using graphite as electrode in lithium-ion batteries focused on reproducing potential change with time and the temperature dependence of the open circuit voltage[20–22].

However, since the measurements should be conducted close to equilibrium and a high sensitivity is required, it is still challenging to determine the thermodynamic information (entropy, enthalpy and free enthalpy) of several processes, such as the phase transition, the change of ion pair and solvation shell during dilution. For example, excellent linearity in plots of molar heat vs. open circuit voltage of Li-graphite was demonstrated by Schmid[23]. But no information of phase transitions were exhibited because of the small contribution of enthalpy. Here, an electrochemical microcalorimeter (EMC), developed by our group, allowed us to in-situ measure the molar heat of electrode reactions with short pulses (10 ms long, corresponding to conversions in the submonolayer range) during electrochemical measurements. As an example, we applied this EMC method to determine the phase change during charging and discharging of Li-graphite batteries and the concentration effects on reaction entropy during lithium deposition and aluminium deposition.

Experiments on concentration effects on aluminium bulk deposition in ionic liquids were conducted to study the solvation of aluminium ions and the reaction mechanism. Lithium deposition in 1 M, 0.1 M, 0.01 M $LiPF_6$ in ethylene carbonate (EC) and dimethyl carbonate (DMC) ($EC : DMC = 1 : 1$) electrolyte was investigated to obtain the entropy of the solvated $Li^+$ ion upon dilution and to understand the influence of dilution on the formation of ion pairs. The reaction entropy for lithium intercalation in graphite electrode was measured at various states of charge. The change of reaction entropy during phase transitions was obtained. Thermal effect of the formation of SEI layers was determined.

# 2. Thermodynamics of electrochemical reactions

In the year 1821, Seebeck discovered the connection between temperature and electricity, the so-called thermoelectric effect[24]. In a closed circuit of two different metals, when there was a temperature difference, an electrical voltage was measured. An electromotive force of an order of millivolts was detected for a temperature difference of 100 K. The inverse character of this effect for the thermocouple (Lord Kelvin 1851) was confirmed through the discovery of Peltier-effect (in 1834), when the heat flow was $\dot{Q} = i\Pi_{AB}$ for a current of $i$ through the conductive pair AB, where $\Pi_{AB}$ is the Peltier coefficient[25].

Electrochemical reactions are accompanied by heat changes (endothermic or exothermic). Gibbs and Helmholtz investigated independently the electrical work and the entropy change during reaction in a full cell[26, 27]. The first theoretical explanation of electrochemical Peltier coefficient of a half cell implementing the ideas of Eastman on the transport of entropy due to ion migration was proposed by Wagner[28, 29], Monheim and Lange[30, 31]. Later, the theory was extended and summarized by several authors, such as References[32–34].

In terms of experimental research, Raoult and Thomsen[35, 36] determined the difference between the enthalpy and the electric work due to the entropy change of the reaction using calorimetry. Bouty[37] investigated the heat effect of a half cell for Cu deposition. Lange and Sherfey then determined the Peltier coefficient for several electrochemical reactions[38–40]. Based on the theoretical and experimental developments concerning the measurement of the Peltier coefficient (molar heat), microcalorimetry was used to determine the Peltier coefficient of electrochemical reactions, such as silver deposition[41] and lithium bulk deposition[42].

In this work, the sign convention for thermodynamic parameters, such as heat, work and entropy, will be considered from the perspective of the system. The sign will be denoted as positive when there is an increase of a thermodynamic parameter in the system, and vice versa. Section 2.1 is based on the textbook of Physical Chemistry[43]. The thermodynamic basis knowledge of Peltier coefficient in subsection 2.1.2 is based on the work of Agar[44] and the book by Bard[45] on the basis of electrochemical method and the chapter on Surface Microcalorimetry from the book on Surface and Interface Science (Volume 5 and 6) by Gottfried and Schuster[46].

## 2.1. Reversible heat

In a full cell, the enthalpy $H$ is defined as:

$$H = U + p \cdot V \tag{2.1}$$

The differential of $H$ follows that:

$$dH = dU + p \cdot dV + V \cdot dp \tag{2.2}$$

According to classic thermodynamic, the infinitesimal change of inner energy $dU$, absorbed heat $\delta Q$ and work $\delta W$ for a certain process correlates in the following equation:

$$dU = \delta Q + \delta W \tag{2.3}$$

In an electrochemical reaction, the work may include two parts: the volume work $W_{Vol}$ and the electric work $W_{El}$:

$$\delta W = \delta W_{Vol} + \delta W_{El} \tag{2.4}$$

According to the definition of work, the volume work can be obtained:

$$\delta W_{Vol} = -p \cdot dV \tag{2.5}$$

where $p$ symbolizes the pressure and $V$ the volume.

If we consider the former equations together, the differential of enthalpy correlates with the absorbed heat and the electric work in the following relation:

$$\delta Q = dH - \delta W_{El} \tag{2.6}$$

In a reversible reaction, the change of electric work equals to the differential of free enthalpy, as shown in the following expression:

$$\delta W_{El} = -z \cdot F \cdot dE_0 = dG \tag{2.7}$$

where $z$ is the number of electrons that are transferred during the reaction and $F$ is the Faraday constant. Considering the relation of free enthalpy with entropy and enthalpy $dG = dH - T \cdot dS$, we can conclude that the absorbed heat during a reversible reaction relates to the entropy in the following expression:

$$\delta Q = T \cdot dS \tag{2.8}$$

where $T$ is denoted as temperature and $dS$ the change of entropy during a reaction. Therefore, we can calculate the entropy for a reversible reaction as long as we obtain the exchanged heat.

For a half cell, we are interested in the reaction on the working electrode. For aluminium deposition and lithium deposition/intercalation, the reaction on the working electrode can be denoted in the following form:

$$M^{n+} + n\,e^- \longrightarrow M \tag{2.9}$$

The exchanged heat $\delta Q$ at an electrified junction of the working electrode and the electrolyte in this case correlates with the Peltier coefficient $\Pi$, which is named after French physicist Jean Peltier, in the following expression:

$$\delta Q = \Pi d\xi \tag{2.10}$$

where $\xi$ is the progress of reaction.

### 2.1.1. Potential dependence of reaction entropy

The zero-current cell potential $E_0$ at a certain anode composition is related to the free enthalpy for the cell reaction, according to the Equation (2.7). When the pressure of the cell is constant, the temperature coefficient $\partial E_0/\partial T$ correlates with the entropy in the following equation:

$$\left(\frac{\partial E_0}{\partial T}\right)_p = -\frac{\partial \Delta_R G}{zF \cdot \partial T} = \frac{-\partial \Delta_R H + T\partial \Delta_R S}{zF \cdot \partial T} \tag{2.11}$$

If the contribution of the enthalpy change can be neglected, the potential dependence of reaction entropy can be expressed by[22, 23, 47]:

$$\Delta E_0 \approx \frac{T \cdot \Delta \Delta_R S}{F} \tag{2.12}$$

where the $\Delta E_0$ is the change of open cell potential and $\Delta\Delta_R S$ is the change of reaction entropy.

### 2.1.2. Heat of transport and transport entropy

The change in entropy is caused by the transport of electrons and ions as well as by the transfer of heat $\delta Q$ from the surrounding to the interface volume. The heat transferred to the system during a reversible progress of the reaction is called Peltier coefficient, as shown in Equation (2.10). In an electrochemical cell, the electrode reaction is accompanied by the transport of charge carriers $i$. In a seminar paper, Eastman[49] demonstrated that

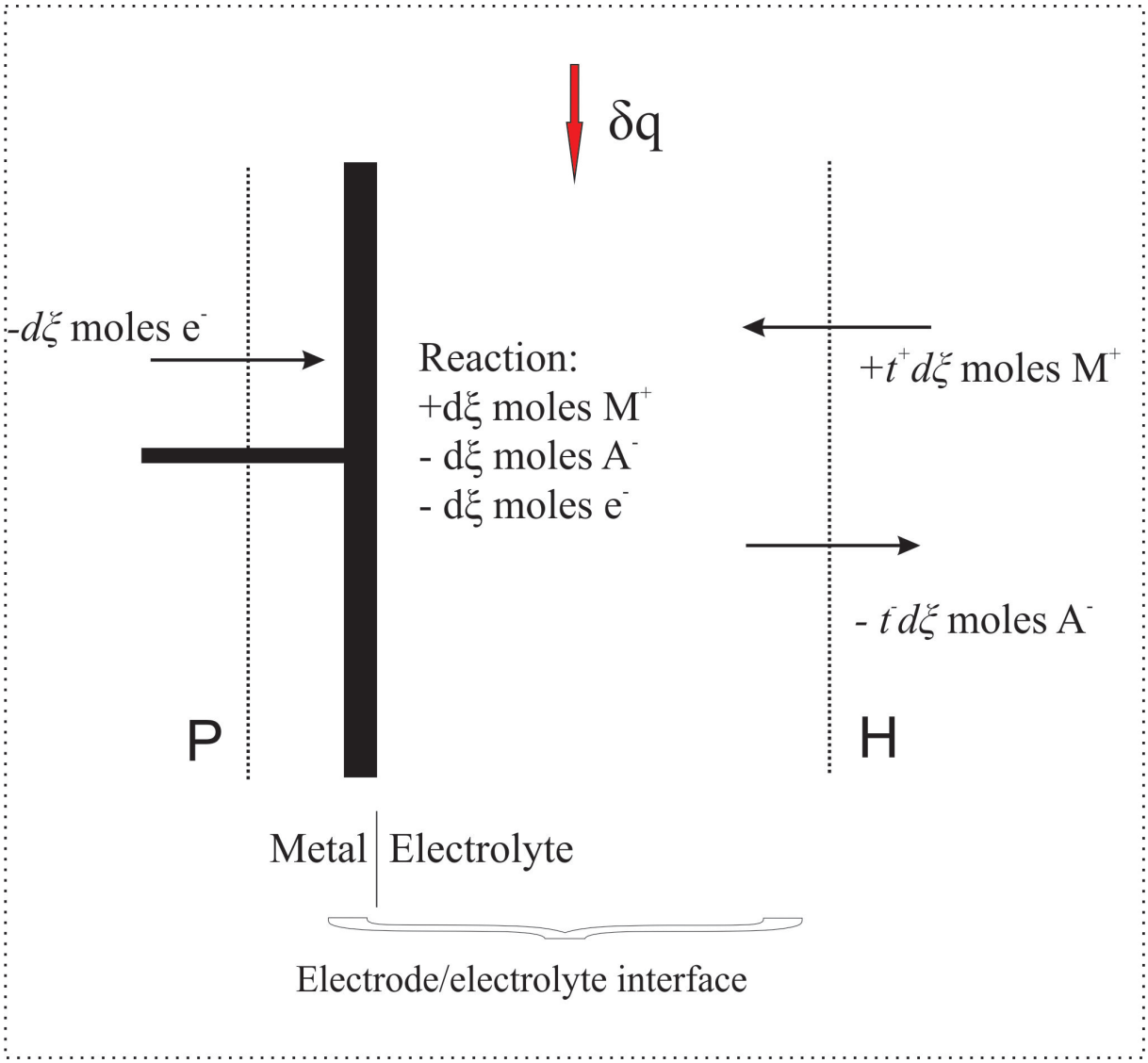


Figure 2.1. – Interface of a single electrode of metal M in an electrolyte of its salt ($M^+$, $A^-$). P and H denote the borders of the interface volume[48].

the transport of charge carriers correlates with the transport of heat, the so-called heat of transport $\hat{Q}_i$. The corresponding entropy change $\hat{s}_i = \hat{Q}_i/T$ is called Eastman's entropy of transfer, which should be added to the entropy change due to the molar entropy of conversion of the ion or electron $s_i$. When one mole of charge carrier $i$ is transported and has reacted, the corresponding entropy change is $\bar{\bar{S}}_i = \hat{s}_i + s_i$. $\bar{\bar{S}}_i$ is called transported entropy.

A summary of models for a physical reasoning for the transport of heat by charge carrier $i$ can be found in reference[46]. The heat of transport can be traced back to local thermal effects, which affect the structure and hydrogen-bond network of the surrounding solvent, such as water, beyond the first solvation shell of the ions. Ions can influence the entropy of the surrounding solvent and therefore cause structure-breaking or structure-making. When an ion is transported, the structural effects on the solvent are released behind and

built up ahead. The corresponding heat is absorbed ahead and liberated behind, which leads to transport of heat accompanying the transport of ions.

In a half cell with constant pressure and temperature, the heat of transport can be calculated according to the following considerations. Figure 2.1 shows a schematic structure of a half cell, where a wire of metal M is attached to an electrode of the same material. The electrolyte solution is composed of metal ions $M^+$ and $A^-$ ions. The reduction reaction (2.9) happens on the surface of the metal electrode.

The boundaries of the electrode-electrolyte interface are denoted as plane P and H. On the metal side, a plane P is at a fixed position of the wire, through which the electrons are provided to the electrode. On the solution side of the electrode, a plane H is chosen (Hittorf reference plane), which is sufficiently far from the electrode to symbolize the bulk properties of the electrolyte. To keep the net amount of solvent constant between the boundaries, the plane may move slightly under current flow. The current is assumed to be infinitesimally small to make the reaction (2.9) reversible.

After a progress of the reduction reaction by $\xi$, the thermodynamic state of the electrode-electrolyte interface changes accordingly: $d\xi$ moles of $M^+$ are reduced to M. Accordingly, through the Hittorf plane, $t^+ d\xi$ moles of $M^+$ are transported into the interface and $t^- d\xi$ moles of $A^-$ immigrate into the bulk of the electrolyte. $t^+$ and $t^-$ are the Hittorf transference numbers, which state how the current in the electrolyte is distributed between the ions, indicating different transferring ability of different ions. Since the net number of electrons in the metal side does not change, the entropy of the electrode-electrolyte interface volume can be expressed[44] by:

$$dS = (s_M - s_{M^+} + t^+ \cdot s_{M^+} - t^- \cdot s_{A^-} - s_{e^-})d\xi \tag{2.13}$$

where $s_M$, $s_{M^+}$ and $s_{A^-}$ denote the molar entropy of the metal and ions.

Following the former discussion on the transported entropy, the entropy change due to the transport of ions and electrons across the boundaries and due to transfer of heat can be expressed by[44]:

$$\begin{aligned} &(t^+ \cdot \bar{\bar{S}}_{M^+} - t^- \cdot \bar{\bar{S}}_{A^-} + \bar{\bar{S}}_{e^-})d\xi \\ =&(t^+(s_{M^+} + \hat{S}_{M^+}) - t^-(s_{A^-} + \hat{S}_{A^-}) + (s_{e^-} + \hat{S}_{e^-}))d\xi \end{aligned} \tag{2.14}$$

Since entropy is a state function, the entropy change in Equation (2.14) should be equal to the one derived from the change of state of the system in Equation (2.14). By combining Equation (2.13) and Equation (2.14), $\frac{\Pi}{T}$ is given[44, 46]:

$$\begin{aligned}\frac{\Pi}{T} &= (s_M - s_{M^+} - s_{e^-}) - (\hat{s}_{M^+} - \hat{s}_{A^-} + \hat{s}_{e^-}) \\ =&\Delta_R S - \frac{1}{T}(\hat{Q}_{M^+} - \hat{Q}_{A^-} + \hat{Q}_{e^-})\end{aligned} \tag{2.15}$$

$\Delta_R S = s_M - s_{M^+} - s_{e^-}$ corresponds to the molar entropy change of the half cell reaction. The Peltier coefficient is hence determined by considering both the molar entropy change of the electrochemical half cell reaction and the entropy change due to Eastman's entropy of transfer or the heat of transport of the charge carriers.

The heat of transport of different ions is listed in references[44, 50]. For non-aqueous solution, there is no literature value. However, it's possible to treat the ions as dielectric materials[44, 51] and provide an approximation for the heat of transport, as shown in the following expression:

$$\hat{Q} = -c_{SI}\left(\frac{e^2 \cdot z^2}{2 \cdot h \cdot \varepsilon}\frac{\partial ln\ \varepsilon}{\partial ln\ T}\right)\left(1 - \frac{r^s}{2 \cdot h}\right) \tag{2.16}$$

where $e$ is the elementary charge, $z$ the number of charge, $h$ the minimal distance between ion and solvent, $r^s$ the Stokes radius of the ions und $\varepsilon$ the relative permittivity. The constant $c_{SI}$ is about $4.3 \cdot 10^{31}$ $\mathrm{V\,m/(mol\,C)}$.

## 2.2. Irreversible heat

To measure the entropy of the electrochemical reaction, we should minimize the irreversible part. In the electrochemical reaction, the irreversible heat mainly comprises two parts: the Joule heat $\delta Q_{Joule}$ and the polarization heat due to the overpotential $\delta Q_{Pol}$. When a current $I$ flows in the electrolyte with a resistance $R$ for a time $dt$, the Joule heat is:

$$\delta Q_{Joule} = R \cdot I^2 \cdot dt \tag{2.17}$$

In order to conduct the reaction, an overpotential $\eta$ needs to be applied, which will cause the polarization of the interface, leading to a deviation from the equilibrium.

$$\delta Q_{Pol} = z \cdot F \cdot |\eta| \cdot d\xi \tag{2.18}$$

Here, $\xi$ is the reaction variable (progress of reaction).

Considering the reversible contribution $\delta Q_{rev}$ and the irreversible part $\delta Q_{irrev}$, the exchanged heat $\delta Q$ of a reaction can be written in the following form[52]:

$$\delta Q = \underbrace{T \cdot dS}_{\delta Q_{rev}} \underbrace{-I^2 \cdot R \cdot dt - z \cdot F \cdot |\eta| \cdot d\xi}_{\delta Q_{irrev}} \tag{2.19}$$

The Joule heat $\delta Q_{Joule}$ and the polarization heat cause the generating of heat in the system that is transferred to the surrounding. However, the use of very small currents reduce the Joule heat to negligibly small amount. The method of minimizing the influence of polarization will be discussed in the following chapters.

# 3. The experimental basis of electrochemical microcalorimetry

## 3.1. Electrochemical microcalorimetry

A microcalorimeter developed by our group[41, 53] makes it possible to obtain the molar heat (Peltier coefficient) at an electrode interface during an electrochemical reaction, with only monolayer or submonolayer conversion. In this work, the molar heat of the electrochemical reaction in aluminium and lithium half cells was measured via electrochemical microcalorimetry. According to chapter 2, the molar heat and the entropy of an electrochemical reaction can be determined. Since the entropy includes all side processes, such as coadsorption and ordering of the solvent, it can provide complementary information to the current–potential relation, which will shed light on the mechanism of the electrochemical reaction.

Electrochemical calorimeters have been used to determine the entropy for the deposition of metal by measuring the temperature change using a thermistor[33, 50]. By compensating the exchanged heat to keep the temperature unchanged, isothermal microcalorimetry was used to investigate some materials, e.g. the $LiNiCoO_2$ electrode[54]. For the application of electrochemical calorimetry in energy storage researches, Saito *et al.* studied commercial Li-ion batteries[55]. Kobayashi *et al.* investigated different combinations of graphite, lithium and $LiCoO_2$ as electrodes for a cell[56]. Maeda *et al.* studied the intercalation of lithium into graphite[57] and McKinnon *et al.* the intercalation of $Li_xMo_6Se_8$[58].

One difficulty for the study of surface and interface reactions is the small amount of reaction, which usually corresponds to the conversion of a few percent of a monolayer[23]. With the high sensitivity, the electrochemical microcalorimeter developed by our group provides access to the reaction entropy of an electrochemically stimulated surface process[59]. Using the electrochemical microcalorimeter, for example the under potential deposition (UPD) of Cu and Ag on gold surface was investigated[41, 53].

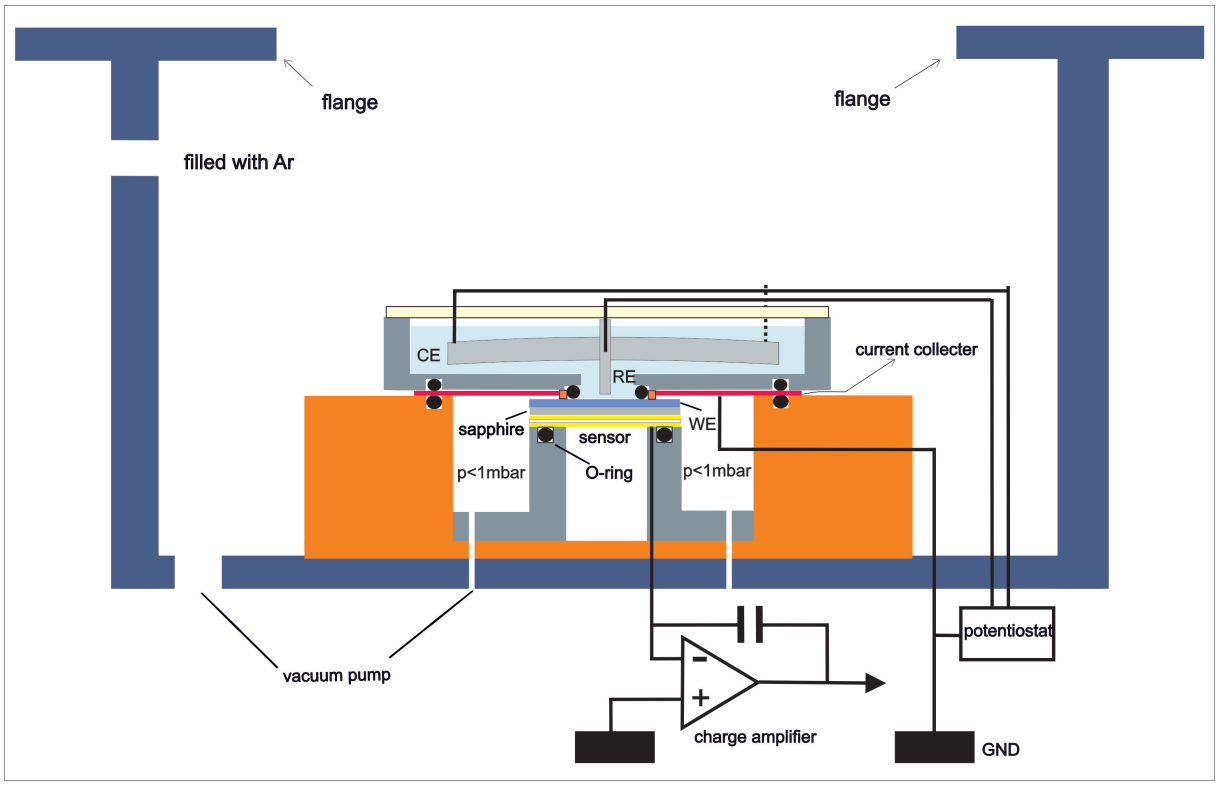


Figure 3.1. – Schematic figure of the electrochemical microcalorimeter.

## 3.2. Experimental setup

Figure 3.1 is a schematic figure to show the electrochemical microcalorimeter, which we used in our experiments. The setup was developed by our group[60]. It includes the following systems:

1) the vacuum: Two spaces needed to be evacuated. The first one was used to maintain the close contact between the sensor and working electrode so that most of the heat produced during the reaction on the working electrode could be transferred to the sensor. This was realized by a rotary vane pump (Leybold-Heraeus, Trivac D8B). The pressure could reach 0.1 mbar after evacuation for half an hour. This pump was kept running during the measurement. The second task was to evacuate the air when the flange of the apparatus was joined up to the glove box. Another rotary vane pump (Leybold-Heraeus, Trivac D8B) was applied for this purpose. Normally, it was evacuated for 10 h. Then the container was filled with pure Ar before connecting to the atmosphere of the glove box.

2) the sensor: The pyroelectric sensor was made of $LiTaO_3$ or PVDF. It could produce an electric signal due to temperature changes on the surface of the sensor. Even a small change of temperature, such as micro-Kelvin, could be detected. The sensor was coated with Au (200 nm for $LiTaO_3$ and 100 nm for PVDF) on both sides. Then it was connected to the charge amplifier on the one side and the grounding cable on the

other side using copper cable by soldering with field's metal (a kind of low melting temperature alloy). The soldered sensor was put on the polymer supporter with a O-ring (inner diameter: 5 mm; cord thickness: 1 mm) in between for buffering. A piece of sapphire sheet (8 mm x 8 mm x 50 µm) was put on the sensor to adjust the height. The sapphire had a larger thermal conductivity and specific heat than the sensor, thus there will be no obstacles for heat transfer between the working electrode and the sensor.

3) signal processing and recording: The electrodes were connected to a computer-controlled potentiostat, which allowed applying of current or potential pulses. The signal from the sensor due to the temperature change was amplified by a charge amplifier. The magnified signal was recorded through a National Instrument Card controlled by a procedure developed by our group in Igor Pro (Wavemetrics).

   We optimized the potentiostat and improved the procedure. Thousands of pulses (including potential, current and temperature transients) could be recorded in one measurement. A complete transient was 1 s long. When compressing, the procedure only fully recorded the first 100 ms of the transient and at the same times the whole transient was recorded with much lower sampling frequency. The average of the transient was obtained after reconstruction.

4) electrochemical cell: This part included the working electrode, current collector and cell. When assembling the cell, the working electrode was put on the sapphire sheet, with a copper circular ring (inner diameter: 6 mm) and a Viton O-Ring on it. In the next step, the current collector was put on the copper ring. The copper ring played the role of conductor between the sapphire sheet and the current collector. The cell was assembled on the current collector with an O-ring in between for sealing.

5) the container: The sensor and the assembled cell were mounted in the container. The container was used to protect the cell and connect it to the glove box.

### 3.2.1. PVDF sensor

Polyvinylidene difluoride (PVDF) foil, which is a pyroelectric material and was coated with a gold layer on both sides, was used as the temperature sensor in the microcalorimeter. With this microcalorimeter, it's feasible to measure the exchange of heat during reactions with submonolayer conversions, which are close to the thermal equilibrium. The PVDF is a kind of pyroelectric material, in which the change of temperature could change the state of electric polarization (electric dipole per unit volume). According to

reference[61, 62], the pyroelectric efficiency (p) correlates with the temperature (T) and electric displacement (D) as shown in the following equation:

$$p = \left(\frac{\partial D}{\partial T}\right)_{\sigma,E} \tag{3.1}$$

where $\sigma$ is stress and E is the electric field. The electric displacement could be denoted in the following equation:

$$D = \varepsilon_0 E(P_s + P_{induced}) \tag{3.2}$$

where $\varepsilon_0$ is the permittivity in vacuum, E is the electric field (here it equals to zero), $P_s$ and $P_{induced}$ are spontaneous polarization and induced polarization, respectively.

When we examine Equation (3.1) and Equation (3.2), we find that the change of temperature results in the change of polarization, which will change the dipole moment. To compensate the change of the dipole moment, charges on the surface of the PVDF sensor will redistribute, which will cause the flow of charges if it is short circuited[61]. Thus, the change of temperature of the PVDF sensor could be detected by amplifying the current. The coating layers on the surface of the PVDF act as current collector. According to Equation (3.1), the PVDF sensor is sensitive to mechanical stress. Since the thermal contact between the sensor and the working electrode was not constant after each assembling of the cell, a calibration had to be conducted in each experiment.

### 3.2.2. Lithium tantalate pyroelectric sensor

Lithium tantalate ($LiTaO_3$), which is a kind of pyroelectric material, responds to the temperature change by current flow due to electric polarization (electric dipole per unit volume). Therefore, in this work, a thin $LiTaO_3$ crystal, with a gold layer on both sides, was used as temperature sensor in the microcalorimeter. With this pyroelectric detector, it's feasible to measure the change of temperature during the reaction with submonolayer conversions, i.e. the system remains close to thermal equilibrium. According to References[63, 64], the relation between pyroelectric current $I_{pyro}$ and the pyroelectric coefficient (p) (the polarization change dP with the rate of the temperature change T) was denoted in the following equation:

$$I_{pyro} = A_s \frac{dP}{dT} \times \frac{d\Delta T_s}{dt} = pA_s \frac{d\Delta T_s}{dt} \tag{3.3}$$

where $A_s$ is the area and $d\Delta T_s/dt$ the rate of temperature change. Thus, a tiny change of temperature on the surface of the $LiTaO_3$ sensor can be detected when the current was amplified by the charge amplifier. In this work, with the help of an improved charge

amplifier and potentiostat, the sensitivity of the $LiTaO_3$ sensor was greater than that of the PVDF sensor.

## 3.3. Experimental procedures

The experiments, which were sensitive to $O_2$ and $H_2O$, were conducted inside a glove box ($O_2 < 4\ ppm$; $H_2O < 0.5\ ppm$). With the high sensitivity of the sensor, we were able to measure tiny amount of heat of about $10^{-5}$ K. In order to acquire the molar heat (Peltier coefficient) and entropy, it is necessary to ensure the short reaction and tiny conversion so that the reversible reaction is conducted close to equilibrium[43]. Furthermore, it's also important to minimize heat loss due to transfer heat to the electrolyte in order to study the reaction that happens on the surface of working electrode. Since the thermal conductivity of the WE (W, Ni, graphite) and the sapphire sheet is more than 100 times larger than that of the electrolyte, the heat transfer to the electrolyte can be neglected[23].

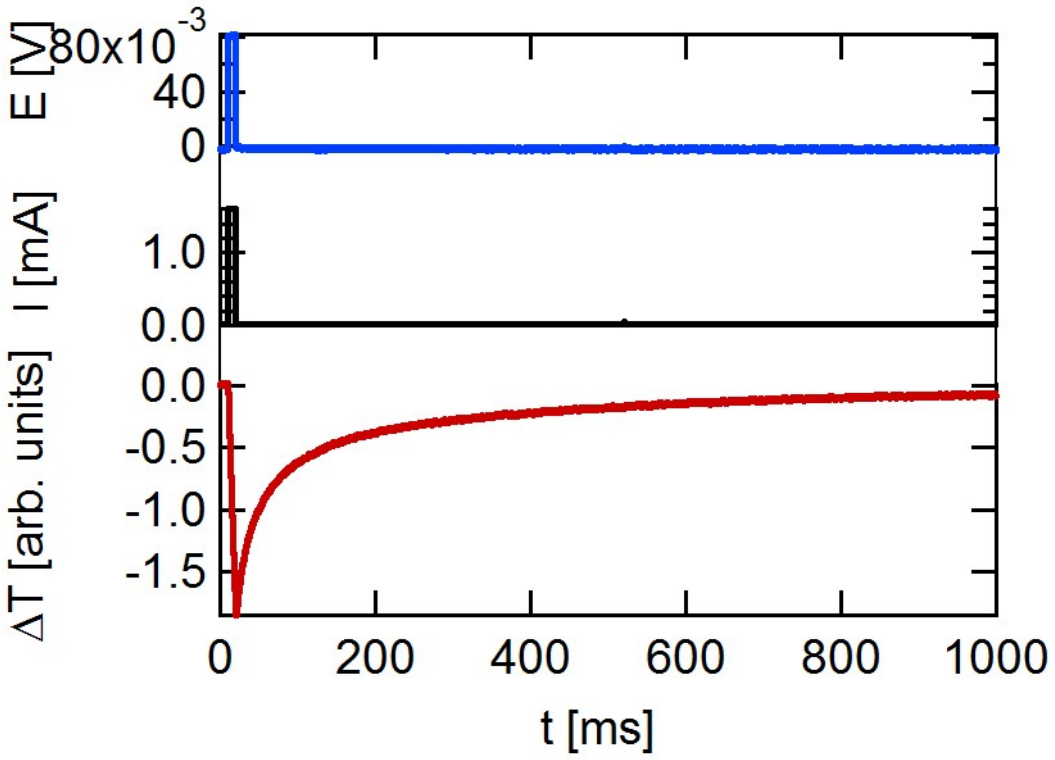


Figure 3.2. – Typical potential pulse including transients of potential (top, blue), current (middle, black) and temperature (bottom,red) applied with positive overpotential using Ni as working electrode, platinum as RE and CE electrode and 0.1 M $K_3[Fe(CN)_6]$ / $K_4[Fe(CN)_6]$ as electrolyte.

As an example we show a typical heat measurement for the calibration reaction. According to Equation (2.19) in chapter 2, potential pulses with increasing overpotentials were

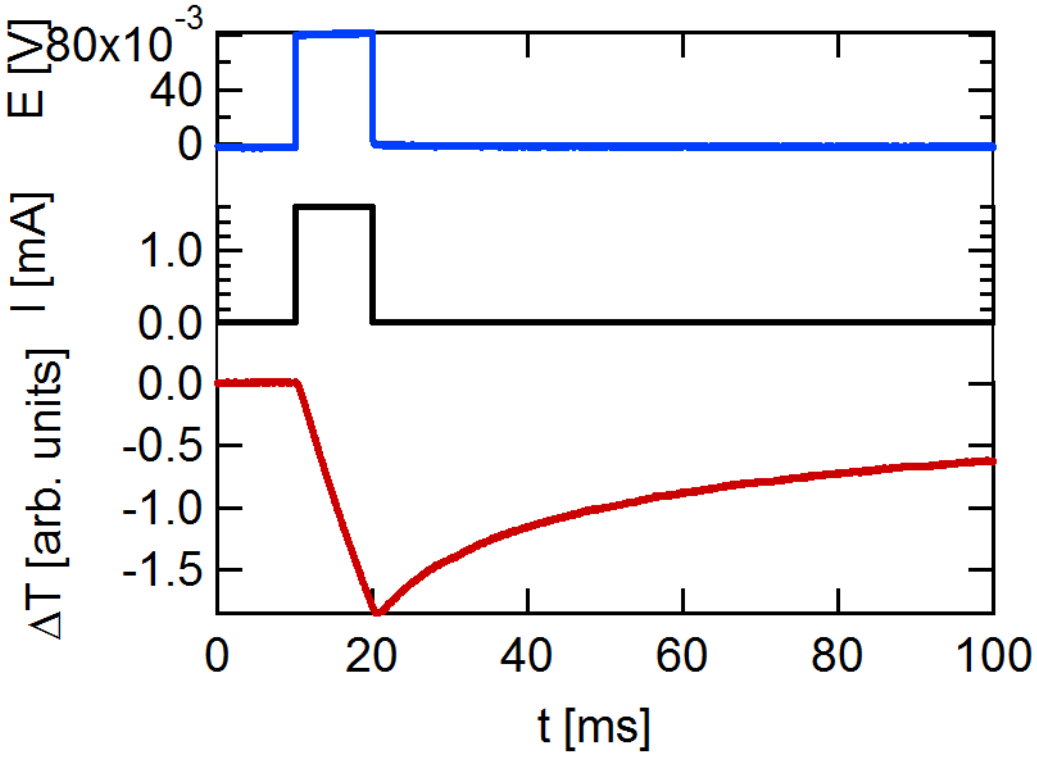


Figure 3.3. – Enlarged version of a typical potential pulse including transients of potential (top, blue), current (middle, black) and temperature (bottom,red) with positive overpotential using Ni as working electrode, platinum as RE and CE electrode and 0.1 M $K_3[Fe(CN)_6]$ / $K_4[Fe(CN)_6]$ as electrolyte.

applied to obtain the molar heat of the calibration reaction. A typical pulse, including potential, current and temperature transients for the calibration reaction is shown in Figure 3.2. The corresponding curve up to 100 ms can be seen in Figure 3.3. Potential pulses with an amplitude of 80 mV were applied between the time $t = 10\ ms$ and $t = 20\ ms$, which induced a current of 1.6 mA and a pulse heat of -1.7 in arbitrary unit (a.u.). Then the cell was switched to open cell potential by electronic interruption. With this cutoff, the potential returned to the equilibrium potential. The temperature changed simultaneously as shown in Figure 3.2 and Figure 3.3. At the end of the pulse ($t = 20\ ms$), with only a small delayed heat evolution (1 or 2 $ms$), the temperature transient started to relax to the thermal equilibrium. When the time came close to one second, the temperature transient returned to about the starting temperature, as shown the temperature transient in Figure 3.2. We waited at least 10 seconds before applying the next pulse. The charge, which flowed during the potential pulse, could be obtained by integrating the current transient. From the amplitude of the temperature and charge, reached at the end of the potential pulse, we can determine the amount of evolved heat. Dividing the pulse heat by the integrated charge, we got the normalized heat. However, the heat value of the reaction from the temperature transient is in arbitrary unit. In order to obtain the molar

heat of the electrochemical reaction, it is required to compare the molar heat with other reactions for which the Peltier coefficient is well known (i.e. the calibration reaction).

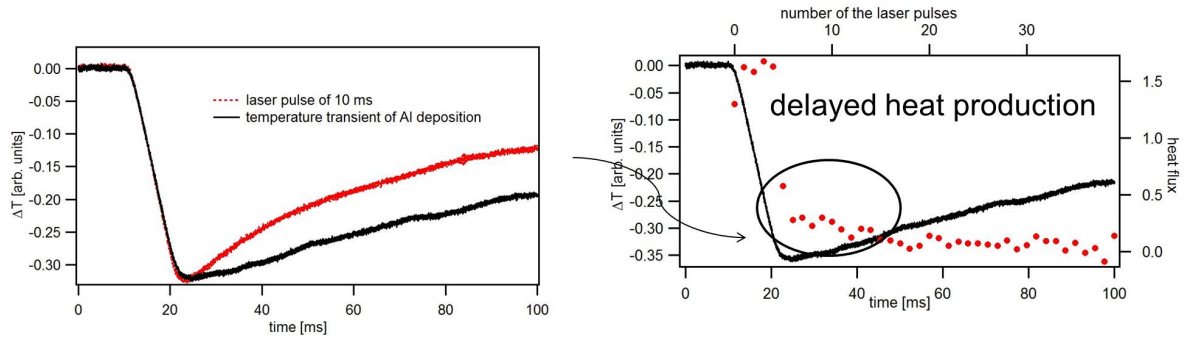


Figure 3.4. – The delayed heat evolution is shown by comparing a 10 ms laser pulse and the temperature transient of Al dissolution (left). To calculated the delayed heat evolution, 40 laser pulses (2 ms long) were used for fitting (right).

In addition, there usually is delayed heat evolution after the stop of the current flow at $t = 20\ ms$, as shown in Figure 3.4. The left part in Figure 3.4 shows the comparison between the temperature transient during Al dissolution and a 10 ms laser pulse. It demonstrates that the temperature change due to the laser pulse relaxed faster than that due to Al dissolution. To determine the exchanged heat, we used 2 ms long pulses to fit the temperature transient. As shown in the right part of Figure 3.4, the heat flow retrieved from the temperature transient by fitting was not zero from the sixth to the sixteenth point, which confirms the presence of delayed heat evolution between 20 ms and about 50 ms. This heat should be included when we calculate the normalized heat. The fitting procedure is described in detail in Reference [60].

Therefore, there are three necessary steps in an experiment: calibration, measurement of the electrochemical reaction under study and fitting of the temperature transients with the thermal response of laser pulses to retrieve the heat flow. The fitting is usually performed at the end of the experiment. But the sequence of calibration depends on the electrochemical reaction.

### 3.3.1. Calibration

As mentioned, the charge transferred through the sensor is proportional to the exchanged heat due to reaction. The corresponding proportional constant has to be determined by an experiment, the calibration reaction. A calibration reaction is usually a well studied reaction for which the molar heat is well known. The calibration reaction depends on the system which we investigate.

According to the electrolyte in the calibration reaction, the calibration can be categorized:

1) Calibration reaction with aqueous solution as electrolyte

2) Calibration reaction with nonaqueous solution as electrolyte

### Calibration with aqueous solution

For the experiment of lithium deposition and aluminium deposition, the electron transfer reaction in 0.1 M $K_3[Fe(CN)_6]$ / $K_4[Fe(CN)_6]$ aqueous solution was performed under ambient conditions as calibration reaction. The reaction of the $K_3[Fe(CN)_6]$ / $K_4[Fe(CN)_6]$ redox pair is well studied and the Peltier coefficient of this reaction is known in literature[32]. For both the lithium deposition and aluminium deposition, the calibration needed to be conducted in the beginning, because the surface of the working electrode would be irreversibly changed after the formation of the SEI layer or the decomposition of ionic liquids during the metal deposition reaction.

For calibration with aqueous solution, platinum was used as reference (RE) and counter electrode (CE), because platinum doesn't react with the electrolyte and provides a stable reference potential. A metal foil, such as gold, tungsten or nickel can be used as working electrode (WE), since the electron transfer reaction in $K_3[Fe(CN)_6]$ / $K_4[Fe(CN)_6]$ aqueous solution can be conducted on these metal surface. The active electrode area of the nickel or tungsten sheet, which served as working electrode, was about 0.2 $cm^2$. The cell was made from polychlorotrifluoroethylene (PCTFE, also known as KEL-F®). The working electrode (W or Ni) was cleaned with sand paper to remove the oxide layer on the surface and then rinsed with ultra pure water and acetone[65] for three times, respectively.

The cyclic voltammogram (CV) for the electron transfer reaction in 0.1 M $K_3[Fe(CN)_6]$ / $K_4[Fe(CN)_6]$ aqueous solution was scanned between −0.4 V and 0.4 V. On Ni working electrode, the CV curve started from ca. 0 V, which was the open cell potential (ca. −0.8 mV vs Pt reference electrode), and was scanned towards the positive direction, as shown in Figure 3.5. The oxidation peak appeared at 0.25 V and the reduction peak at −0.25 V. The reduction peak broadened slightly probably because of the oxide layer on the surface of the working electrode (Ni). After the Ni WE was polished, a narrow reduction peak could be obtained and the CV demonstrated good reproducibility between the second and the third cycles, as shown in Figure 3.6.

When Au was used as working electrode, no oxide layer was expected on the surface of the WE. In comparison with the CV for calibration on Ni, the reduction and oxidation peak of $K_3[Fe(CN)_6]$ / $K_4[Fe(CN)_6]$ electron transfer reaction appeared at a similar potential, respectively. However, the maximal current density for the reduction peak was about −20 $mA/cm^2$, which was stronger than that for calibration on Ni (−12 $mA/cm^2$). As shown in Figure 3.7, the CV for the reaction of $K_3[Fe(CN)_6]$ / $K_4[Fe(CN)_6]$ redox pair demonstrated a narrow reduction peak (at −0.2 mV). From the CV, we found better reproducibility for the calibration reaction on Au compared with that on Ni (WE).

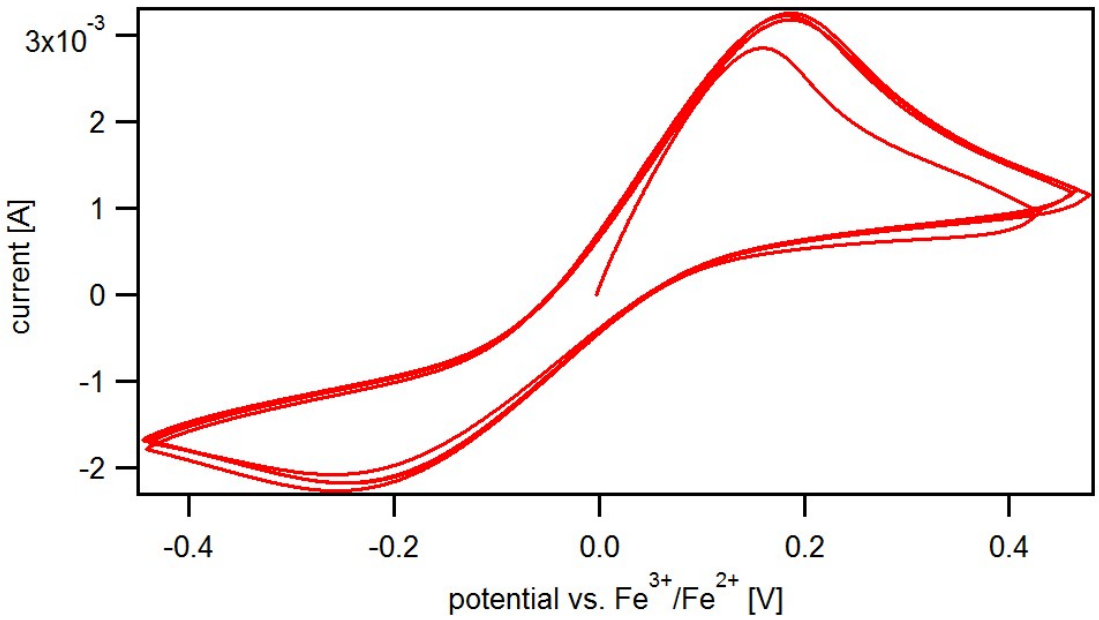


Figure 3.5. – The cyclic voltammogram for calibration using platinum as RE and CE electrode and 0.1 M $K_3[Fe(CN)_6]$ / $K_4[Fe(CN)_6]$ as electrolyte on insufficiently polished Ni working electrode. The CV was recorded, starting from 0 V, which was repetitively scanned between -0.4 V and 0.4 V. The scan speed was 50 mV/s.

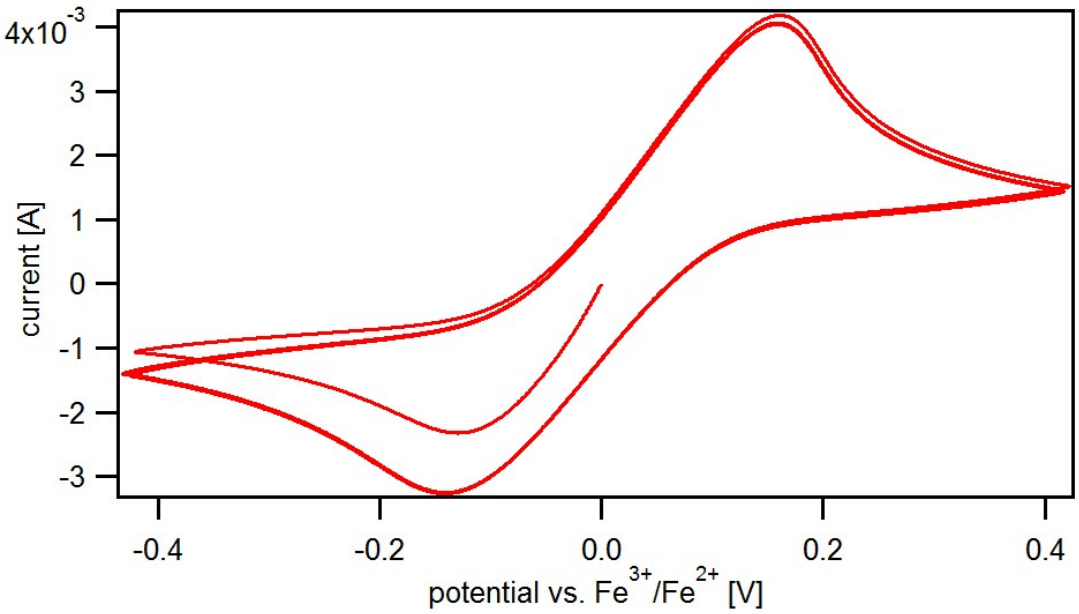


Figure 3.6. – The cyclic voltammogram for calibration on sufficiently polished Ni working electrode with platinum as RE and CE electrode and 0.1 M $K_3[Fe(CN)_6]$ / $K_4[Fe(CN)_6]$ as electrolyte. The CV was recorded, starting from 0 V, which was repetitively scanned between -0.4 V and 0.4 V. The scan speed was 50 mV/s

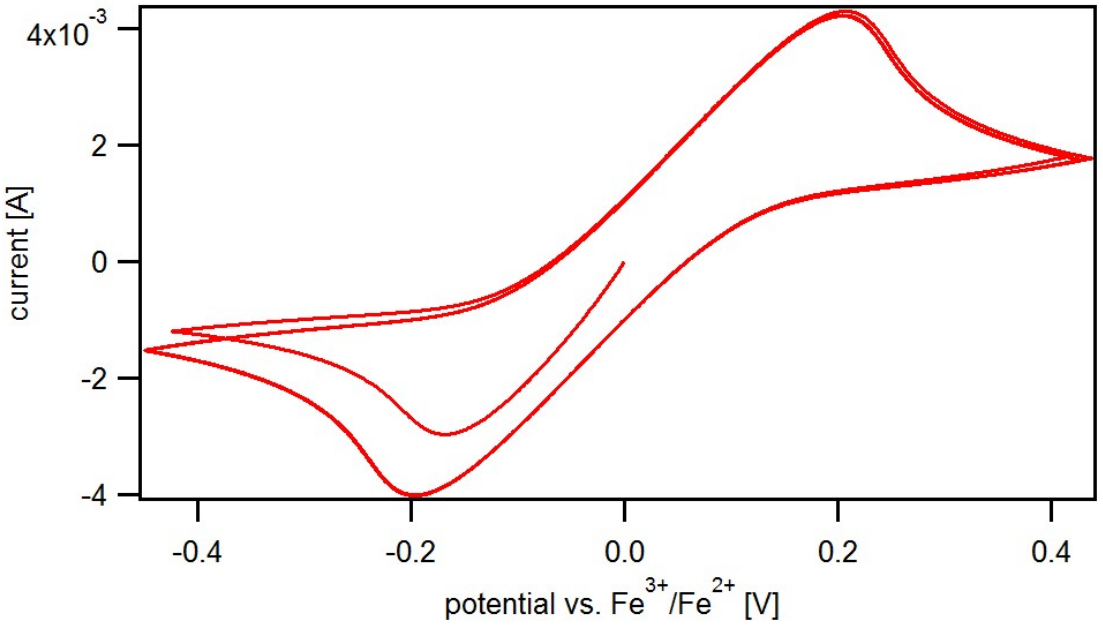


Figure 3.7. – The cyclic voltammogram for the calibration on a Au working electrode with platinum as RE and CE electrode and 0.1 M $K_3[Fe(CN)_6]$ / $K_4[Fe(CN)_6]$ as electrolyte. The CV was recorded, starting from 0 V, which was repetitively scanned between -0.4 V and 0.4 V.

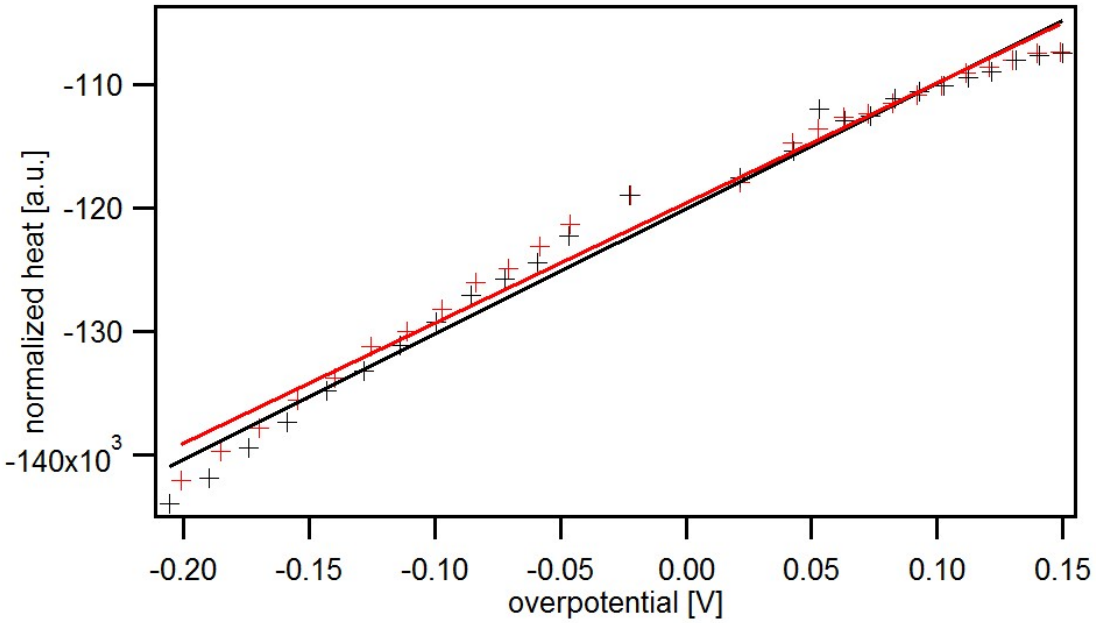


Figure 3.8. – The normalized heat for the calibration reaction on an insufficiently polished Ni working electrode with platinum as RE and CE electrode and 0.1 M $K_3[Fe(CN)_6]$ / $K_4[Fe(CN)_6]$ as electrolyte.

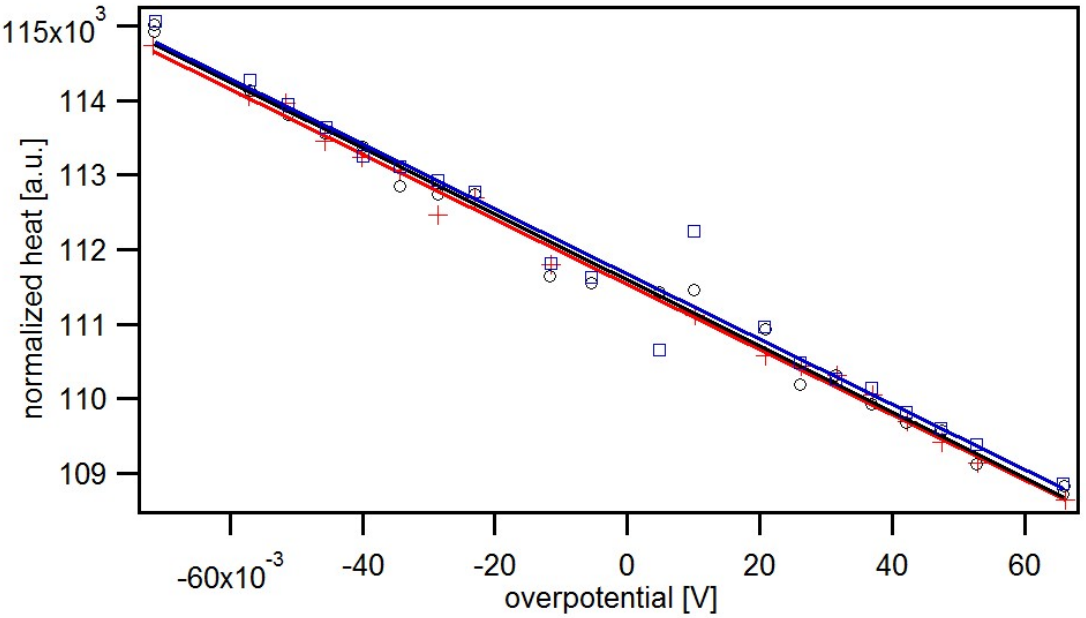


Figure 3.9. – The normalized heat for the calibration on sufficiently polished Ni working electrode with platinum as RE and CE electrode and 0.1 M $K_3[Fe(CN)_6]$ / $K_4[Fe(CN)_6]$ as electrolyte.

The influence of an oxide layer on the WE on the results for the normalized heat was examined. As shown in Figure 3.8, the normalized heat was plotted versus the overpotential. Since the oxide layer on the surface of the working electrode was not completely removed, there was a bias for the range of negative overpotential, which agreed with the broadened reduction peak of the CV curve in Figure 3.5. Due to the oxide layer on WE surface, the error for calibration was about 2%. When the Ni WE was sufficiently polished, the corresponding normalized heat changed almost linearly and symmetrically with the overpotential, as shown in Figure 3.9. The difference of the Peltier coefficient for calibration, e.g. Figure 3.8 and Figure 3.9, was significant for different experiments due to the variance of the thermal contact between the sensor and the WE. This indicated that the calibration should be conducted in each experiment. The literature value of the Peltier coefficient ($-45.1$ kJ/mol) for the reaction of $K_3[Fe(CN)_6]$ / $K_4[Fe(CN)_6]$ redox pair was compared with the y-intercept (y-axis corresponds to the normalized heat) in Figure 3.9 to obtain the calibration factor.

After the calibration, the lid with the CE and RE was disassembled and the other configuration of the cell was kept unchanged. After the electrolyte was removed, the cell was washed with ultra pure water and acetone for three times, respectively. The setup was then connected to the glove box and evacuated for 10 hours. Before the deposition of aluminium or the deposition of lithium, the cell was washed with the corresponding electrolyte for three times.

### Calibration with nonaqueous solution

When graphite was used as WE, the calibration with aqueous solution is not possible, because the electron transfer reaction in $K_3[Fe(CN)_6]$ / $K_4[Fe(CN)_6]$ aqueous solution can't be conducted on the graphite surface. Fortunately, the Peltier coefficient of lithium deposition (in 1 M $LiPF_6$ electrolyte with lithium as RE and CE) was studied by Schmid[42] and was confirmed in chapter 5 of this work. Therefore, we conducted the calibration using the reaction of lithium deposition. The calibration was conducted after the measurement of charging and discharging of the graphite electrode to avoid damage of the WE. Otherwise, the study of the Peltier coefficient for the charging and discharging would be disturbed by the calibration, which irreversibly changed the structure of the working electrode.

We conducted the calibration by acquiring the Peltier coefficient for lithium deposition. It is also technically practical from the perspective of heat transfer for the calibration by lithium deposition, because the heat conductivity and specific heat capacity of graphite (heat conductivity: $25 \sim 470$ W$m^{-1}K^{-1}$, specific heat capacity: 709 J/(K kg)) are much larger than that of the $LiPF_6$ in EC/DMC. Between the graphite and the lithium tantalate, there are a copper foil (25 µm, 401 W/(m K), 385 J/(K kg)) and sapphire (50 µm, 401 W/(m K), 385 J/(K kg)), as discussed late in section 6.1. According to the specific heat capacity and the heat conductivity of the sapphire sheet and the copper foil, there is no obstacle for the heat transfer from the graphite to the lithium tantalate sensor, when the working electrode (graphite, coated on copper foil), the sapphire and the lithium tantalate were tightly contacted, since the air was removed in the inner sensor compartment with the help of a rotary vane pump (Leybold-Heraeus, Trivac D8B). The pressure reached 0.1 mbar after half an hour.

The calibration was conducted in the glove box including the following procedures. Before the calibration, the graphite was charged to below zero volt where the lithium plating occurred. Then lithium was deposited on the graphite for 3 min under a current of 500 µA (about 2800 monolayers; the area of the active working electrode: 0.2 $cm^2$). After the deposition of lithium, the surface of the working electrode was fully covered with metallic lithium. When the open cell potential was stable around 0 V, potential pulses with different overpotentials were applied to conduct lithium deposition and dissolution. Since the lithium deposition/dissolution was conducted on the surface of lithium, the Peltier coefficient for lithium deposition using graphite as WE is the same as that using Ni as WE.

Using positive overpotential (left) and negative overpotential (right) alternatively, we obtained pulses for calibration with lithium bulk deposition on graphite WE. As shown in Figure 3.10, typical potential pulses including the potential (top, blue), the current (middle, black) and the temperature (bottom, red) transients for lithium deposition in

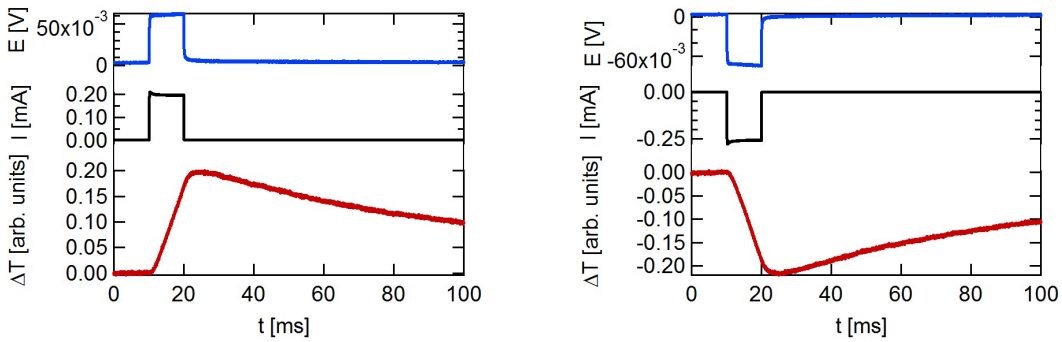


Figure 3.10. – Typical transients of potential (top, blue), current (middle, black) and temperature (bottom,red) for calibration pulses applied with positive overpotential (left) and negative overpotential (right) using graphite as working electrode, Li as reference and counter electrode and 1 M $LiPF_6$ solution (in EC and DMC) as electrolyte.

a Li-graphite half cell with graphite as working electrode, Li as reference and counter electrode and 1 M $LiPF_6$ solution (in EC and DMC) as electrolyte after complete charging and lithium plating are given in this figure.

For Figure 3.10, before applying a pulse, the cell was kept under OCP (open cell potential) condition for 10 ms. Then, potential pulses were applied with an overpotential of ca. 60 mV between $t = 10\ ms$ and $t = 20\ ms$. After the end of the pulse, at $t = 20\ ms$, the system returned to thermal equilibrium within about 1 s. The amount of the converted lithium ions, i.e., the charge, can be calculated by integration of current versus time (i.e. current transient in Figure 3.10). According to the calculation, the charge for the pulses in Figure 3.10 was about 10 µC/cm$^2$ (for the pulse on the left) and $-12.5$ µC/cm$^2$ (for the pulse on the right). Assuming a surface density of $10^{15}\ atoms \cdot cm^{-2}$, this charge correlated to about 6% of a monolayer. From the temperature transient, we confirmed that the temperature responded immediately when the overpotential was applied, which directly reflected the normalized heat of pulses during the electrochemical reaction due to the applied overpotential. The normalized heat was calculated from the temperature difference between $t = 10\ ms$ and $t = 20\ ms$.

The change of the normalized heat for lithium deposition/dissolution on the graphite working electrode with overpotential is shown in Figure 3.11. We applied three sets of pulse measurements, for each of which different overpotentials were used for the potential pulses. Before each of these three measurements, the open cell potential was about 0 V vs. $Li^+/Li$, which also shows that the graphite was fully charged and the surface of graphite was covered with lithium. The change of the normalized heat with the overpotential was approximately linear, i.e. a larger error for smaller overpotentials. The Peltier coefficient was about $1.01 \times 10^5$ in arbitrary unit. It exhibited good reproducibility for the three measurements.

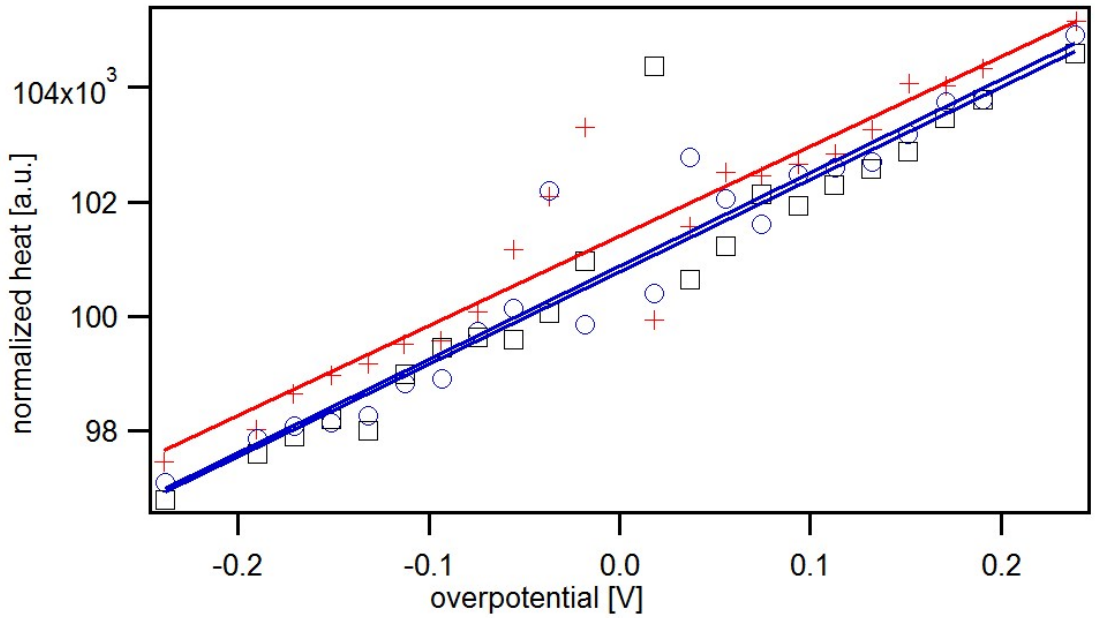


Figure 3.11. – The change of the normalized heat with overpotential before fitting for calibration with the lithium deposition and dissolution reaction, using graphite as working electrode, Li as reference and counter electrode, $LiPF_6$ solution (in EC and DMC) as electrolyte.

### 3.3.2. The fitting of pulses

The aim of fitting is to calculate the delayed heat evolution after the end of the electrochemical pulse. Normally, there is a several millisecond delay after the cell is switched to OCP mode (delayed heat evolution). With the help of fitting, the delayed heat evolution can be calculated using the thermal response function of the cell as measured with laser pulses. In detail, hundreds of 2 ms long laser pulses (405 nm, CS4050205M, Laser Components) are applied after the experiment. The average of these pulses is chosen as the master pulse, i.e. the thermal response function of the cell. Then this master pulse is used to fit the pulses for the calibration. Since the Peltier coefficient of the calibration is known, the heat unit of the master pulse can be calculated. With this master pulse, the heat flow during the measurement can be obtained from the temperature transients[60].

To estimate an optimal number of laser pulses for the fitting, 40 (empty square) and 100 (empty cycle) laser pulses (2 ms long) were used, respectively, for fitting of a typical temperature transient from a measurement during lithium deposition, obtained with positive overpotential, as shown in Figure 3.13 . From the plot of the heat flow versus time in Figure 3.13, we observed that the heat flow continues when the outer cell current was switched off. The first five data points corresponded to the current pulse (2 ms per data point). In Figure 3.13, the temperature transient was fitted from $t = 10\ ms$ to $t = 90\ ms$ (squares) and to $t = 210\ ms$ (circles). The heat flow obtained by 40 laser pulses overlapped well with the results of 100 laser pulses. After about 90 ms, the heat

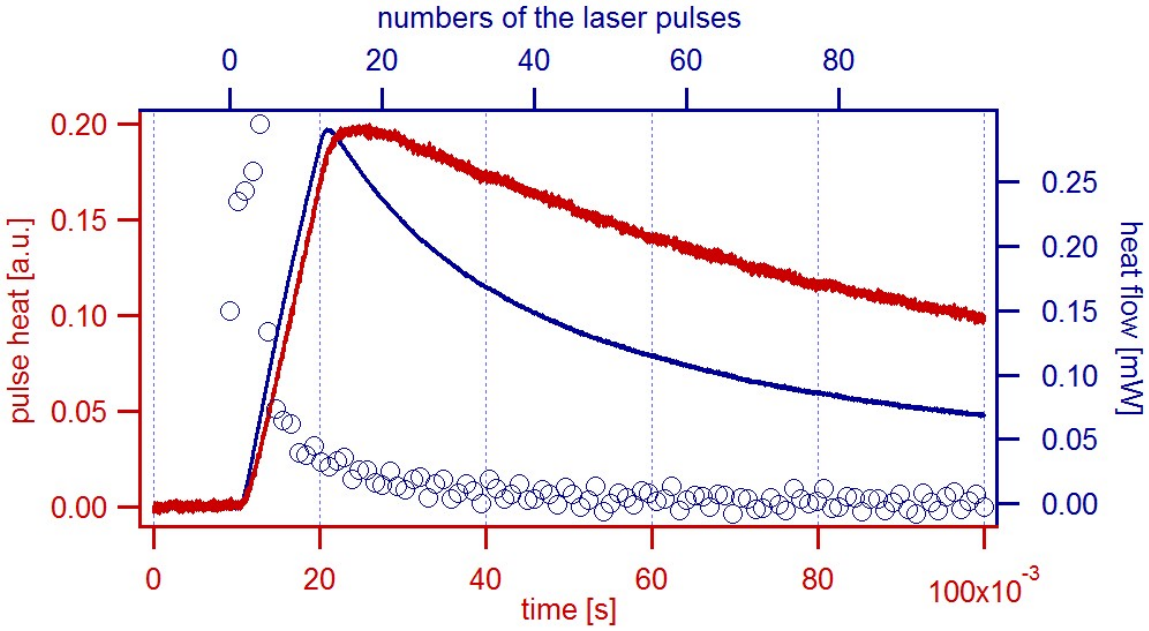


Figure 3.12. – A typical temperature transient (black) for calibration and a 10 ms long laser pulse (red) used for fitting to calculate the delayed heat evolution and the heat flow of the 2 ms long laser pulses (blue empty circles).

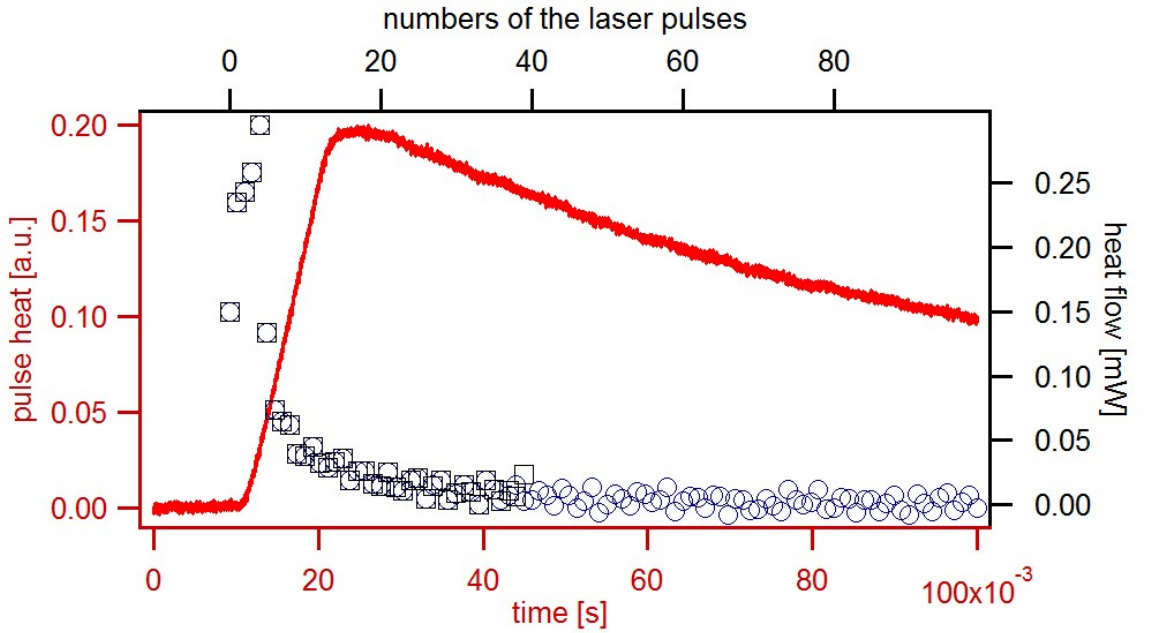


Figure 3.13. – A typical temperature transient (red) for the current pulse during charging, the heat flow of the fitting with 40 laser pulses (black empty square) and 100 laser pulses (blue empty circles).

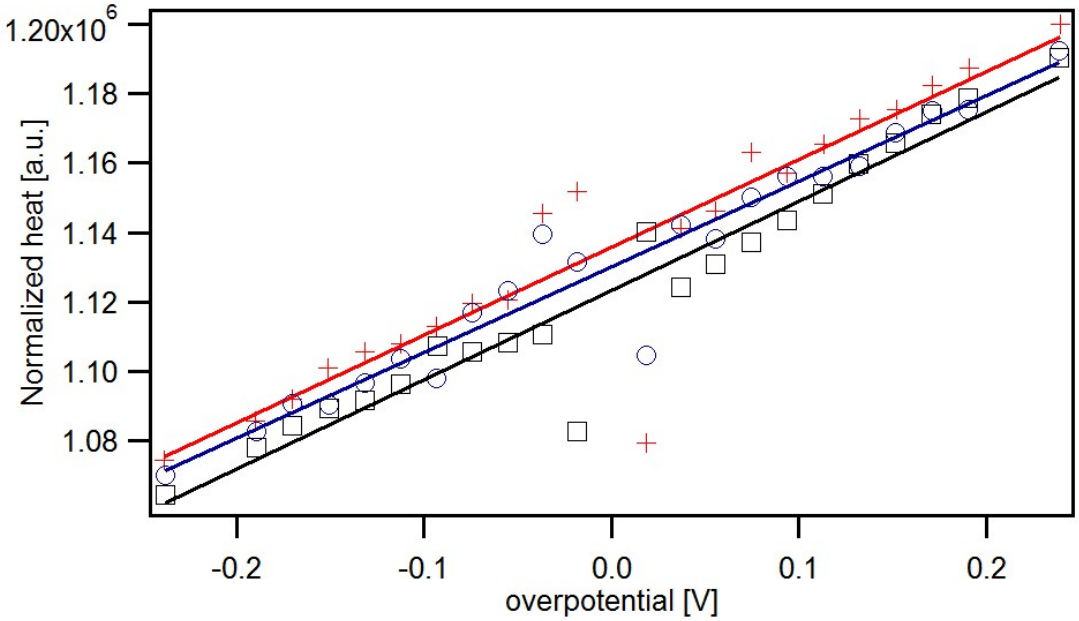


Figure 3.14. – The fitted normalized heat versus overpotential for the lithium deposition and dissolution with graphite as working electrode, Li as reference and counter electrode, $LiPF_6$ solution (in EC and DMC) as electrolyte.

flow became effectively zero, which indicated that the fitting with 40 laser pulses (2 ms long) was sufficient to calculate the total heat.

The normalized total heat, determined from integrating the heat flow up to 90 ms, is shown in Figure 3.14. Only small deviations of the normalized heat were found for the three measurements. The pulses for lithium deposition/dissolution on the graphite working electrode were fitted with 40 laser pulses (2 ms long).

# 4. Concentration effects on reaction entropy during Al deposition

Due to the low-cost, low-flammability, light weight and three-electron redox advantages of aluminium (Al), Al-based rechargeable batteries are promising to possess the advantages of cost-effectiveness, safety and high capacity, which would improve energy storage devices to a large extent[66–68]. While the gravimetric capacity of aluminum is very comparable to that of lithium (2.98 A h/g for Al vs. 3.86 A h/g for Li), the volumetric capacity of Al (8.04 A h/cm$^3$), is larger than that of Li by a factor of three[10]. However, Al is hard to repetitively deposit, which undermines its use as electrode. Furthermore, little is known about the thermodynamics involving the electrode reaction of multivalent species and addressing these challenges would demand the study of both the materials and the thermodynamics for the aluminium battery system[66].

The most recent studies of electrolytes for aluminium-based batteries include both aqueous alkaline and non-aqueous electrolytes. Room temperature ionic liquids (Ils) enable the efficient deposition and stripping of aluminium, which makes rechargeable Al-batteries feasible[69]. $AlCl_3$/BMIMCl as room temperature ionic liquids, which have low melting points, a broad potential window and are non-flammable, have been used as electrolyte for aluminium batteries[68] and the deposition of aluminium[70]. While the structure and composition of the ionic liquids was investigated with infrared spectroscopy[11, 12], Raman spectroscopy[13] and neutron diffraction[14], studies of thermodynamics were rarely reported.

Studies show that the ratio of $AlCl_3$ to BMIMCl influence the composition of the $AlCl_3$/BMIMCl ionic liquids[71, 72]. When the $AlCl_3$ content is higher than 50%, $Al_2Cl_7^-$ and $AlCl_4^-$ ions are present in the electrolytes and the the electrolytes have acidic properties. Only the acidic compositions are feasible for Al plating and stripping[73, 74]. In addition, the conductivity and viscosity of electrolytes are influenced by the concentration of the species[75, 76]. By changing the ratio of the $AlCl_3$ to BMIMCl, the physical and chemical properties (such as the conductivity and viscosity) of the ionic liquids are adjustable, which provides many possibilities for both research and applications[77, 78]. Furthermore, although the chloroaluminate ILs are widely used in the study of aluminium batteries[68, 73, 79], little attention has been paid to the relation between the properties

and the structure of the species[76]. And many controversial aspects still need to be addressed, such as the the ionic moieties present at the different compositions[76].

In this chapter, we performed microcalorimetry for an investigation of the electrochemical reaction of aluminium deposition/dissolution in the aluminium half cell with BMIMCl/$AlCl_3$ of different ratio as electrolyte and aluminium wire as reference and counter electrode. Ni and W can be used as WE, because they do not react with aluminium and the calibration could be conducted on these working electrodes. The Peltier coefficient and reaction entropy of aluminium plating/stripping was determined for different electrolytes with various composition, which can shed light on the ionic moieties and their interactions in the BMIMCl/$AlCl_3$ electrolytes.

## 4.1. Experiment

### 4.1.1. The preparation of the chemicals

The $K_3[Fe(CN)_6]$ and $K_4[Fe(CN)_6]$ (GR for analysis) were purchased from Merck KGaA. The BMIMCl (over 95%) and $AlCl_3$ (over 99%) were obtained from Fluka Chemistry. 0.1 M $K_3[Fe(CN)_6]$/ $K_4[Fe(CN)_6]$ aqueous solution was prepared and then stored in volumetric flask. Six electrolytes of ionic liquid with different molar fraction of $AlCl_3$ were prepared by adding the $AlCl_3$ powder very slowly to the beaker which contained the BMIMCl and stirring for 30 min with a magnetic stirrer at the same time to avoid decomposition. Each of the ionic liquid electrolytes was prepared before the measurements. The chemicals involved in this experiment were stored in a glove box ($O_2 < 4\ ppm$; $H_2O < 0.5\ ppm$).

### 4.1.2. The calibration

The calibration was conducted in ambient environment using the one electron transfer reaction of the $K_3[Fe(CN)_6]$ / $K_4[Fe(CN)_6]$ redox pair, as described in section 3.3.1. Since the aluminium deposition will irreversibly change the surface of the working electrode, the calibration should be conducted before the aluminium deposition.

### 4.1.3. Electrochemical and microcalorimetric measurement of aluminium deposition

All of the experiments in this part were conducted inside the glove box in which the concentration of $O_2$ was below 4 ppm and the concentration of $H_2O$ below 0.5 ppm. The working electrode (WE), which acted as cathode during the reaction of aluminium deposition, was the same as the calibration reaction. Aluminium was used as reference

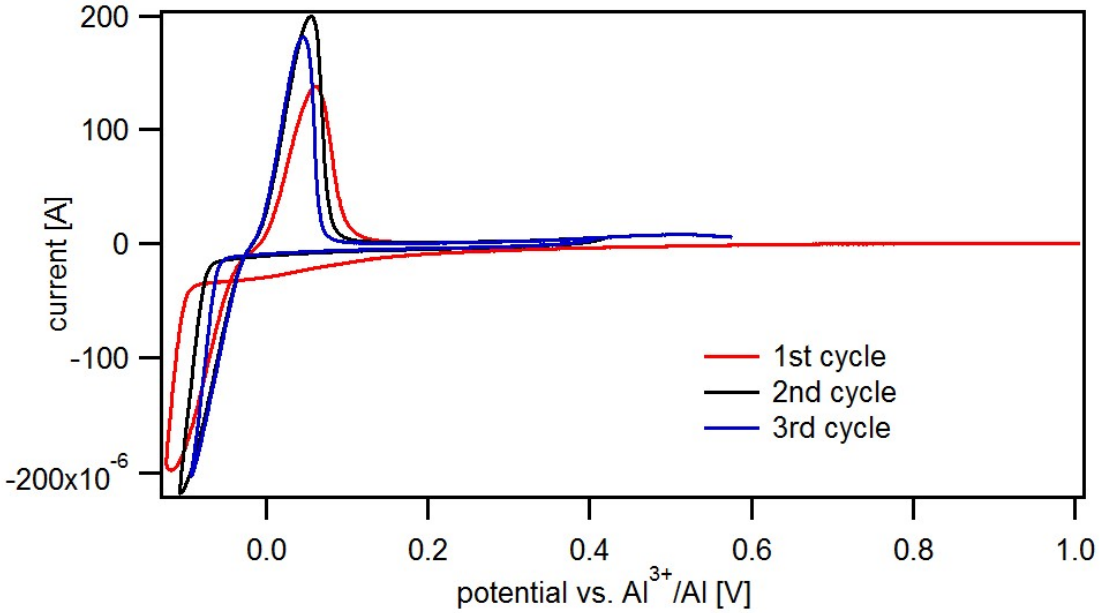


Figure 4.1. – The cyclic voltammogram for aluminium deposition using $AlCl_3$ : BMIMCl ionic liquids (1.7: 1) as electrolyte, Ni as WE, aluminium as RE and CE. The CV was recorded, starting from 1 V, which was repetitively scanned between -0.1 V and 0.6 V. The scan speed was 50 mV/s.

(RE) and counter electrode (CE). They were processed with sand paper, washed with ultra pure water in an ultrasonic cleaner, dried with paper and transferred to the glove box immediately.

During the cyclic voltammogram, the potential was scanned between $-0.2$ V and 0.4 V with a scan speed of 50 mV/s. Before the deposition of aluminium, 1 V was applied for 60 s [65] to remove the oxide layer from the surface of the working electrode. The pretreatment process by applying positive potential is similar to acidic etching (as in concentrated $H_2SO_4$), which can activate the oxide layer of the WE[80, 81]. In order to make the reaction of aluminium deposition/dissolution reversible, hundreds of layers of aluminium should be deposited beforehand (with a current of 500 µA for 3 min, area of the WE: 0.2 $cm^2$). The system was then kept at open cell potential (OCP) for 10 min until the equilibrium was reached. In the next step, potential pulses with different amplitudes were applied to measure the Peltier coefficient of the reaction for aluminium deposition/dissolution.

## 4.2. Results

Figure 4.1 shows the CV curve of the aluminium deposition/dissolution process on a Ni WE when the ratio of $AlCl_3$ to BMIMCl was 1.7:1. From 0.8 V to 0.2 V, there was a

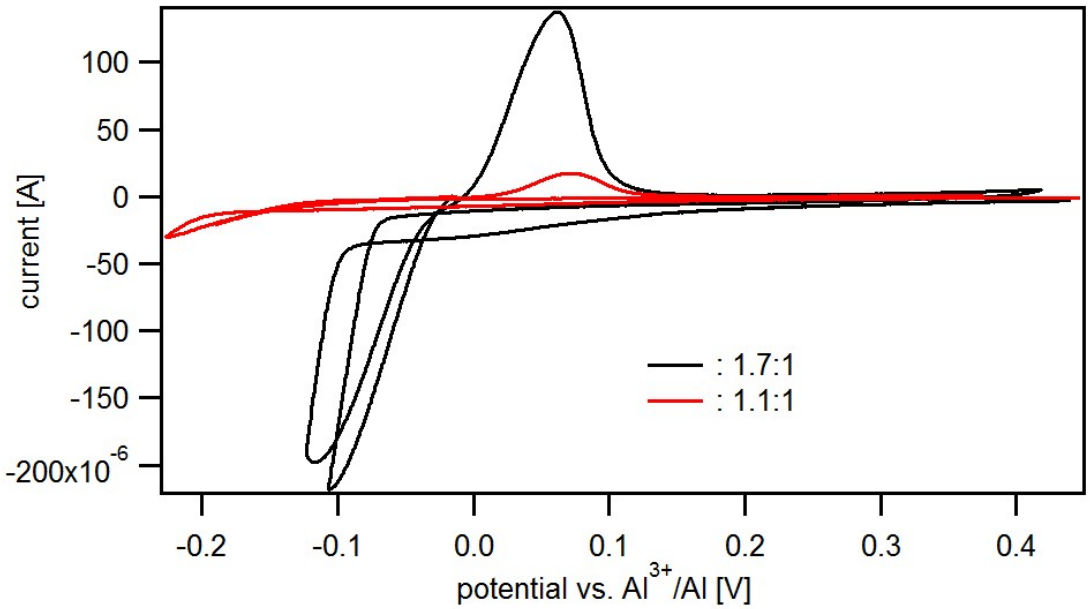


Figure 4.2. – The cyclic voltammogram for aluminium deposition using $AlCl_3$ : BMIMCl ionic liquids (1.7: 1, black one) and (1.1: 1, red one) on the working electrode and the aluminium counter electrode.

small current and no peaks could be observed in this potential region. Considering the scan speed and the charge, the capacity of the double layer was about $2.4 \cdot 10^{-4}$ F/cm$^2$.

The current increased significantly at about $-0.1$ V, corresponding to the deposition of the aluminium. As shown in Figure 4.1, the slope of the curve around 0 V was very steep, which indicated a successful deposition of aluminium. And the slope of the first cycle at around 0 V was significantly steeper than that of the second and the third. From the third cycle, the variance of the slope around 0 V was small, which indicates that the reaction of aluminium deposition/dissolution was reversible. Another example could be found in Figure 4.2, in which the slope of the CV curve around 0 V was steeper when the ratio of $AlCl_3$ to BMIMCl was 1.7:1 (compared with the sample, where the ratio was 1.1). The capacity of the double layer was about $5.9 \cdot 10^{-5}$ F/cm$^2$. Furthermore, a larger current could be found when the ratio of $AlCl_3$ to BMIMCl was 1.7:1. The slope of the CV curve around 0 V indicates the extent of the difficulty of the aluminium deposition.

Figure 4.3 and Figure 4.4 show optical microscopy images of the surface of a tungsten working electrode before and after the deposition of aluminium, respectively. In Figure 4.3, the scratches from the sandpaper could be seen clearly. After the deposition of aluminium for 3 min with a current of 500 µA (inside the glove box, area of the WE: 0.2 cm$^2$), the surface of the working electrode was partly covered with several layers of deposit. If we chose $1 \cdot 10^{15}$ $atoms \cdot cm^{-2}$ as the number of metal atoms on a close packed surface, about 940 layers of alumnium were deposited on average.

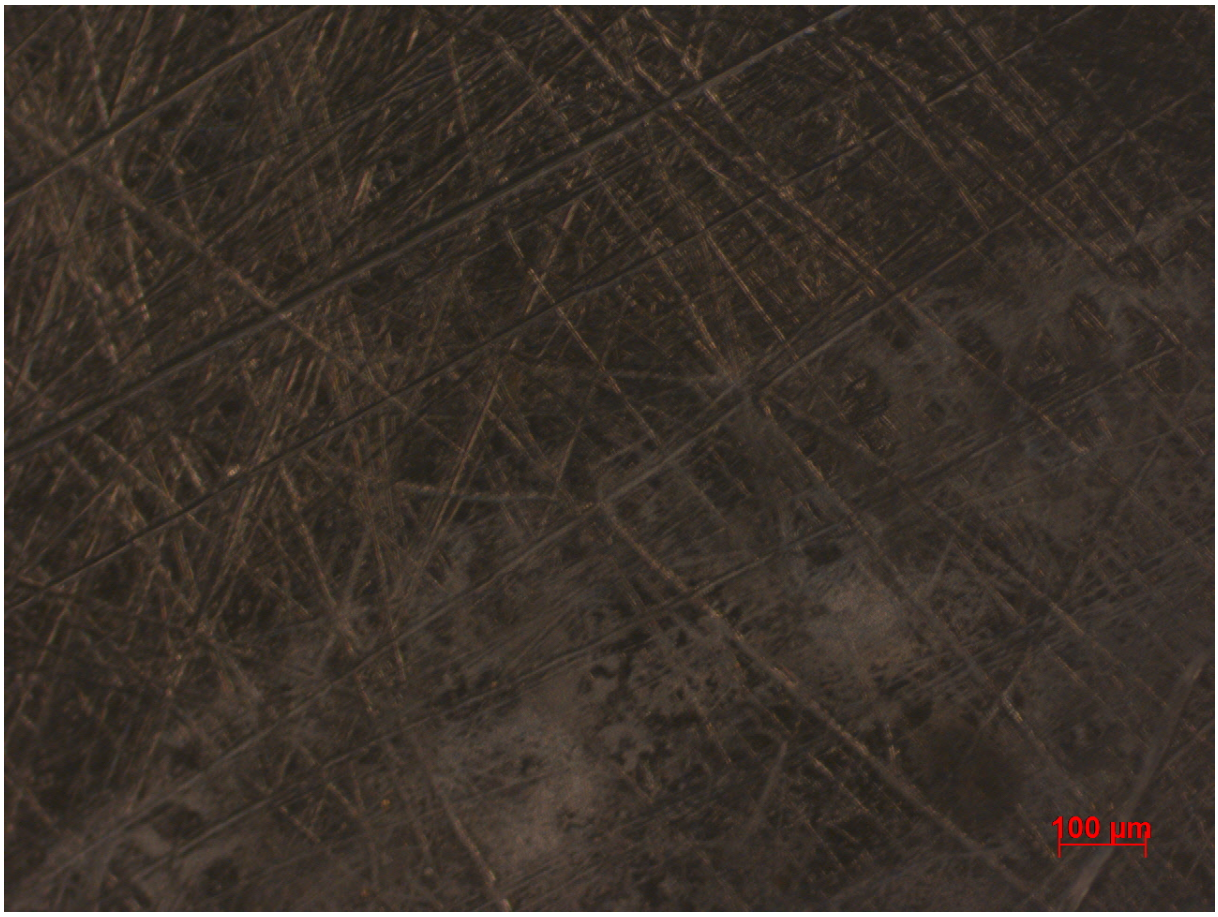


Figure 4.3. – Optical image of the surface for the polished tungsten foil as working electrode before the deposition of aluminium.

Aluminium oxide was formed when the WE was exposed to air, while the WE was transferred to the microscope. From the optical microscopy image of the surface of the working electrode and the CV curve of the reaction, we can confirm that aluminium was deposited on the working electrode in this system of ionic liquid.

Figure 4.5 shows the potential, current and temperature transients of a typical pulse, obtained with an overpotential of ±80 mV versus the $Al/Al^{3+}$ equilibrium potential. The left part shows the transients for aluminum dissolution. When the potential pulse started at $t = 10\ ms$, the temperature of the sensor responded immediately. At the end of the pulse ($t = 20$ ms), the temperature of the sensor reached the minimum of -0.16 in arbitrary units. Then the cell was kept at the open cell potential (OCP) condition and the temperature relaxed to equilibrium. The charge of the pulse could be obtained by integration of the current transient (±27.5 µC/cm$^2$ for the transients shown in Figure 4.5). Less than 10% of a monolayer of aluminium was dissolved/deposited under the assumption that it's single crystal aluminum with face centered cubic structure on the tungsten working electrode. The normalized heat of the pulses in aluminum deposition/dissolution experiments was obtained by dividing the amplitude of the pulse heat by pulse charge.

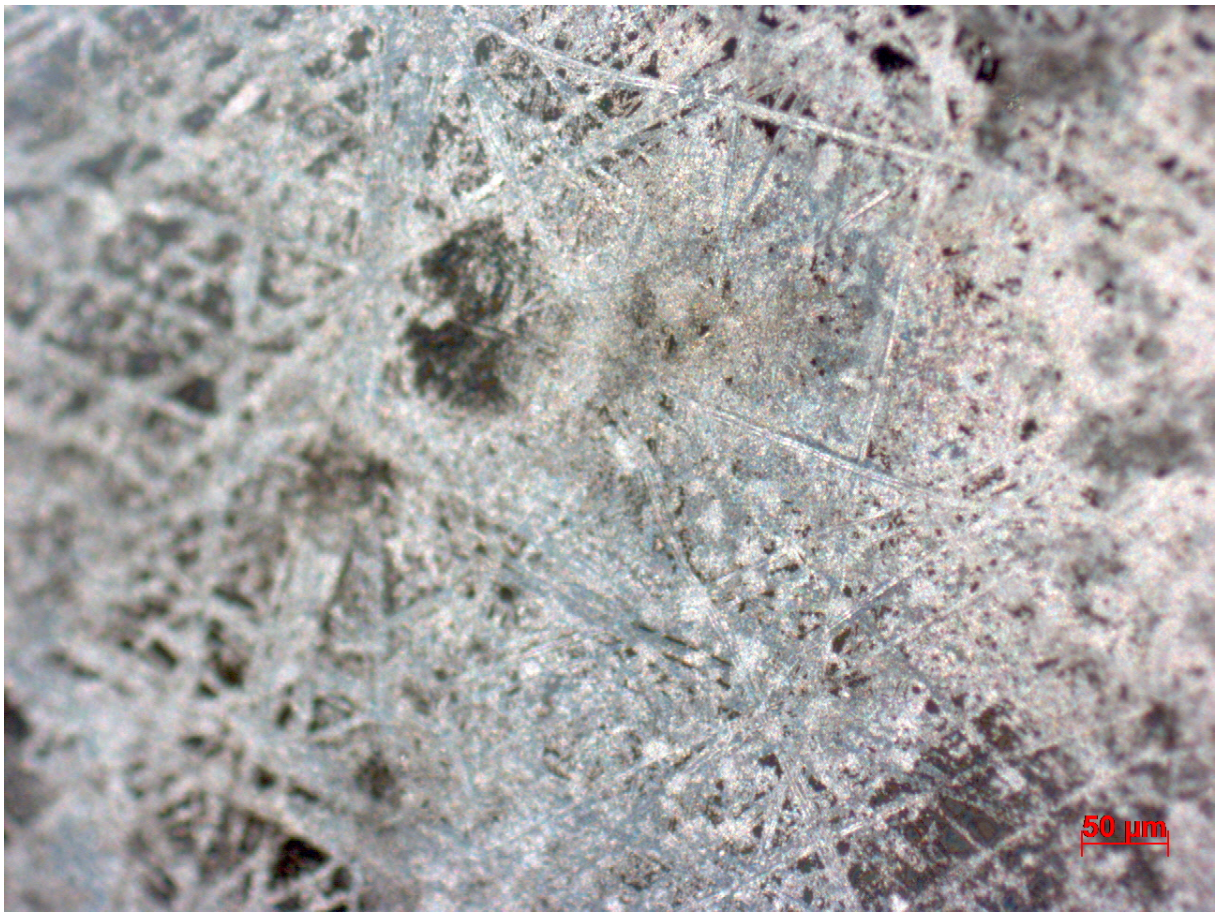


Figure 4.4. – Optical image of the surface for the polished tungsten foil as working electrode after the deposition of aluminium.

The change of normalized heat with overpotential is shown in Figure 4.6. For negative overpotential pulses, corresponding to aluminum deposition, we found a decrease of temperature. Therefore, there was a cooling effect where negative overpotental pulses were applied. The positive pulses show an increase in temperature, and corresponded to the dissolution of aluminium. According to Equation (2.19) in chapter 2, the heat change was composed of three factors. The first one was the reversible heat from the electrochemical reaction. The second factor is irreversible heat which is due to a polarization of the charge on the electrode because of the overpotential. The third, Joule heat, was also irreversible because of the current flow through the electrolyte. But the contribution of Joule heat could be neglected in our system since the applied overpotential was very small and lasted only 10 ms.

In our measurement, when the ratio of $AlCl_3$ to BMIMCl was 1.7, the Peltier coefficient $\Pi$ ($\Pi = T\Delta S$) for the aluminum deposition/dissolution reaction was about 10 kJ/mol and had a good reproducibility. The transport heat was calculated according to Equation (2.16) in subsection 2.1.2, which was only about 7.6 J/mol and could be neglected compared with the Peltier coefficient.

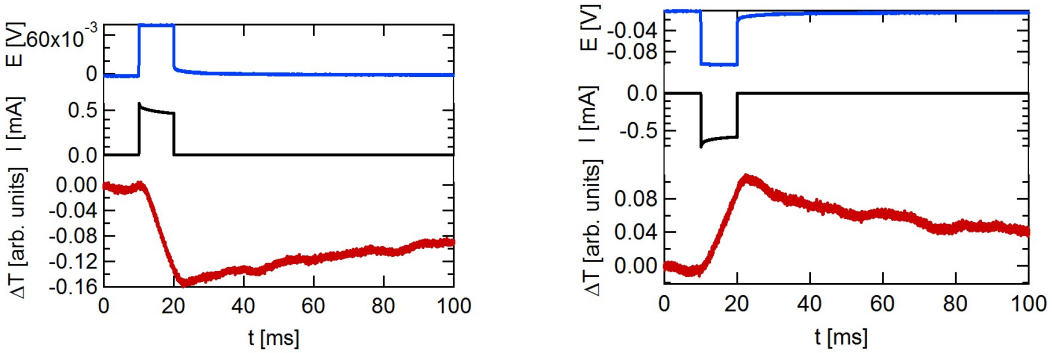


Figure 4.5. – Typical pulses including potential (top), current (middle), and temperature (bottom) transients of aluminum dissolution (left) and deposition (right). Aluminum deposition/dissolution was conducted on a ca. 940 monolayer-thick aluminum-film on Ni by applying a pulse with a overpotential of 20 mV at $t = 10\ ms$. At $t = 20\ ms$ the outer circuit was switched to open and the temperature reached equilibrium close to 1 s.

## 4.3. Discussion

### 4.3.1. Aluminium deposition on W or Ni

In these experiments, we chose tungsten or nickel as working electrode. Firstly, about 940 monolayers of aluminium was deposited on the working electrode before the measurements

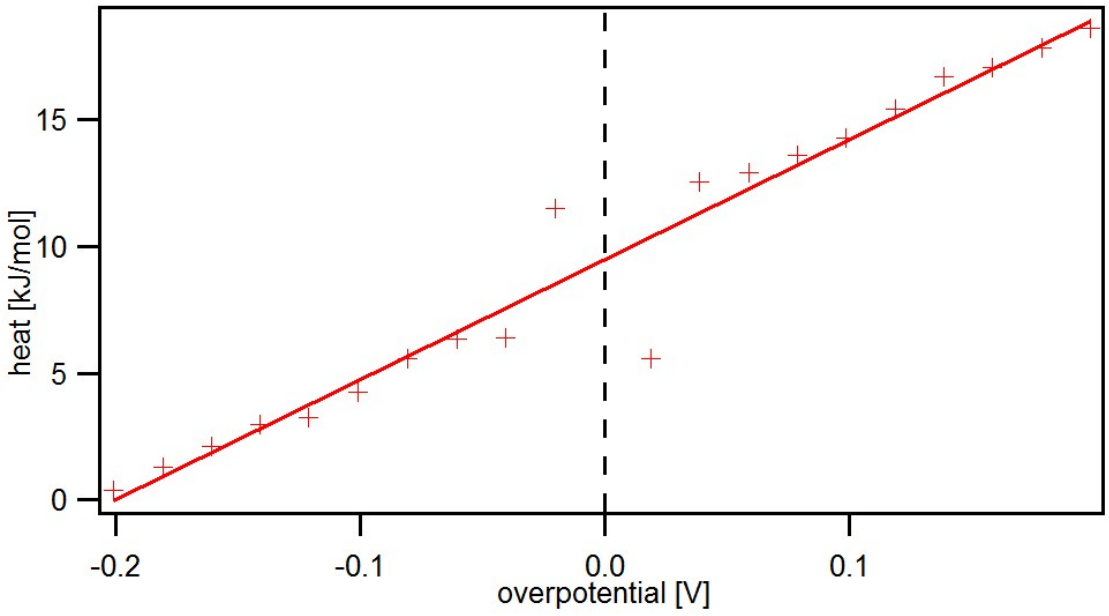


Figure 4.6. – The normalized heat of pulses duing aluminium deposition after fitting with 2-ms-laser pulses (40). To separate the reversible heat effect from irreversible effects that are due to overpotential, we extrapolated the overpotential to zero.

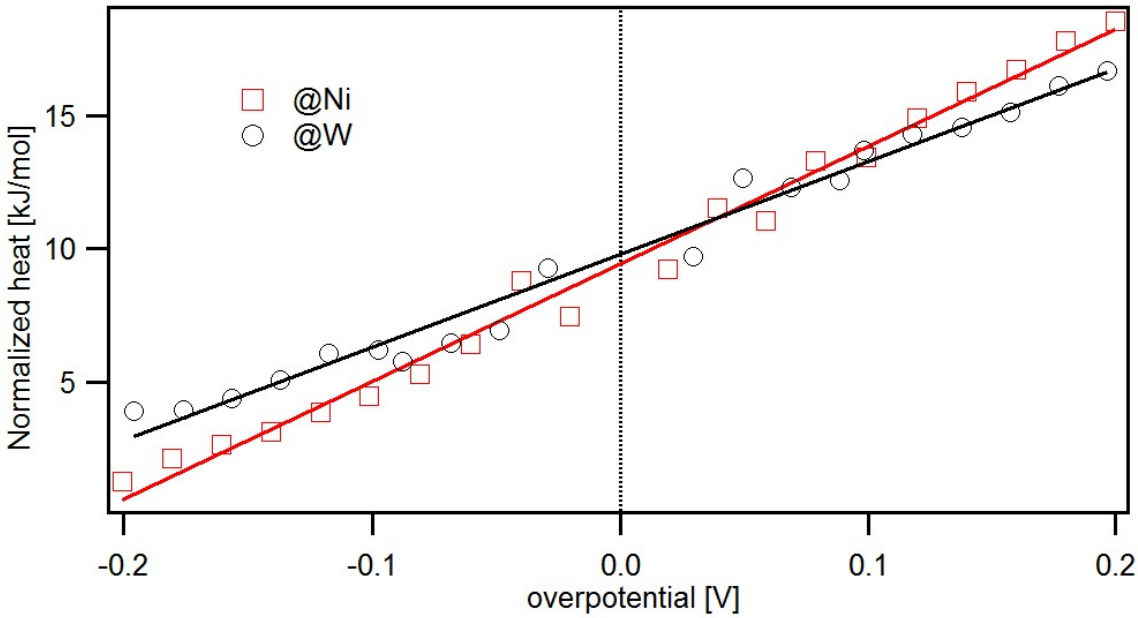


Figure 4.7. – The normalized heat (with calibration and fit) of pulses during the aluminium deposition using Ni (red) and W (black) as working electrode, respectively. The electrolyte used here was $AlCl_3$ : BMIMCl ionic liquids (1.7: 1).

of the reversible heat. As can be seen from Figure 4.4, the reaction we measured here occurred on the surface of aluminium. As shown in Figure 4.7, the Peltier coefficient of the aluminium deposition/dissolution on W and Ni were both 10 kJ/mol with a variance of 0.2 kJ/mol when the ratio of $AlCl_3$ to BMIMCl was 1.7). Therefore, the materials of the WE has no influence on the reversible heat of the reaction.

There are two requirements for choosing the working electrode. One of the prerequisites for choosing a certain metal foil as working electrode is that it doesn't react with alumnium, which indicated the second requirement for choosing a WE: the calibration reaction can be conducted on the working electrode. Since the aluminium WE facilitates the deposition of alumnium because of its similar lattice structure with the aluminium deposit, Al can be a good choice as WE. However, the $K_3[Fe(CN)_6]/K_4[Fe(CN)_6]$ redox pair reaction for calibration can't be conducted on Al WE.

### 4.3.2. Warming or cooling effect when ratio of aluminium chloride to BMIMCl is 1.7

As shown in Figure 4.8, the transient of the heat signal for aluminium dissolution was compared with that of a laser pulse. The change of the temperature was in the same direction. Since it's always warming effect for laser pulses, the aluminium dissolution has a warming effect and vice versa, the aluminium deposition has a cooling effect. Even

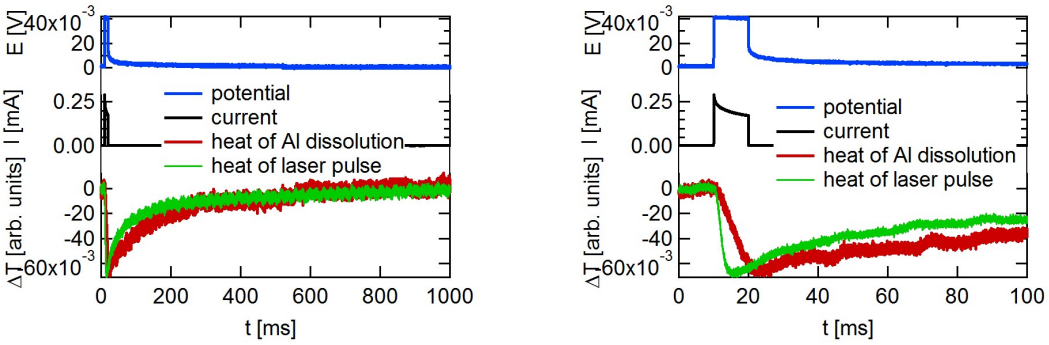


Figure 4.8. – The full (left) and enlarged potential pulse including the transients (right) of potential (top, blue), current (middle, black), and temperature (bottom, red) for aluminum dissolution and a 2-ms-laser pulse. Aluminum dissolution was conducted on a ca. 940 monolayer-thick aluminum-film on Ni by applying a pulse with a overpotential of 20 mV at $t = 10\ ms$. At $t = 20\ ms$ the outer circuit was switched to OCP mode and the temperature reached equilibrium close to 1 s. Since the laser pulse causes a warming effect, the comparison between the laser pulse and the temperature transient could give us a clue for the heat effect of the aluminium deposition.

Table 4.1. – The Peltier coefficient and entropy for aluminium deposition/dissolution with different ratio of $AlCl_3$ to BMMIMCl

| Ratio ($AlCl_3$:BMIMCl) | Peltier coefficient (kJ/mol) | Entropy (J/mol/K) |
|---|---|---|
| 1.7:1 | 9.6 | 32.2 |
| 1.5:1 | 3.5 | 11.7 |
| 1.4:1 | 1.8 | 6.0 |
| 1.3:1 | -1.3 | -4.5 |
| 1.2:1 | -3.6 | -11.3 |
| 1.1:1 | -9.4 | -31.4 |

though the change of temperature for one single pulse was tiny due to the small amount of charge, it could have a significant influence during the charging of Al batteries when a transfer of more charge is involved. Therefore, the thermal effects of the reaction should be considered in the design of energy storage devices.

### 4.3.3. Different ratio of aluminium chloride to BMIMCl

The Peltier coefficient of aluminium deposition in six electrolytes with different ratio of $AlCl_3$ to BMIMCl was measured with good reproducibility and the corresponding reaction entropy was calculated, as shown in Table 4.1 and Figure 4.9. When the ratio of $AlCl_3$ to BMIMCl was 1.7:1, the Peltier coefficient was $(9.6 \pm 0.5)$ kJ/mol. Thus the reaction entropy of one mole electron was about $(34 \pm 3)$ J/(mol K). As the ratio of $AlCl_3$ decreased, the Peltier coefficient also decreased. When the ratio was 1.3, the Peltier coefficient

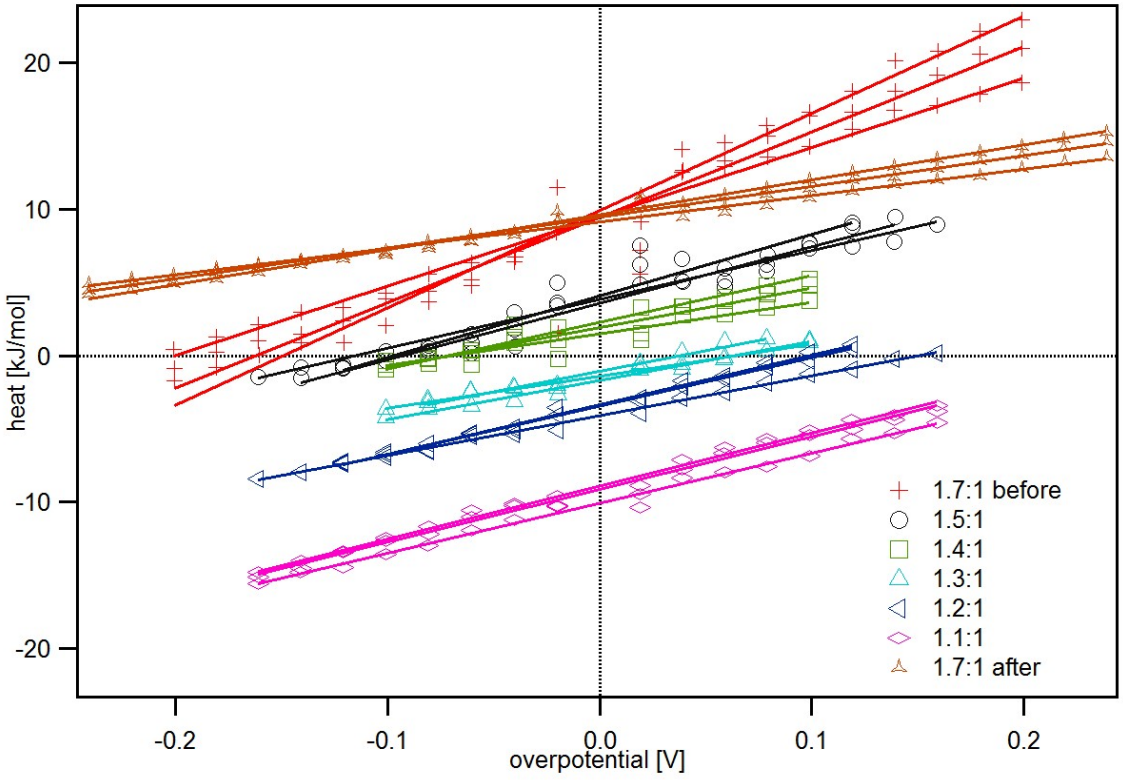


Figure 4.9. – The normalized heat of the dissolution and deposition of aluminium versus the overpotential for a series of measurements conducted in ionic liquid electrolytes with different molar ratios of $AlCl_3$ to BMIMCl (1.7, 1.5, 1.4, 1.3, 1.2, 1.1) and on a Ni working electrode. It shows a good reproducibility and regular decrease with the decrease of ratio of the $AlCl_3$ to BMIMCl.

became negative ($-0.7$ kJ/mol). As the ratio decreased to 1.1:1 ($AlCl_3$ to BMIMCl) , the corresponding Peltier coefficient was $(-9.4 \pm 0.5)$ kJ/mol. Compared with the Peltier coefficient for the deposition of copper (54.8 kJ/mol) and silver ($-5.8$ kJ/mol)[82], the cooling effect of the aluminium deposition using the electrolyte with a ratio of 1.7:1 ($AlCl_3$ to BMIMCl) is comparable to the deposition of $Cu^{2+}$.

As mentioned, when the ratio of $AlCl_3$ to BMIMCl was smaller than 1.3:1, it's difficult to deposit aluminium directly on W or Ni WE. Thus, we firstly deposited 940 layers of aluminium on working electrode. Then, the cell was washed using the electrolyte with smaller ratio ($AlCl_3$ to BMIMCl), following by adding the corresponding electrolyte. Typical pulses including potential (top), current (middle), and temperature (bottom) transients of aluminum dissolution/deposition using the electrolyte of 1.1:1 are shown in Figure 4.10. It is demonstrated that the aluminium deposition using the elctrolyte of 1.1:1 ($AlCl_3$ to BMIMCl) was reversible.

When the molar fraction of $AlCl_3$ is between 58% and 65% (the ratio of $AlCl_3$ to BMIMCl is between 1.4:1 and 1.7:1), the predominant ion in the ionic liquid electrolytes was $Al_2Cl_7^-$

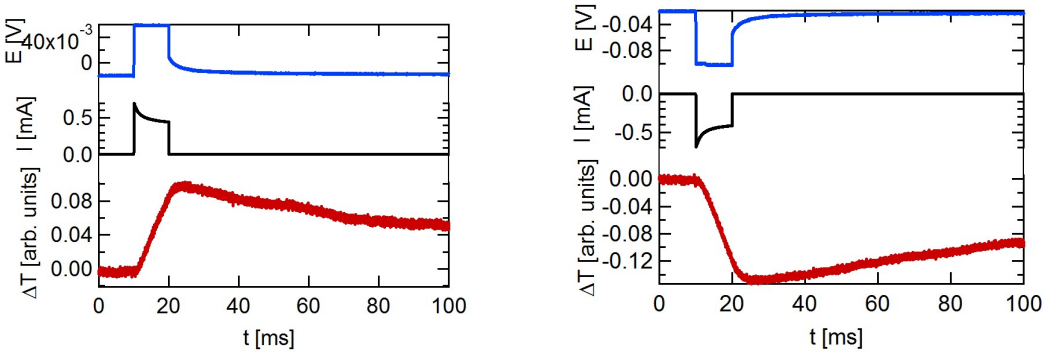


Figure 4.10. – Typical pulse including potential (top), current (middle), and temperature (bottom) transients of aluminum dissolution/deposition using the electrolyte of 1.1:1. Aluminum deposition/dissolution was conducted on a ca. 940 monolayers aluminum-film on Ni WE by applying a pulse with a overpotential of 40 mV at $t = 10\ ms$. At $t = 20\ ms$ the outer circuit was switched to open and the temperature reached equilibrium close to 1 s.

[71, 72]. The main reaction of aluminium deposition on the working electrode could be determined as the following[68, 83]:

$$4[Al_2Cl_7]^- + 3e^- \longrightarrow Al + 7[AlCl_4]^- \tag{4.1}$$

Lai *et al.* showed that the deposition of aluminium was not a single step reaction and a more complex mechanism with several steps was involved[84]. Under the control of potential, one $Al_2Cl_7^-$ ion was adsorbed to the aluminium surface in the applied electric field. Electrons on the working electrode were provided to the adsorbed $Al_2Cl_7^-$ ion, after which one of the aluminium atoms in $Al_2Cl_7^-$ ion was immobilized and produced three chloride ions. The three chloride ions, detached from the immobilized aluminum atom, reacted with three $Al_2Cl_7^-$ molecules and formed six $AlCl_4^-$ ions. This process could also be denoted as the following equations[84, 85]:

$$[Al_2Cl_7]^- \rightleftharpoons [AlCl_3...AlCl_4] \tag{4.2}$$

followed by[84, 85]:

$$\begin{aligned} [AlCl_3...AlCl_4]^- + 3e^- &\longrightarrow Al + [AlCl_4]^- + 3Cl^- \\ 3Cl^- + 3[Al_2Cl_7]^- &\rightleftharpoons 6[AlCl_4]^- \end{aligned} \tag{4.3}$$

The equilibrium constant for reaction (4.2) was reported to be about 3.25 at 40 °C by a chronopotentiometric measurement and a calculation according to Sand's equation[85, 86]. These reactions of (4.2) and (4.3) yielded a overall reaction of (4.1).

According to Equation (4.1), the entropy relation could be denoted as following:

$$7S_{AlCl_4^-} - 4\,S_{Al_2Cl_7^-} = 3\,\Delta_r S - S_{Al} \tag{4.4}$$

where $\Delta_r S$ was the reaction entropy for one mole electrons. $3\Delta_r S$ should be used in the equation, because three mole electrons were transferred when one mole aluminium was deposited.

Even though the immobilization of Al ions on the WE leads to the decrease of entropy, the change of the solvation shell and the entropy increase due to the produced species should be considered. Since four larger $Al_2Cl_7^-$ molecules were sacrificed and seven smaller $AlCl_4^-$ molecules were produced, it's reasonable that a positive reaction entropy was obtained when the ratio of $AlCl_3$ to BMIMCl was 1.7:1.

The reaction entropy of aluminium deposition decreased when the ratio of $AlCl_3$ to BMIMCl decreased, as shown in Table 4.1, which is probably due to the change of the concentration of the ions in ionic liquids (the dilution entropy of the predominant ions). The effect of concentration change of ions on the reaction entropy of aluminium deposition can be calculated by combining Equation (4.4) and the equation of $S_{X^-} = S^o_{X^-} - Rln(a_{X^-} - RT((da_{X^-})/(dT))$[50]. Here $X^-$ is the predominant ions in ionic liquids, i.e. $AlCl_4^-$ and $Al_2Cl_7^-$. $S^o_{X^-}$ is the standard molar entropy of $X^-$. $a_{X^-}$ is the activity of $X^-$. The temperature dependence of the activity, which is usually small, can be neglected. There is a deviation between the calculated results of concentration effects and the experimental results for the change of reaction entropy with the ratio of $AlCl_3$ to BMIMCl. A possible reason is that other processes, such as the adsorption of ions on working electrode which has a negative entropy, are involved during aluminium deposition.

## 4.4. Conclusion

In this chapter, with the help of electrochemical microcalorimetry, we obtained the Peltier coefficient (molar exchanged heat) and the reaction entropy for aluminum deposition/dissolution process using $AlCl_3$/BMIMCl ionic liquids with different ratios of $AlCl_3$ to BMIMCl as electrolyte. Tungsten or nickel was suitable as working electrode, while aluminium was not feasible in this reaction, since the calibration reaction couldn't be conducted on an Al WE. Al wires could be used as reference electrode and counter electrode, since the Al reference electrode provided a stable reference potential.

The Peltier coefficient was $(9.6 \pm 0.5)$ kJ/mol when the ratio of $AlCl_3$ to BMIMCl was 1.7:1. A cooling effect was found for aluminium deposition, while a warming effect for aluminium dissolution. When the ratio of $AlCl_3$ to BMIMCl decreased, the corresponding Peltier coefficient and reaction entropy also decreased. As the ratio of $AlCl_3$ to BMIMCl

was between 1.4:1 and 1.7:1, the predominant ions in the ionic liquid electrolyte was $Al_2Cl_7^-$. During the deposition of aluminium, seven $AlCl_4^-$ ions were produced with a sacrifice of four $Al_2Cl_7^-$ ions when one aluminium ion was immobilized, which leaded to the positive sign of the reaction entropy. The Peltier coefficient became negative when the ratio of $AlCl_3$ to BMIMCl was between 1.4:1 and 1.1:1.

The concentration effects on the change of reaction entropy was partly due the dilution entropy of the predominant ions. Some other processes, such as the adsorption of ions, were also expected.

# 5. Concentration effects on reaction entropy during lithium deposition

Lithium-ion batteries are widely used for energy storage in many fields, e.g., in portable electronic devices[66]. Ongoing research efforts aim to extend their use in new fields such as electric automobiles. Li-ion batteries operate with an electrolyte consisting of a lithium salt in organic solvents. Usually a mixture of cyclic and acyclic carbonates is used as solvent in order to combine advantageous properties such as a high dielectric constant, low viscosity, low melting point, high boiling point and high conductivity[87, 88]. Particularly the viscosity and conductivity of the electrolyte are influenced by the concentration of the lithium salt. At high concentrations, lithium and its counter ion may form neutral ion contact pairs, which do not contribute to the conductivity[89]. Additionally the coordination number of the lithium ion may change with both concentration and electrolyte composition[88–92]. Information on the behavior of solvated lithium and the molecular structure of lithium-solvent aggregates is helpful to study cointercalation[93] and the formation of layers covering the electrode (also called solid electrolyte interphase layer, SEI layer)[94] and to design electrolytes[95].

The solvation of lithium ions in battery electrolytes has therefore been studied by several methods, including Raman- and IR- spectroscopy, DFT- and MD- calculations[91, 93], ionization mass spectroscopy[96], NMR[90, 92, 94], and conductivity measurements[95].

In this study, we investigated concentration effects on reaction entropy during electrochemical deposition of lithium from a solution of $LiPF_6$ in a mixture of ethylene carbonate (EC) and dimethylcarbonate (DMC) using electrochemical microcalorimetry (see References [23, 60, 97]). A series of $LiPF_6$ electrolytes in different concentrations (1 M, 0.1 M, 0.01 M) were used in order to gain information on the solvation behavior of $Li^+$ upon dilution, possible changes in coordination and the influence of contact ion pair formation. These results were partly published in the reference[75]. The discussion in this work closely follows that reference[75].

# 5.1. Experiment and chemicals

## 5.1.1. Chemicals

The $K_3[Fe(CN)_6]$ and $K_4[Fe(CN)_6]$ (GR for analysis) were purchased from Merck KGaA. 1 M Lithium hexafluorophosphate ($LiPF_6$) in ethylene carbonate (EC) and dimethyl carbonate (DMC) ($EC : DMC = 1 : 1$) was from BASF (battery grade) and stored in the glove box. A mixture (1:1, wt%) of EC (Alfa Aesar, 99%) and DMC (Alfa Aesar, 99%) was prepared as solvent in the glove box ($O_2 < 4\ ppm$; $H_2O < 0.5\ ppm$). The solvent was stored in a ground-glass stoppered flask with proper amount of molecular sieve for purification. The $LiPF_6$ electrolytes with lower concentration (0.1 M, 0.01 M) were prepared by adding a mixture (1:1, wt%) of EC and DMC to the $LiPF_6$ solution (1M). The diluted electrolytes (0.1 M and 0.01 M) were freshly prepared before each measurement. Ni foil and Au foil, as working electrode (WE), were cut in round pieces with a diameter of 9 mm. Ni was polished with diamond paste (0.7 µm-HK-A, from Walter Messner GmbH), followed by washing with ultra pure water. For the calibration, platinum wire with a diameter of 0.2 mm was used as reference electrode (RE) and counter electrode (CE). For the deposition of lithium, lithium wire (2 mm) was used as RE and CE.

## 5.1.2. Electrochemical and microcalorimetric measurement of lithium deposition

The electrochemical and microcalorimetric measurements of lithium deposition were performed in the glove box, where the concentration of $O_2$ was below 4 ppm and the concentration of $H_2O$ below 0.5 ppm. Ni and Au were used as working electrodes, respectively. For lithium deposition, the platinum could also be used as pseudo RE and CE[42]. However, the lithium is more suitable as RE, due to the better-defined reference potential for the deposition of lithium. On lithium CE, the deposition/dissolution of lithium becomes reversible. In addition, there is no difference of the Peltier coefficient between the platinum and lithium as RE and CE[42, 75]. Therefore, lithium was used (as RE and CE) in this chapter. Before the measurement of each electrolyte, the cell was rinsed with the corresponding electrolyte for three times. The measurements in the glove box consisted of two parts. Firstly, a cyclic voltammogram (CV) was recorded, starting at 3.4 V (open cell potential), which was repetitively scanned between −0.2 V and 1 V. When the CV demonstrated a good reproducibility, the reversible heat of the reaction was measured with the microcalorimeter by applying potential pulses with different amplitudes.

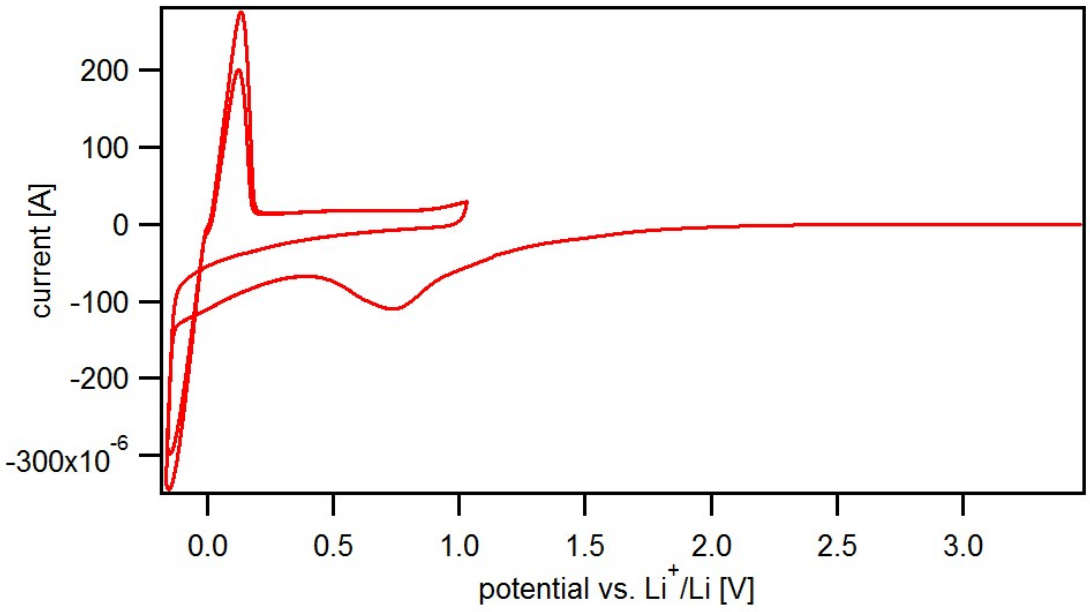


Figure 5.1. – The cyclic voltammogram with 1 M $LiPF_6$ in ethylene carbonate (EC) and dimethyl carbonate (DMC) as electrolyte, Ni as working electrode and lithium as RE and CE electrodes. The CV was recorded, starting from 3.4 V, which was repetitively scanned between -0.1 V and 1 V.

## 5.2. Results

### 5.2.1. Results of lithium deposition on a Ni working electrode

Considering the requirement of calibration and the deposition of lithium, we used polished Ni as working electrode. Figure 5.1 is the CV for the deposition of Li on Ni. The open cell potential was about 3.4 V. At the beginning, the CV was scanned towards the negative direction until the strong negative current appeared at $-0.1$ V, which corresponded to the deposition of lithium. The additional reduction peak in the first cycle with an amplitude of about $-50$ µA at 0.8 V may be due to the decomposition of the electrolyte and the formation of SEI layer[98]. Different from the CV for Au (see Figure 5.6) as working electrode, there was only one significant oxidation peak with an amplitude of about 280 µA at 0.2 V. As shown by the CV curve near 0 V of the second and third cycles in Figure 5.1, the curve was almost linear and the slope was very steep at 0 V. This gave a clue that the deposition and dissolution of lithium on Ni was reversible. When the curves of the different cycles were compared, it could be confirmed that the CV curve demonstrated good reproducibility.

Figure 5.2 shows transients of potential, current and temperature up to 100 ms. Negative overpotential corresponds to lithium deposition and positive overpotential to lithium dissolution. The cell was kept for 10 ms at equilibrium potential before applying the potential pulse. Then, potential pulses with different overpotential (120 mV in Figure

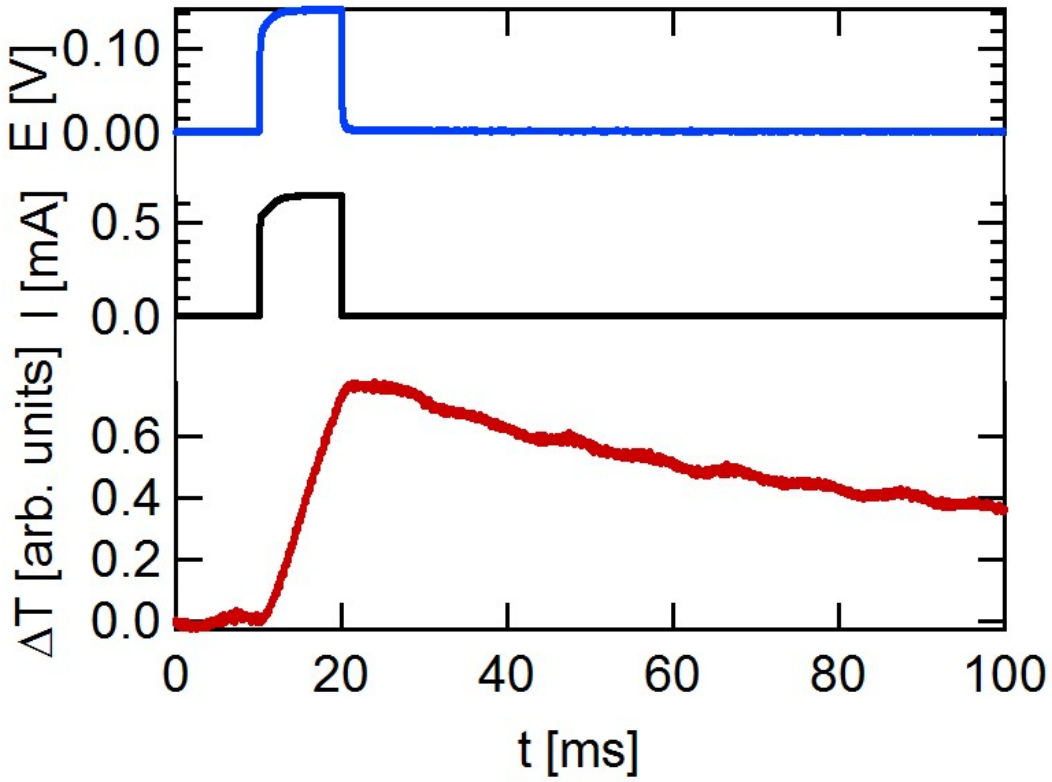


Figure 5.2. – A typical pulse including transients of potential (top, blue), current (middle, black) and temperature (bottom,red) up to 100 ms applied with positive overpotential using 1 M $LiPF_6$ in EC/DMC as electrolyte, Ni as WE, Li as RE and CE.

5.2) were applied between $t = 10\ ms$ and $t = 20\ ms$. After the end of the pulse, the cell was switched to OCP and the system relaxed to the thermal equilibrium within ca. 1 s. The amount of the converted lithium ions can be estimated through the integration of the current-time curve (the current transient in Figure 5.2). According to the calculation, the charge for the pulse in Figure 5.2 was about 30 µC/cm$^2$. Assuming a surface density of $10^{15}\ atoms \cdot cm^{-2}$, this charge corresponds to about 18% of a monolayer of Li, referred to a close packed Li layer. The temperature changed immediately with applying the pulse, which directly reflected the heat evolution during the potential pulse. Through calibration, the normalized heat during the reaction could be determined quantitatively. As previously reported by our group[42], the deposition of lithium had a cooling effect and lithium dissolution had a warming effect on the electrode. This behavior is also a clue for the reversibility of the reaction.

In Figure 5.3, the normalized heat for the dissolution/deposition of lithium with 1 M $LiPF_6$ as electrolyte was plotted as a function of the overpotential, that is, the amplitudes of the corresponding potential transients. Excellent linearity in plots of the normalized heat vs. the overpotential was obtained, with larger deviation from linearity for smaller

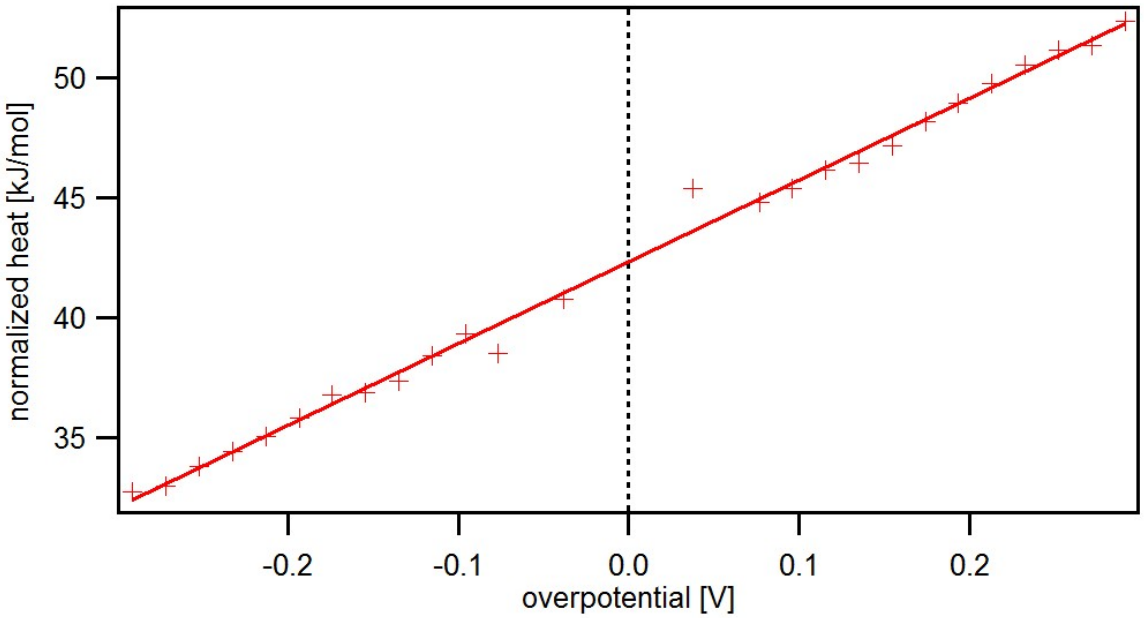


Figure 5.3. – The normalized heat of the dissolution (positive potential pulse) and deposition (negative potential pulse) of lithium versus overpotential using 1 M $LiPF_6$ in EC/DMC as electrolyte, Ni as WE and Li as RE and CE.

overpotential. According to Equation (2.19) in chapter 2, there were three main contributions to the heat: reversible heat due to the entropy change of the reversible process; the irreversible heat due to the polarization of the electrode; the Joule heat, which can be neglected in our case, because the pulse was very short (10 $ms$).

As mentioned in chapter 2, the molar heat of a reaction ($T \cdot \Delta_R S$) is also known as the Peltier coefficient ($\Pi$):

$$\Pi = T \cdot \Delta_R S \tag{5.1}$$

Both the entropy of the main electrochemical reaction and the entropy of sides reactions contributed to the molar entropy change $\Delta_R S$. In addition the transport entropy due to the transfer of electrons and ions also made a contribution to the Peltier coefficient[44]. However, the contribution of the transport entropy could be neglected because of the large Stokes radius of the lithium ion[42]. In order to obtain the reversible contribution to the normalized heat of the reaction, the data of all the pulses with different amplitudes was extrapolated to an overpotential of zero by linear fit (linear regression). In Figure 5.3, the Peltier coefficient (after calibration) for 1 M solution of $LiPF_6$ in EC/DMC was about $(45 \pm 3)$ kJ/mol.

We also checked the error of this measurement with the microcalorimeter. Firstly, the error of the temperature transients was examined by checking the signal-to-noise ratio. As expected, the error is larger for pulses with smaller overpotentials, that is smaller conversions. Secondly, the error for the Peltier coefficient of different measurements without

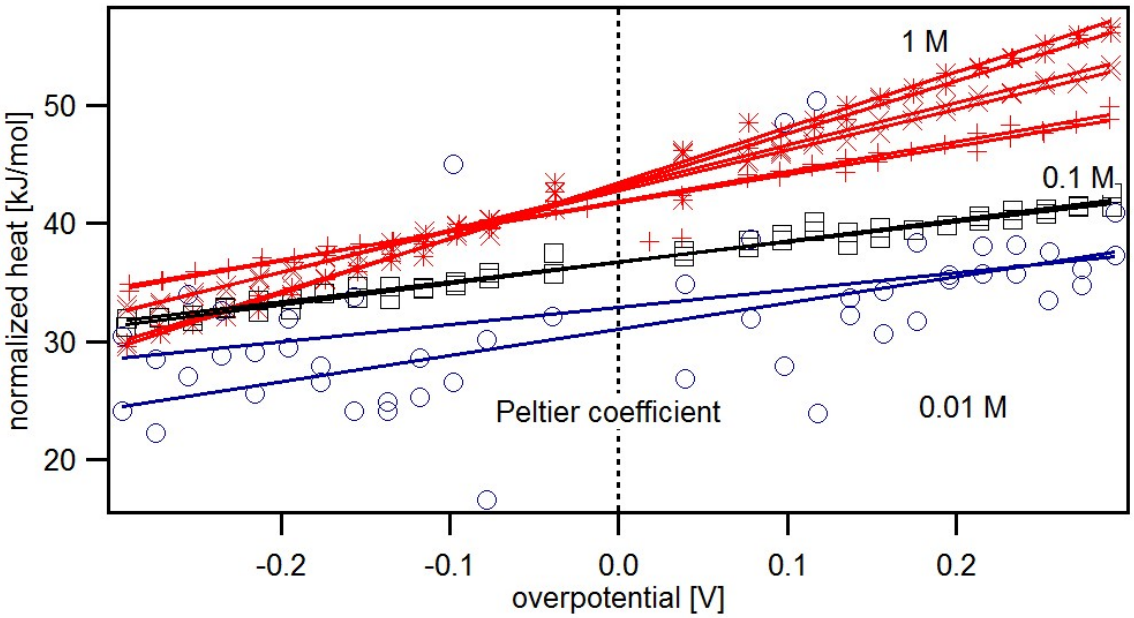


Figure 5.4. – The normalized heat of the dissolution (positive potential pulse) and deposition (negative potential pulse) of lithium versus overpotential for a series of measurements conducted in a 1 M, 0.1 M and 0.01 M $LiPF_6$ solution on Ni working electrode.

manually changing of the cell (statistical error) can be derived from the linear fit and is usually within the extent of 1% for 1 M and 0.1 M electrolyte, which shows that the linear extrapolation is a reasonable approximation and that the measurement exhibits good reproducibility. Typical deviations of the Peltier coefficient among different measurements within one experiment, i.e. without dismantling the cell, were of the order of 1 kJ/mol. However, the error of the data from different experiments is of the order of 6 kJ/mol, since the error of calibration procedure on the Ni WE should be considered.

The slope of the linear fit in Figure 5.3 demonstrates the increase of the contribution from irreversible heat with increasing overpotential, as shown by Equation (2.19) in chapter 2. In the ideal condition, the slope should be close to the Faraday constant. Nevertheless, the real measurement shows deviations mainly because of the electrolyte resistance, which induces a potential drop between working electrode and reference electrode. Therefore, the effective overpotential at the interface between electrode and electrolyte becomes lower than the amplitude of the potential pulse and the slope of the linear fit becomes smaller than the Faraday constant. But this deviation doesn't change the result of the Peltier coefficient, because the Peltier coefficient is obtained by extrapolating the overpotential to zero and is independent of the slope of the linear fit [52].

In this chapter, our aim is to obtain the Peltier coefficient of lithium deposition from electrolytes with different concentrations to gain information on the behavior of lithium ions upon dilution. As shown in Figure 5.4, the normalized heat for lithium deposition

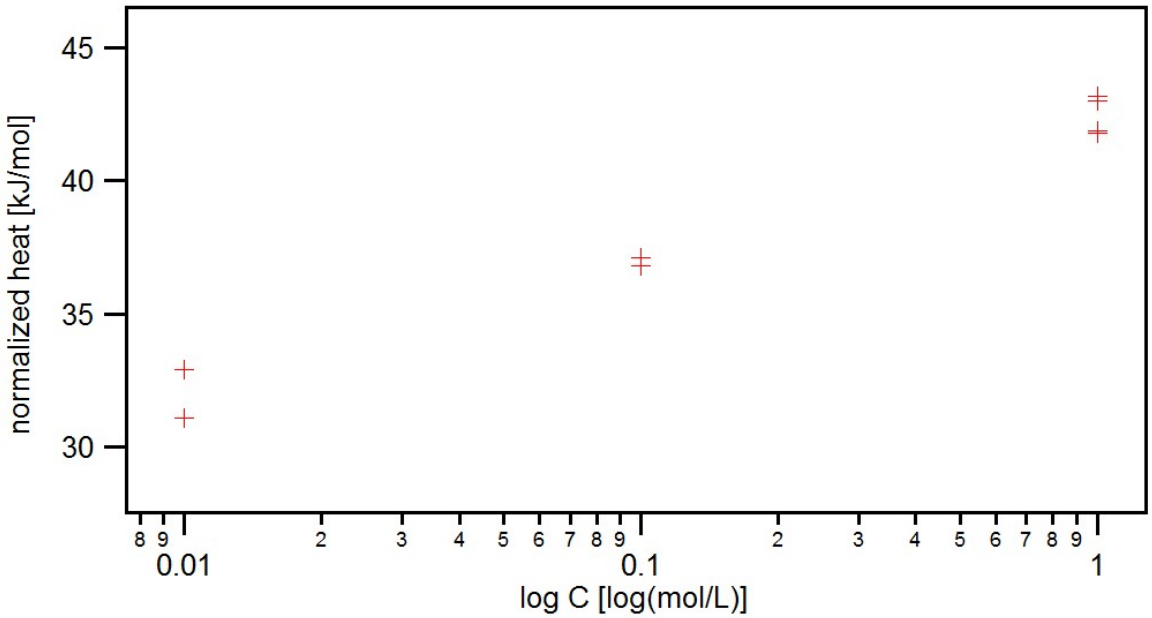


Figure 5.5. – The normalized heat of the dissolution and deposition of lithium versus the logarithmic concentration (dilution factor) for a series of measurements conducted in a 1 M, 0.1 M and 0.01 M $LiPF_6$ solution on Ni working electrode. It shows good reproducibility and regular decrease with the decrease of concentration of the $LiPF_6$.

from 1 M, 0.1 M and 0.01 M solution of $Li^+$ in EC/DMC for different potential pulse amplitudes was determined within one experiment without changing the configuration of the cell. We measured two sets of potential pulses for each electrolyte solution. At the interval of the two sets of the pulses, we waited at least 10 min until the system returned to the equilibrium. During washing of the cell, for example, before measuring of 0.1 M solution, we removed the electrolyte of 1 M concentration and rinsed the cell thoroughly using the 0.1 M electrolyte for three times. The transients of all pulses were checked. Most of the pulses were good except some pulses with small amplitudes, which had a low signal-to-noise ratio.

According to Equation (2.19) in chapter 2, the Peltier coefficient was obtained by extrapolating the overpotential to zero. As shown in the Figure 5.4, the Peltier coefficient decreases with concentration. The Peltier coefficient was $(45 \pm 3)$ kJ/mol for 1 M, $(40 \pm 3)$ kJ/mol for 0.1 M and $(35 \pm 3)$ kJ/mol for 0.01 M. The reliableness was examined by repeating the measurements of 1 M electrolyte. For example, after measuring the 0.1 M solution, we repeated to measure the normalized heat for the 1 M solution. The results were reproducible. The average difference of the Peltier coefficient for lithium deposition in 1 M electrolyte between the two measurements is less than 0.5 kJ/mol.

As shown in Figure 5.5, the difference between the Peltier coefficient for 1 M solution and the diluted solution is about 5 kJ/mol for a dilution by a factor of 10. For a dilution

of 100, the difference of Peltier coefficient is about 10 kJ/mol. Any time dependent changes or aging effects can be neglected, because the first and the corresponding repeated measurements exhibited the same results. It is noteworthy that the slope of the linear regression becomes slightly smaller with decreasing electrolyte concentration. This is due to the increasing electrolyte resistance and larger ohmic drop at the lower concentrations of electrolytes.

We repeated the whole experiment five times. Some of the experiments demonstrated a slightly larger Peltier coefficient (e.g. 48 kJ/mol for the 1 M $LiPF_6$ electrolyte). However, all of the differences for the Peltier coefficient were in the order of $(5.0 \pm 1.5)$ kJ/mol for a dilution by a factor of 10 and $(10 \pm 2)$ kJ/mol by a factor of 100. Occasionally, the Peltier coefficient for the very first lithium deposition was smaller than that of all the following measurements of the same concentration of electrolyte. This is reasonable when we considered the decomposition of the electrolyte and the formation of SEI layer while the lithium was deposited on the working electrode. Therefore, we attribute this heat effect to side reactions due to the building of a SEI layer, which was continued during the pulses. We therefore disregarded the results of the first Li deposition experiment of a series of measurements.

### 5.2.2. Lithium deposition on a Au working electrode

In addition to experiment of Li deposition on Ni WE, we also used Au as WE. It turned out that alloying of Li and Au distorts the microcalorimetric measurements. Since the corresponding deposition measurements are still of relevance, we present them in the following.

When Au was chosen as WE, three main processes were involved: the decomposition of electrolyte (reports were found for both the solvent[99] and solute[100]), the formation of SEI layer and the alloying process with lithium. These processes were confirmed by in situ STM[101] and in situ TEM[99]. Yet, it's difficult to distinguish these processes from TEM images[99]. However, at the potential where lithium was deposited, the alloying between Au and Li should be the dominant process, considering that the formation of SEI layer was observed above 0.7 V[102]. An atomic resolution STM, TEM and X-ray studies of Li and Au ordering in Au electrode revealed that a $Au_3Li$ structure in coexistence with the pure Au lattice planes (111)[99, 103, 104]. To evaluate the influence of the alloying process on the deposition of lithium, cyclic voltammetry and electrochemical microcalorimetry were performed.

Figure 5.6 shows the CV for 1 M $LiPF_6$ on Au (WE) with Li as RE and CE and $LiPF_6$ in EC/DMC (1 M) as electrolyte. It was recorded, starting from 3.2 V, which was repetitively scanned between -0.1 V and 1.7 V. The first reduction peak appeared at 2 V, which had a current density of $-300\ \mu A/cm^2$ and a charge of $-4\ mC/cm^2$. As the scan went on,

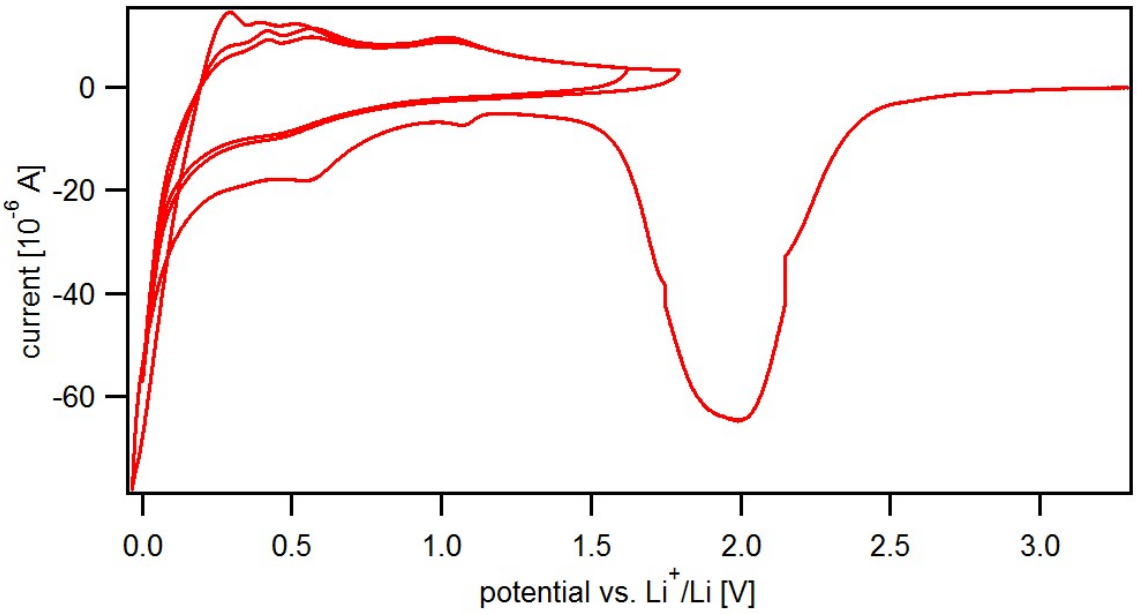


Figure 5.6. – The cyclic voltammogram for the solution of 1 M $LiPF_6$ in ethylene carbonate (EC) and dimethyl carbonate (DMC) on an Au working electrode with lithium as RE and CE electrode. The CV was recorded, starting from 3.2 V, which was repetitively scanned between -0.1 V and 1.7 V.

another two reduction peaks with smaller amplitude appeared at 1 V and 0.5 V, which might correlate to the decomposition of the electrolyte[98]. When the potential came close to −0.1 V, the formation of an alloy between Au and Li was expected[99, 101] while the lithium was deposited on the Au working electrode. This process was not reversible, which could be confirmed by the absence of a sharp oxidation peak in the CV curve. There was only one oxidation peak with a small amplitude of 50 $\mu A/cm^2$. In addition, the oxidation peaks for the CV curves in different cycles were not reproducible.

By spatially resolved EELS spectra, it was found that the Au was covered with a layer of Li−Au alloy[99]. Under the assumption that the layer of Li-Au alloy may prevent the Au from further alloying, we deposited about 6000 monolayers of lithium on the Au working electrode and performed the microcalorimetric measurements. Using the $LiPF_6$ electrolyte (1 M, in EC/DMC), ten heat measurements of Peliter coefficient $\Pi$ were obtained. Figure 5.7 shows the plots of the normalized heat vs. the overpotential with 1 M $LiPF_6$ in EC/DMC as electrolyte. It could be found that there were significant differences among the measurements. In addition, most of the curves show a much lower value of the normalized heat (between 25 kJ/mol and 10 kJ/mol) than that we obtained using Ni as working electrode. It could be expected that the alloying process continued while the microcalorimetric measurements were performed. Therefore, the Au-Li layer wasn't sufficient to prevent the Li and Au from further alloying.

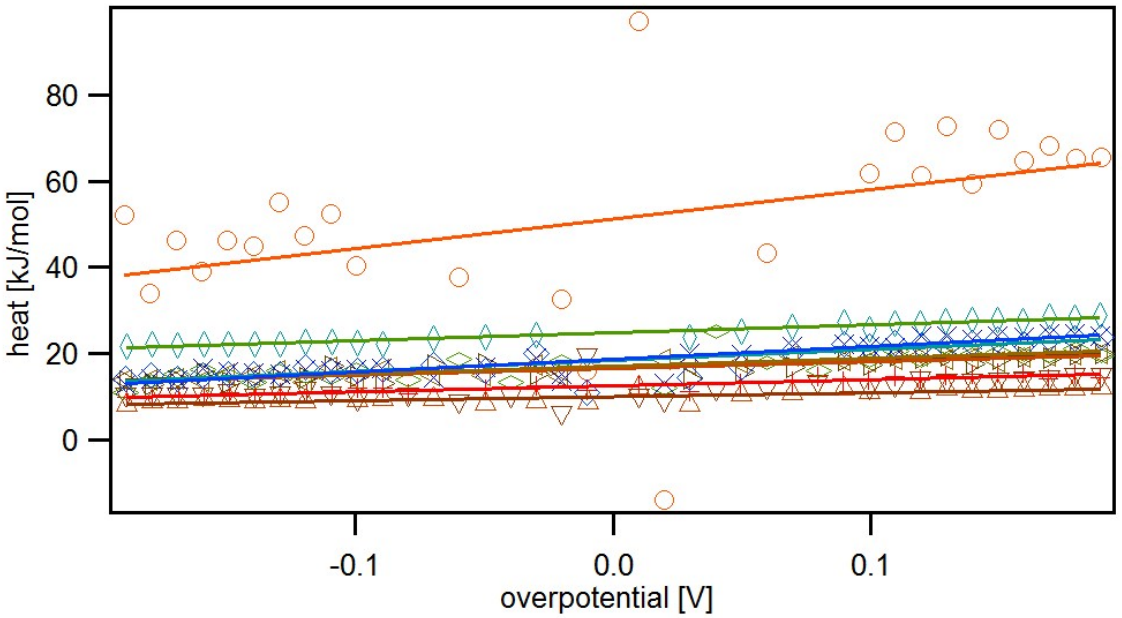


Figure 5.7. – The normalized heat of the dissolution (positive potential pulse) and deposition (negative potential pulse) of lithium versus overpotential for a series of measurements conducted in a 1 M $LiPF_6$ solution and on Au working electrode.

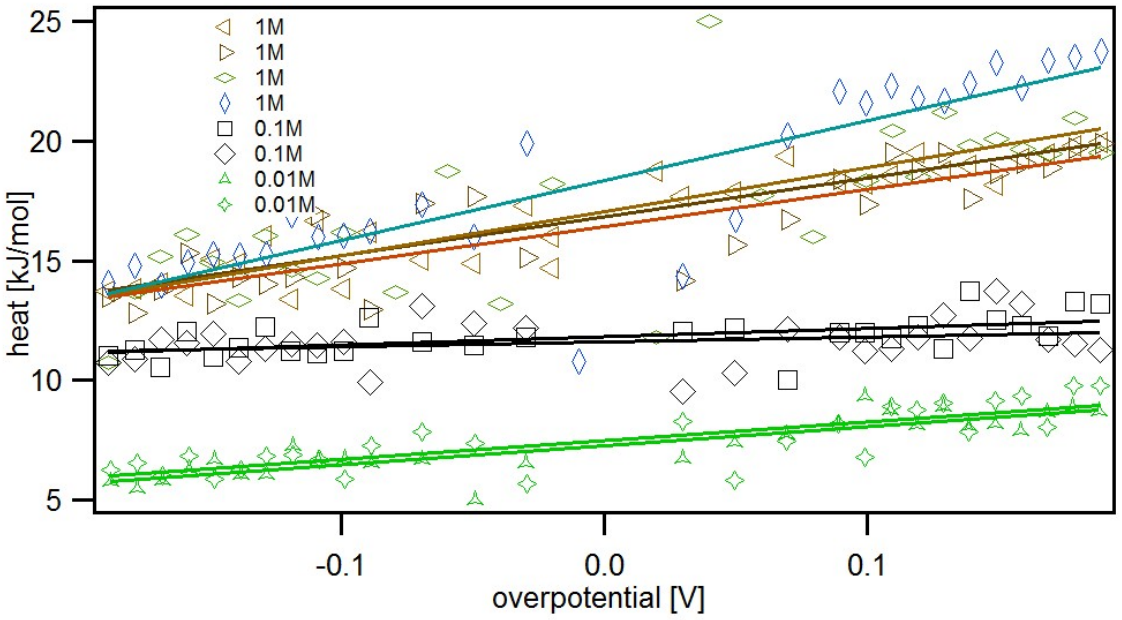


Figure 5.8. – The normalized heat of the dissolution (positive potential pulse) and deposition (negative potential pulse) of lithium versus overpotential for a series of measurements conducted in a 1 M, 0.1 M and 0.01 M $LiPF_6$ solution and on Au working electrode.

The comparison of the normalized heat using electrolyte of different concentration was conducted in Figure 5.8. Even though the values of the normalized heat were small for all measurements with Au as WE, the relative relation among the measurements are clear. As shown in Figure 5.8, the normalized heat was larger for the electrolyte ($LiPF_6$ in EC/DMC) with higher concentration ($1M > 0.1M > 0.01M$). When the electrolyte was diluted by a factor of 10, the normalized heat decreased by about 5 kJ/mol; for a dilution factor of 100, the normalized heat decreased about 10 kJ/mol. Within error bar, the decrease of the Peltier coefficient upon dilution of the electrolyte was therefore, the same as that found for the lithium deposition on Ni working electrode.

Even though the WE demonstrated a significant improvement for calibration over the Ni WE, it is not stable when lithium was deposited on it. The results show that Au is not suitable as a working electrode for studying the deposition of lithium, because of the alloying process.

## 5.3. Discussion

Microcalorimetric measurements of lithium deposition using Au and Ni as the WE show that the observed dilution effects on the Peltier coefficient are indeed independent of the substrate and hence stem from variations of the entropy of the Li ions in solution.

### 5.3.1. Concentration effects on the lithium deposition

The following discussion closely follows the Reference [75]. The entropy (S or $\Delta S$) is a state function, which means that its value is path independent. It has a positive sign when the entropy of the system increases and the system becomes more disordered and vice versa[43]. In addition, the reaction pathways for electrochemical lithium deposition from the different concentrations have the same thermodynamic final state but a different starting one. Therefore, the differences in the Peltier coefficient of the lithium deposition, corresponding to the entropy of the process, resulted from changes in the entropy of the solvated lithium ion in the solution for different concentrations. During the dilution of the electrolyte, three effects were included: changes in coordination, the formation of ion contact pairs and the entropy of dilution.

The dilution effect on the reaction entropy during lithium deposition can be readily calculated. The changes of the entropy of the $Li^+$ ion ($S_{Li^+}$) correlates with its activity $a_{Li^+}$ according to the following equation[50]:

$$S_{Li^+} = S^o_{Li^+} - Rlna_{Li^+} - RT((\partial lna_{Li^+})/(\partial T)) \tag{5.2}$$

where $S^o_{Li^+}$ is the standard molar entropy of $Li^+$ and $a$ is the activity of the ions. The temperature dependence of the activity can be neglected, because it's usually small. Under the assumption that the activity can be approximated by the concentration of the electrolyte, the entropy change due to dilution could be denoted as the following equation:

$$\Delta S_{dil} \approx -Rln(\frac{c_2}{c_1}) \tag{5.3}$$

Therefore, the corresponding change of the Peltier coefficient is:

$$\Pi \approx -RTln(\frac{c_2}{c_1}) \tag{5.4}$$

According to Equation (5.4), the Peltier coefficient will decrease by 5.7 kJ/mol when the dilution factor was 10 and by 11.4 kJ/mol when the dilution factor was about 100. These calculated values are close to the experimental results of $(5.0 \pm 1.5)$ kJ/mol and $(10 \pm 2)$ kJ/mol. Since the electrolytes are not ideal dilute solutions, there will be deviation due to the change of the activity coefficient of $Li^+$ in the different concentrations. In the concentration range between 0.01 M and 1 M, the activity coefficient is smaller than one, with stronger deviations for higher concentrations. Therefore, it will lower the effect of dilution on the Peltier coefficient if activities is considered instead of concentrations. If the Davies equation is employed, which is an extension of the Debye-Hückel equation for higher concentrations [105], it will result in a reduction of the Peltier coefficient to 5.4 kJ/mol for dilution by a factor of 10. Therefore, the dilution entropy of solvated $Li^+$ provides a reasonable interpretation for our experimental results. In addition, it is also necessary to discuss other possible contributions.

The effect of changes in the coordination of $Li^+$ with electrolyte concentration also makes a contribution to the changes in the solvation of $Li^+$ ions. It has been found by various methods, such as Raman-, IR-, and NMR-spectroscopy as well as by DFT- and MD-calculations that the coordination number of $Li^+$ increases upon dilution, e.g., in solutions of $LiClO_4$ in EC, $LiBF_4$ in MEC (methoxymethyl ethylene carbonate) and $LiBF_4$ in EC/DMC[89–91, 106]. However, in those reports, contributions from inner and outer solvation shells are not discriminated.

Previous report from our group showed that there were about 4 coordinated solvent molecules in the inner shell of lithium ion and that the entropy of lithium deposition is mainly due to the entropy gain of the solvent molecules when they are released from the inner solvation shell upon deposition of the $Li^+$ ion[42]. The contribution to the entropy change by the liberation of solvent molecules from the inner solvation shell upon lithium deposition was estimated to be about 42 J mol/K for 1 M $Li^+$ in EC:DMC, referred to the one mole of liberated solvent molecules. In other words, the Peltier coefficient will increase

by about 12 kJ/mol for an increase of the coordination number in the inner solvation shell by about one upon dilution.

According to our data, however, we determined a decrease of the Peltier coefficient upon dilution, which can be fully interpreted as the entropy of dilution. Note that activity variations with concentration cannot compensate for changes in the inner coordination shell, since the effect of activity also tends to lower the differences of the Peltier coefficients upon dilution, as discussed above. We therefore expect that the inner shell coordination of $Li^+$ ions is not changing considerably upon dilution and that the reported changes of the coordination number of $Li^+$ with concentration rather reflect changes in the coordination beyond the first coordination shell.

Finally, we consider the effect of the formation of ion contact pairs as a third contribution to the entropy changes in the solvation of $Li^+$ ions with different concentration. Ion pairs formation (association) is favored in electrolytes with small permittivity and/or high concentration. Contact pairs between lithium and its counterion have been identified in various salts and solvents using Raman- and IR-spectroscopy[89, 106, 107], Hartree-Fock, MD and DFT calculations[91, 93, 108], and conductivity measurements[95]. The extent of ion contact pair formation also has been discussed in literature. Qiao *et al.* studied the ion contact pair formation of $LiBF_4$ in 4-methoxymethyl-ethylene carbonate (MEC) at different temperatures[106]. They reported a Raman band corresponding to ion contact pair interactions even for their measurements with the lowest concentration (0.26 mol/L). The intensity of the band increased with concentration. Tasaki *et al.* calculated the solvation of lithium in a 1 M electrolyte with propylene carbonate (PC) and reported a partial solvation number for $Li^+$ by $PF_6^-$ ions of 0.35, which can be interpreted as a measure for the contact ion pair concentration[93]. Salomon and Plichta measured the conductivity of various Li-electrolytes and derived the activity of the ions and the thermodynamic association constant using the Fuoss-Hsia equation[95]. For $LiClO_4$ in PC they found an association constant $K_a$ of 1.3 L/mol which corresponded to about 31% ion pairs at 1 M.

In this chapter, it is difficult to predict the extent of solvation of ion contact pairs. Since they possess only a dipole moment but no net charge, the extent of solvation might initially be expected to be reduced compared to the single ions. Therefore, lithium deposition from ion pairs should liberate less solvent molecules than deposition from isolated solvated $Li^+$ ions. The formation of a free anion upon lithium deposition can be neglected in this context because it is generally very weakly solvated[109]. Since the fraction of contact ion pairs should decrease upon dilution, their effect on the Peltier coefficient should oppose the influence of dilution entropy, as discussed above. Therefore, the differences between the Peltier coefficients for the different concentrations should be decreased by the formation of ion pairs. According to our results, however, we see no such effect within our error margins. This suggests that the solvation entropy of ion pairs is similar to the solvation

entropy of free lithium ions. Indeed, on the molecular level only one side of the $Li^+$ ion is shielded by its counterion. On the unshielded side, the neighboring solvent molecules of $Li^+$ ion will be strongly polarized. This assumption is supported by DFT-calculations of Tasaki *et al.*, who found that there was almost no variance of energy for the desolvation of lithium in ion pairs compared to solvated lithium ions at 1 M concentration[93].

### 5.3.2. Transport heat

According to Equation (2.16) in subsection 2.1.2, M. Schmid calculated the transport heat for lithium deposition with lithium as RE and CE, Ni as WE and $LiPF_6$ (1 M) as the electrolyte. The calculated transport heat $Q^*$ was about $-0.6\,\mathrm{kJ/mol}$ [23]. We assume that the variance of concentration (between 0.01 M and 1 M) of the electrolyte doesn't change the transport heat significantly. Therefore, the transport heat can be neglected for the above discussion.

## 5.4. Conclusion

Using microcalorimetry, the Peltier coefficient for electrochemical Li bulk deposition on Ni or tungsten working electrodes from electrolytes of $LiPF_6$ in DMC/EC with different $Li^+$ concentrations was determined. The entropy of transport can be neglected in such electrolyte solutions because of the small contribution of entropy of transport. Therefore, the Peltier coefficient for the Li deposition directly reflects the entropy change upon the electrochemical Li deposition reaction. The Peltier coefficient decreased by $(5.0 \pm 1.5)\,\mathrm{kJ/mol}$ by reducing the $Li^+$ concentration from 1 to 0.1 M and by $(10 \pm 2)\,\mathrm{kJ/mol}$ from 1 M to 0.01 M. If we assumed that the electrolytes were ideal solutions, we obtained a decrease of the Peltier coefficient by $5.7\,\mathrm{kJ/mol}$ upon dilution of the electrolyte concentration by a factor of 10. Therefore the measured variations of the Peltier coefficient can be well interpreted by the dilution entropy of the solvated $Li^+$ ion.

Normally, the change of the inner shell coordination number of $Li^+$, or the formation of ion pairs should reduce the variances of the Peltier coefficient among the investigated concentrations range. Therefore, we neither found significant changes of the activity coefficient nor of the inner shell coordination number of the $Li^+$ ions. Furthermore, although there was report of the formation of ion contact pairs for electrolytes similar to the one used in this study, we didn't find evidence of the contribution of ion pairs to the reaction entropy of lithium deposition. This indicates that ion contact pairs are similarly solvated as lithium ions at $Li^+$ concentrations between 1 M and 0.01 M.

In addition to experiment of Li deposition on Ni WE, we also used Au as WE. However, the alloying of Li and Au distorts the microcalorimetric measurements. Even though the values of the normalized heat were small for all measurements with Au as WE, the

relative relation among the measurements are clear. The normalized heat was larger for the electrolyte ($LiPF_6$ in EC/DMC) with higher concentration ($1M > 0.1M > 0.01M$). When the electrolyte was diluted by a factor of 10, the normalized heat decreased by about 5 kJ/mol; for a dilution factor of 100, the normalized heat decreased about 10 kJ/mol.

Nowadays, there were investigations of superconcentrated $Li^+$ based electrolytes with $Li^+$ concentrations exceeding 2 M for applications, e.g., in high rate of charging of Li ion batteries[110]. At high concentrations of $Li^+$, the $Li^+$ ions are interpenetrating the inner solvation shell and the electrochemical properties of the electrolyte deviate significantly from that of the ideal solution[111]. It is expected in our system, for $Li^+$ concentrations beyond 1 M, that the effects of the changes of the inner coordination shell and the formation of ion pairs on the Peltier coefficient may roughly overcompensate the variations due to the dilution of the electrolyte. Therefore, the Peltier coefficient may eventually reverse its sign for superconcentrated Li electrolytes.

# 6. Phase transition during lithium intercalation in graphite electrodes

Graphite, as a typical layered material, is widely used as anode active material in commercial Li-ion batteries due to its light weight and low voltage. The light weight leads to a high gravimetric capacity of graphite (theoretical capacity: 372 mA h/g [112]). And a lower voltage is beneficial for graphite as anode materials to provide a wider potential window for full cells. Li was used as anode electrode (standard electrode potential of Li: −3.04 V), because Li has a lower voltage than most of the metals. (Only strontium, calcium and praseodymium have a more negative potential than lithium. But they are less competitive because of their larger density.) However, lithium metal is flammable which leads to serious safety problems. Since the potential of the intercalated graphite is close to that of lithium (electrode potential of graphite versus $Li/Li^+$: 0.1 V [113]), graphite is an ideal alternative to Li metal as anode electrode. In addition, graphite is stable under ambient conditions and provides a good compromise between cycling behavior and specific capacity[114]. By combining graphite with a lithium containing cathode, lithium can "rock" from one side to the other during charging and discharging (i.e. "rocking-chair" mechanism)[115]. With this model, the intercalation and deintercalation of lithium is well described.

At the beginning of the intercalation, the lithium ions intercalate alternatingly into graphite layers and leave several unoccupied layers between two layers of intercalant instead of occupying all the available interlayers[116]. As shown in Figure 6.1, this character appears periodically for graphite anodes and is known as stage phenomenon. Stage-n means a sequence of n unoccupied layers and an intercalated layer, which forms a specific phase and repeats until the phase boundary. Normally, the formula of the staged phases is denoted as $Li_xC_6$, where $x$ is the state of charge. For example, $x = 0.5$ corresponds to the composition of a half insertion (stage-2)[117]. According to literature, various stages appear during lithium insertion[118–120]. Studies demonstrated that the sequence of the stages for charging was of the following form[115, 121]:

$Graphite \rightarrow dilute1 \rightarrow stage4 \rightarrow stage3(\rightarrow stage2L) \rightarrow stage2 \rightarrow stage1$

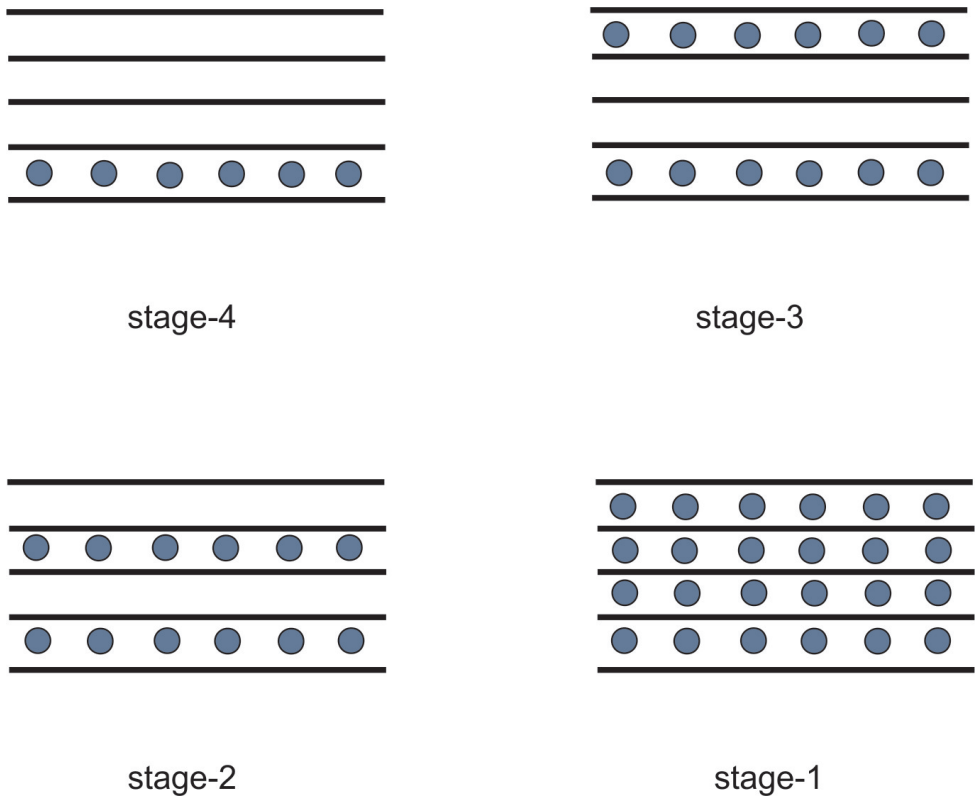


Figure 6.1. – Schemes of a lateral view of four phases (stages) of the Li-graphite intercalation compound.

Here, dilute 1 denotes a phase in which lithium ions are intercalated randomly within the graphite and stage 2L denotes a liquid-like stage 2 phase which has no in-plane ordering[122].

Many methods were used to study the mechanism for the phase transitions (the change of the stages). Safran explained the stage phenomenon with the competition between the in-plane attractive force and the inter-layer repulsive force of the intercalated lithium[123]. Electrochemical insertion of lithium ions into the hosts in graphite might proceed through the formation of a solid solution or by first-order phase transitions, during which nucleation processes could be observed[124, 125].

With chronoamperometric measurements and modeling of nucleation and growth, Levi M.D. *et al.* studied quantitatively the transition from stage 2 to stage 1 during electrochemical insertion of Li ions into graphite[124]. Aurbach obtained a cyclic voltammogram with a scan rate of 4 µV/s to demonstrate the relation of potential and current for the phase transition during charging and discharging of lithium ions with graphite[126]. In addition to the current and the potential information of the cell, thermodynamic studies are also necessary to understand the mechanism of the cell and improve the cell performance. From the perspective of engineering, thermal management is also one of the challenges in aggressive environments for energy storage devices[21]. For fundamental studies, crucial conditions, such as in situ and non-destructive measurement techniques,

are prerequisite[22]. Combined with thermodynamic experimental methods which provide empirical parameters for the simulation, the mechanism of the cell reaction could be understood more clearly.

Nowadays, the experimental methods for investigating the thermodynamic of the insertion of lithium into graphite are limited. Differential thermal analysis (DTA) was performed to determine the formation enthalpies of $LiC_6$ and $LiC_{12}$[127]. The entropy change and enthalpy of lithium intercalation could also be obtained by measuring the temperature dependence of the open-circuit potential of lithium half-cells[20–22]. Filhol[128] showed that it's not accurate to relate the open circuit voltage (OCV) with the small free enthalpy variations in Li-graphite batteries, considering the relation between OCV and free enthalpy (See Equation (2.7)). Without changing the temperature of the cell, the potentiostatic intermittent titration technique (PITT) and galvanostatic intermittent titration technique (GITT), which applied potential and current pulses respectively during charging and discharging, were powerful tools to study the processes of phase transitions[129]. However, a GITT or PITT measurement could last for weeks, since much time during the entropy measurement was wasted during potential relaxation after the cell was turned to open cell potential mode. An alternative method without sacrificing the accuracy is to measure the temperature response to a charging pulse even though the potential don't return to the equilibrium[22]. In addition, the measurement of the Peltier coefficient and entropy for half cell should be reversible, which means the amount of reaction should be small.

Various simulation methods were performed to interpret the mechanism for charging and discharging. The density-functional theory (DFT) or ab initio studies were applied to interpret the potential profile very well when the Van der Waals force between the graphene planes was considered[130, 131]. By including the entropy term and the intercalation pressure, the simulation of the potential steps agreed well with the experimental results[132]. The phase change during the charging and discharging were interpreted by means of a lattice-gas model using the mean-field approximation and Monte Carlo simulations[47, 115, 123]. With the improvement of the calculation ability and the optimization of the software, simulations with multiscale physical models could be performed from a few atoms to the device level which can predict the behavior of the materials and their time evolution[133–135]. These models and the simulation methods may be improved when experimental results are used as input.

In this chapter, electrochemical microcalorimetry, which can induce a very small extent of reaction by applying 10 ms long current pulses, was used to obtain the temperature transients during the charging and discharging processes of Li-graphite half cells (lithium as RE and CE, graphite as WE). The Peltier coefficient and the entropy of the electrode reactions can be obtained. The lattice-gas model was used to calculate the reaction entropy of lithium intercalation in the graphite electrodes.

# 6.1. Experiment

## 6.1.1. Chemicals, materials and cell

The lithium hexafluorophosphate ($LiPF_6$) in ethylene carbonate (EC) and dimethyl carbonate (DMC) ($EC : DMC = 1 : 1$) was purchased from BASF (battery grade). We used lithium wire (the diameter: $\phi = 0.2$ mm) as reference electrode (RE) and counter electrode (CE). The working electrode (WE) was a thin layer of graphite, coated on a copper foil, which was provided by Michael Hess from Prof. Petr Novák's group at the Paul Scherrer Institute (Villigen, Switzerland).

The graphite used in this experiment was polycrystalline graphite of SFG6 type (TIMCAL). It had a large surface area of about 17.1 $m^2/g$ (BET-isotherm). The graphite electrode was prepared by mixing graphite, polyvinylidene fluoride (PVDF) as binder (Kynar Flex) and super-P carbon (TIMCAL) as conductive filling materials in the ratio of 87:10:3 (weight percent). N-Methylpyrrolidine was used as solvent for PVDF. The mixture was stirred until a homogeneous slurry was formed. The slurry was coated on a 25 µm thick copper foil using a simple doctor blades method. An about 9 µm thick graphite layer was formed. It was dried under 80 °C. More information about the preparation precess could be found in the Reference [136].

The graphite electrode was cut in round shape with a diameter of 9 mm. The graphite layer on the margin of the WE was removed using a well designed setup provided by the mechanical workshop in the institute of physical chemistry of the KIT. The setup has a supporter to hold the WE, on top of which the WE was fixed by pressing the WE with a ring, so that the middle part of the WE was intact. Then the WE was rotated and the graphite on the edge was removed with a knife, following by polishing with sand paper along the vertical (to the radial) direction. After the graphite electrode was dried at 120 °C for 24 hours under vacuum, the graphite electrode was transferred into glovebox. More detail information about the preparation and characterization of the graphite electrode could be found in Reference [136].

To avoid the leakage of electrolyte, an O-ring (from C. Otto Gehrckens GmbH & Co. KG; inner diameter: 5 mm; cord thickness: 1 mm) was used, which also plays an important role to keep the sensor and WE closely contact when the air between the cell and its supporter was evacuated. This O-ring was put inside a copper ring, which was used as conductor between the WE and the current collector (made of copper). The copper ring couldn't be put on the working electrode directly, because the mechanical strength of the copper foil and the sensor was not sufficient to distribute the stress due to the pressing of the copper O-ring, leading to a damage of the sensor. Therefore, we used a sapphire sheet (from Kyburz Sapphire, thickness: 50 µm) between the sensor and the WE.

The cell was made of PCTFE (polychlorotrifluoroethylene) (KEL-F). It is stable with the $LiPF_6$ solution and doesn't react with the lithium. In addition, the cell could withstand a mixture of $H_2SO_4$ and $H_2O_2$ (with a ratio of 1:1) for washing. Because the cycling and charging/discharging of the electrochemical cell is time-consuming, it usually costs days to finish one experiment. Therefore, we need to consider the consumption or the evaporation of the electrolyte in our system. The vapor pressure for the solvent of the $LiPF_6$ solution is about $9.8 \times 10^3$ mmHg for EC and 55.36 mmHg for DMC at room temperature. The high vapor pressure for EC minimizes its evaporation, while the DMC is easier to evaporate compared with EC. To minimize the evaporation of the solvent, we covered the cell with a lid. But the cell was not completely sealed, because the RE and CE went through the lid. However, the evaporation of the electrolyte could be neglected, as we determined from the filling level of the cell at the end of the measurement. Even though gas may be produced due to the decomposition of the electrolyte, the gas could still be neglected because of its small extent.

### 6.1.2. Cycling and microcalorimetric measurements

All the experiments in this part were conducted in the glove-box. The cycling was performed with a current of $\pm 0.04$ mA between 0.05 V and 1.5 V. Nine cycles were performed and it took about 3 h for each cycle.

In the microcalorimetric experiment, the cell was charged (or discharged) to a certain potential, followed by switching the cell to OCP mode through electrically interrupting the outer cell circuit and staying at OCP mode for 10 seconds. Then, 10 or 20 current pulses using negative and positive overpotential were applied with different amplitudes for each measurement of pulses. After the pulses, the setup was kept at OCP mode for 5 seconds before switching to cell mode. It usually took less than one minute for each series of pulses in this measurement. According to the methods to treat the pulses, as described in chapter 3, the Peltier coefficient was obtained after calibration and fitting. In this experiment, there was no need to change the configuration of the cell. The electrochemical measurement was controlled and recorded by a procedure based on Igor Pro software (WaveMetrics) while the cell was in the glove box ($O_2 < 4\ ppm$; $H_2O < 0.5\ ppm$).

## 6.2. Results

### 6.2.1. Results of cycling

To investigate stability and lifetime of the graphite electrode (i.e. cyclability), cycling of the electrochemical cell was performed. The cycling included two parts: charging and discharging. Figure 6.2 shows the cycling for the graphite half cell with graphite as

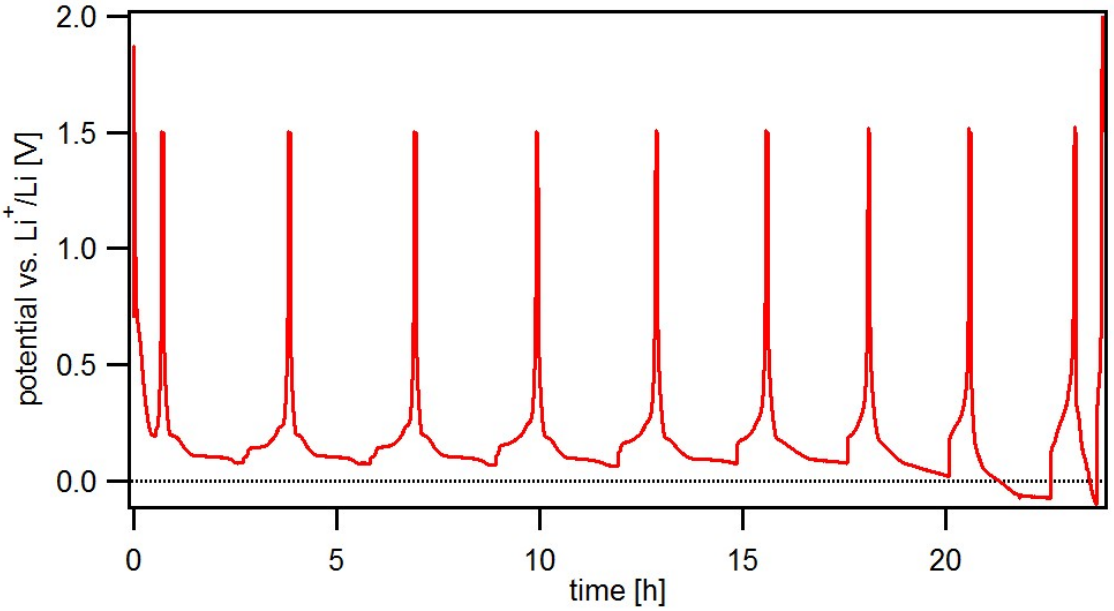


Figure 6.2. – The cycling of graphite half cell with Li as reference and counter electrode, 1 M $LiPF_6$ solution (in EC and DMC, 1:1) as electrolyte. The current was ±40 µA.

working electrode, Li as reference and counter electrode and 1 M $LiPF_6$ solution (in EC and DMC, 1:1) as electrolyte. The system was kept at OCP for 10 minutes after each charging and discharging. Then, constant current mode was applied for both charging (−40 µA) and discharging (40 µA). The first cycle started from 3.4 V and the graphite working electrode was charged to about 0.2 V. In the ninth cycle, the plating on the WE occurred when the cell was charged below 0 V. From the second cycle to the eighth cycle, the cell was cycled between 0.05 V and 1.5 V. Nine cycles, in total, were obtained in this measurement, while during the first cycle the cell wasn't deeply charged and the ninth cycle exhibited the plating of lithium. Therefore, only seven cycles were evaluated (from the second cycle to the eighth cycle).

The corresponding current curve of Figure 6.2 for the cycling of the Li-graphite half cell is shown in Figure 6.3. The spikes in the curve were due to the artifacts (signal noise) from the potentiostat. For the first five cycles, the duration of each cycle was about 3 h. From the sixth cycle, the duration of the cycles decreased quickly, which indicated the degradation of the cell. Some error due to the potentiostat was found for the current. For example, in the second discharging process, the current didn't reach the programmed value of 40 µA, but increased firstly to ca. 30 µA instead and then to 40 µA. The curves for the increase were not uniform.

Figure 6.4 shows the potential curve for the second charging of the graphite working electrode in Figure 6.2. The cell was charged from 1.5 V to 0.05 V. At the beginning, the potential of the cell decreased very quickly to ca. 0.6 V. The quick decrease of the

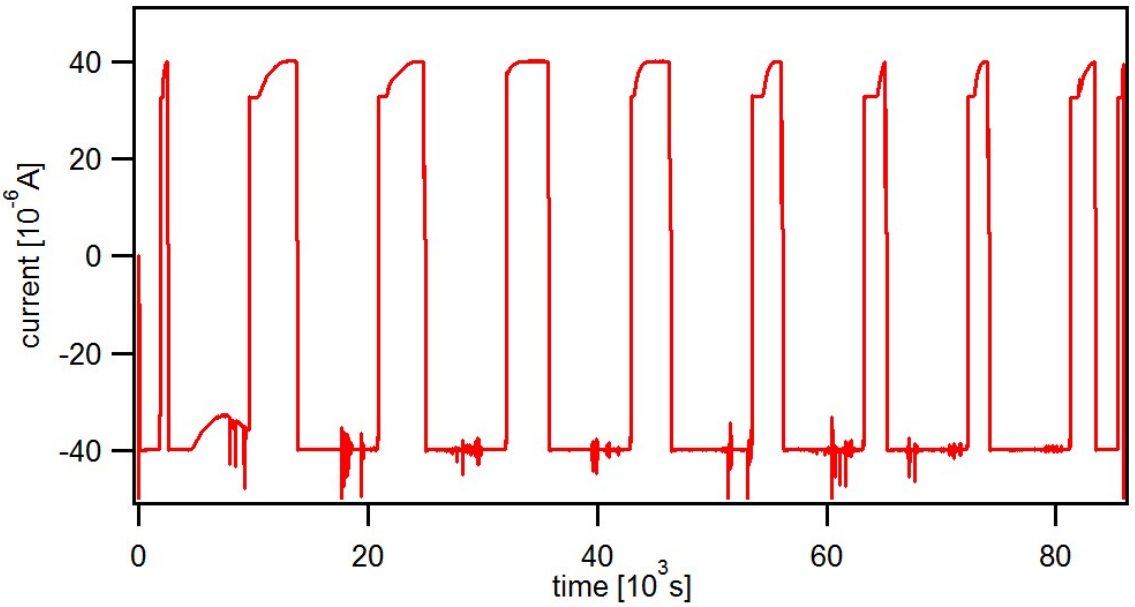


Figure 6.3. – The current curve for the cycling of the graphite half cell with Li as reference and counter electrode, 1 M $LiPF_6$ solution (in EC and DMC) as electrolyte.

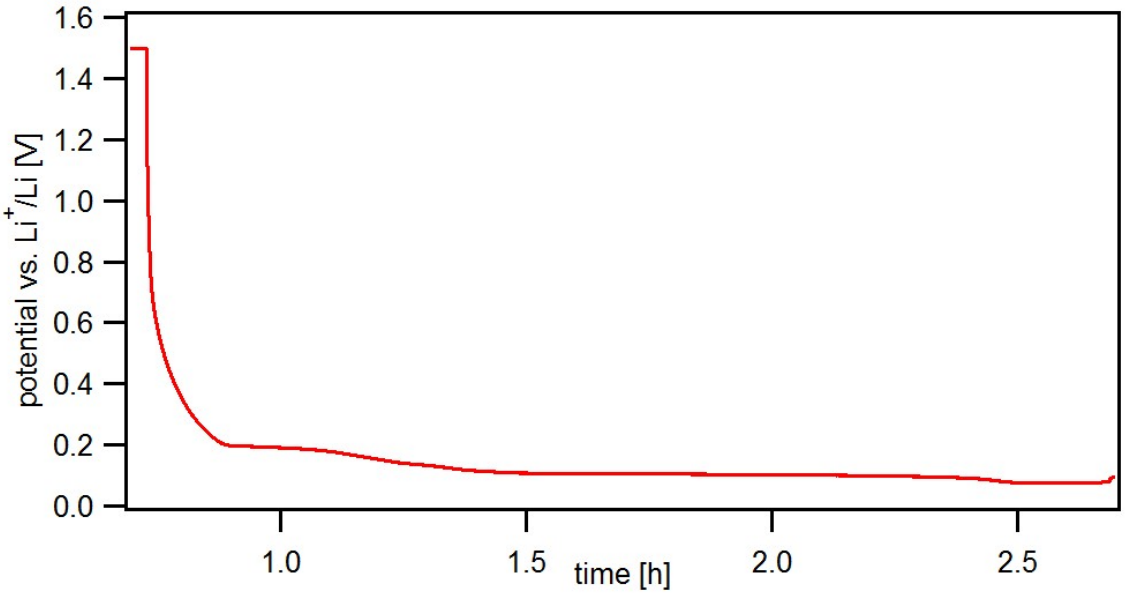


Figure 6.4. – The potential curve for the second charging of a graphite working electrode with Li as reference and counter electrode, 1 M $LiPF_6$ solution (in EC and DMC) as electrolyte. The current for charging was −40 µA.

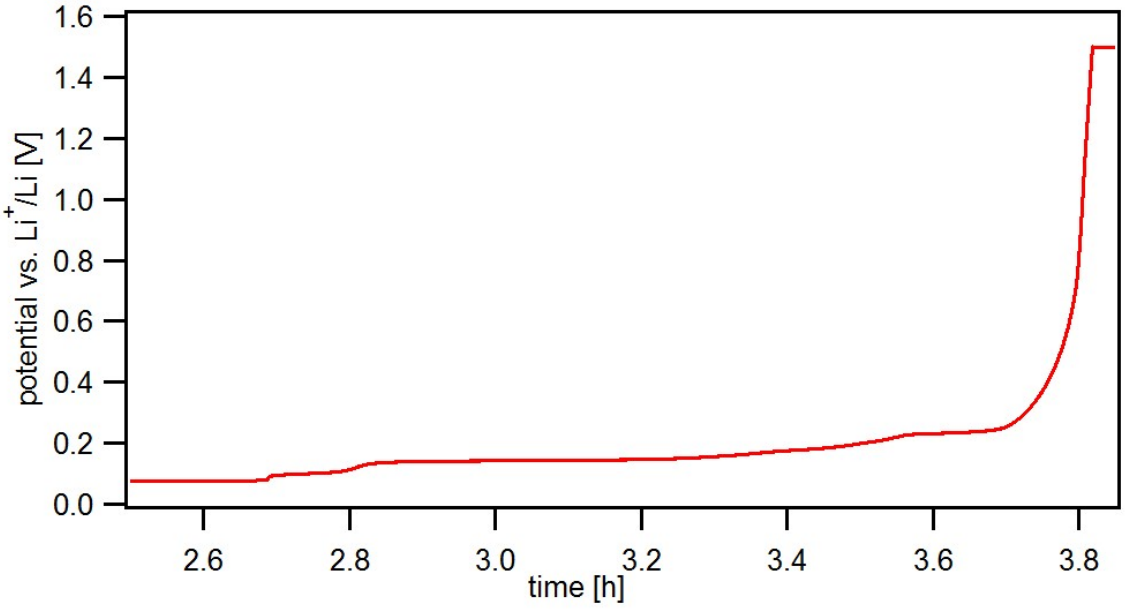


Figure 6.5. – The potential curve for the second discharging of a graphite working electrode with Li as reference and counter electrode, 1 M $LiPF_6$ solution (in EC and DMC) as electrolyte. The current for discharging was 40 µA.

potential indicated a reaction. It was reported that SEI layers started to form around a potential of 0.8 V [137]. Since the SEI layers were formed in the first cycle, the rush decrease of the potential may result from the reconstruction of SEI layers. From 0.2 V on, the potential decreased slowly to the bottom potential limit we programmed. Some steps can be observed, indicating the formation of some staged phases. The second charging lasted 1.95 h.

The second discharging of the cycling in Figure 6.2 is shown in Figure 6.5. Compared with the second charging in Figure 6.4, the steps of the discharging potential profile were weaker. The second discharging lasted for 1.15 h, which demonstrated that the charging process had more charge than the discharging process. This was probably due to the reconstruction of SEI layers.

Since the composition of the intercalant correlates with the capacity for charging and discharging, the differential capacity, $\partial q/\partial V$, shows peaks at the composition where phase transitions occur between coexisting phases[121]. To calculate the differential capacity, current and potential curves were processed with box smoothing using the average value of 1000 corresponding data points to remove the artifacts due to the potentiostat (such as the spikes in Figure 6.3), followed by integrating the smoothed current with time to acquire the charge and calculating the numerical derivative of charge with potential.

The differential capacity for the second charging is shown in Figure 6.6. The determination of the peaks was based on the work of Heß[136] and Dahn[118, 121]. The peaks A, C, D and E corresponded to the phase coexistence (or phase transition) of dilute 1-stage

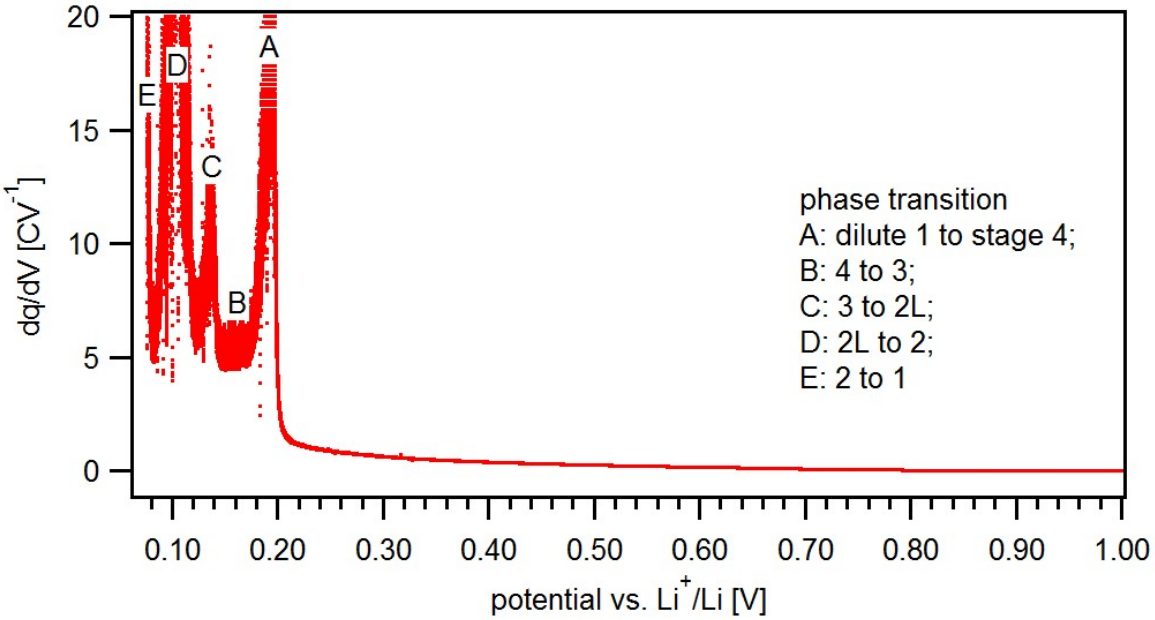


Figure 6.6. – Differential capacity vs. cell potential curves of the second charging of graphite WE. The determination of the peaks was based on the work of Heß[136] and Dahn[118, 121].

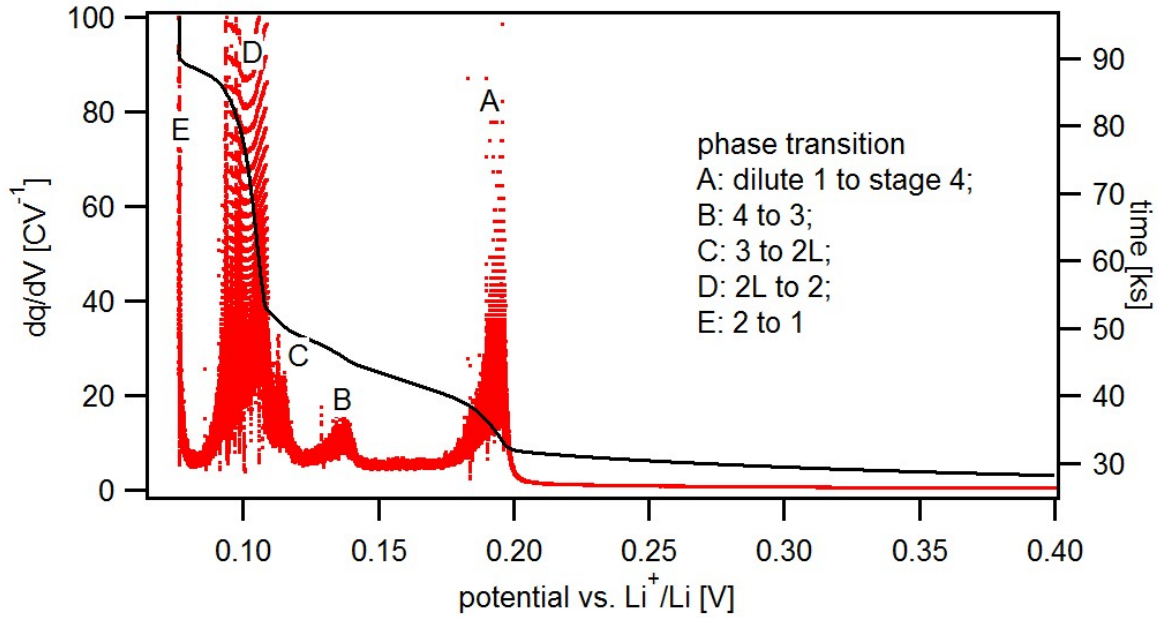


Figure 6.7. – Differential capacity vs. cell potential curves of the second charging of graphite WE.

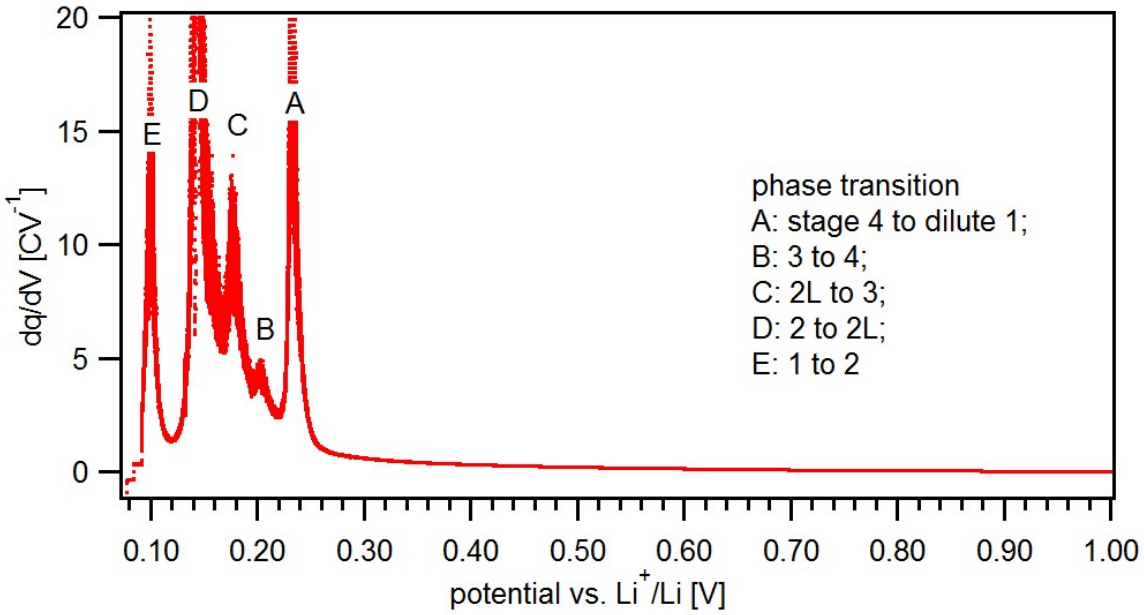


Figure 6.8. – Differential capacity vs. cell potential curves of the second discharging of graphite WE. The determination of the peaks was based on the work of Heß[136] and Dahn[118, 121].

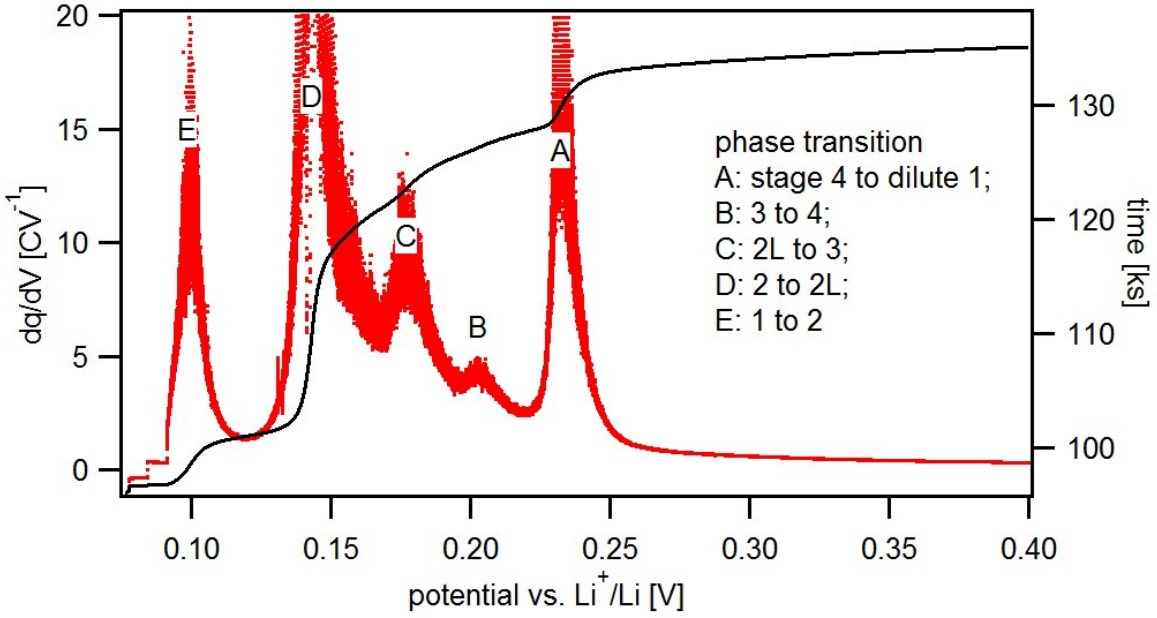


Figure 6.9. – Differential capacity vs. cell potential curves of the second discharging of graphite WE (red). Potential profile shows the potential change with time during the second discharging.

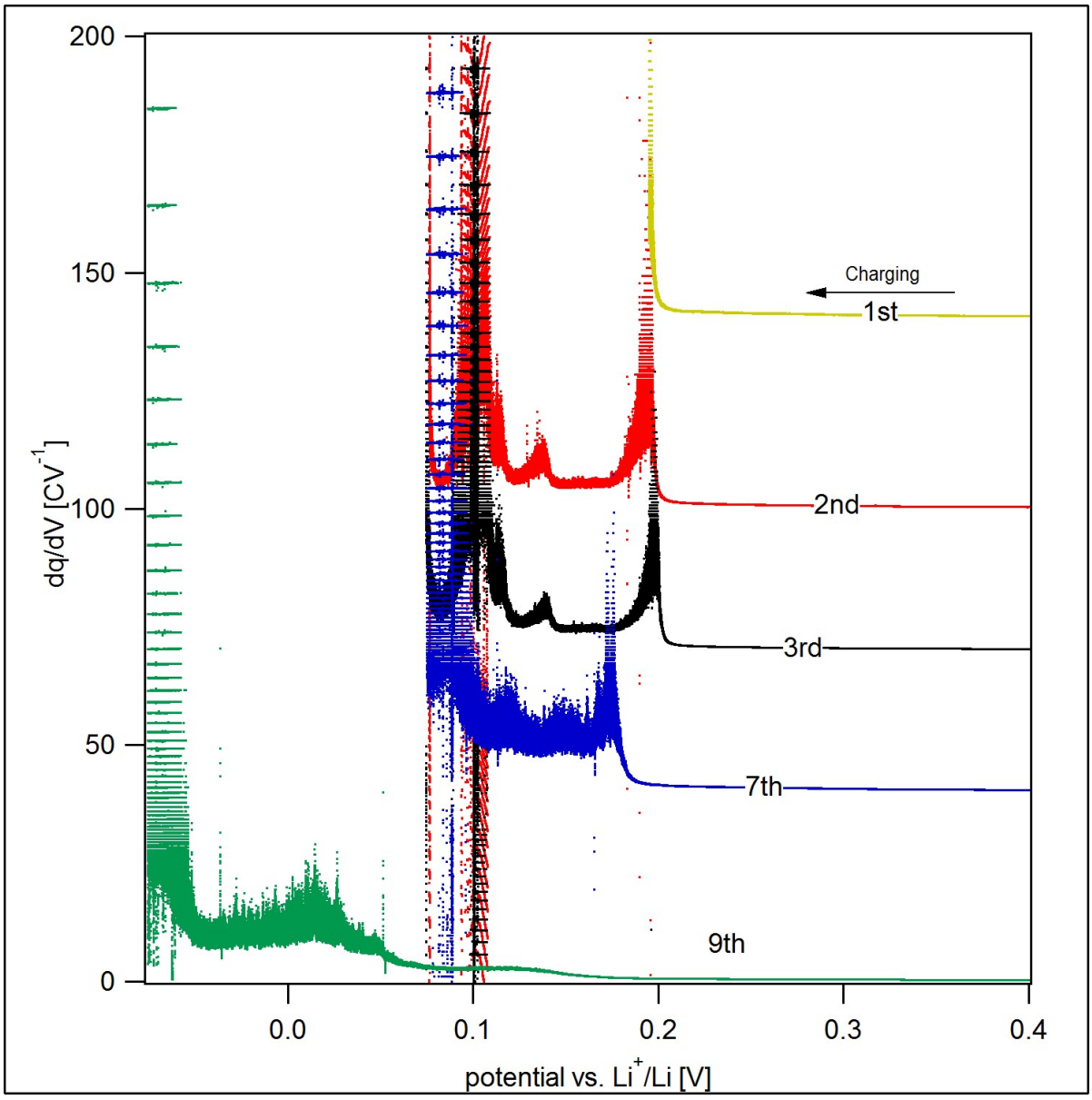


Figure 6.10. – Differential capacity vs. cell potential curves of the charging in different cycles based on Figure 6.2.

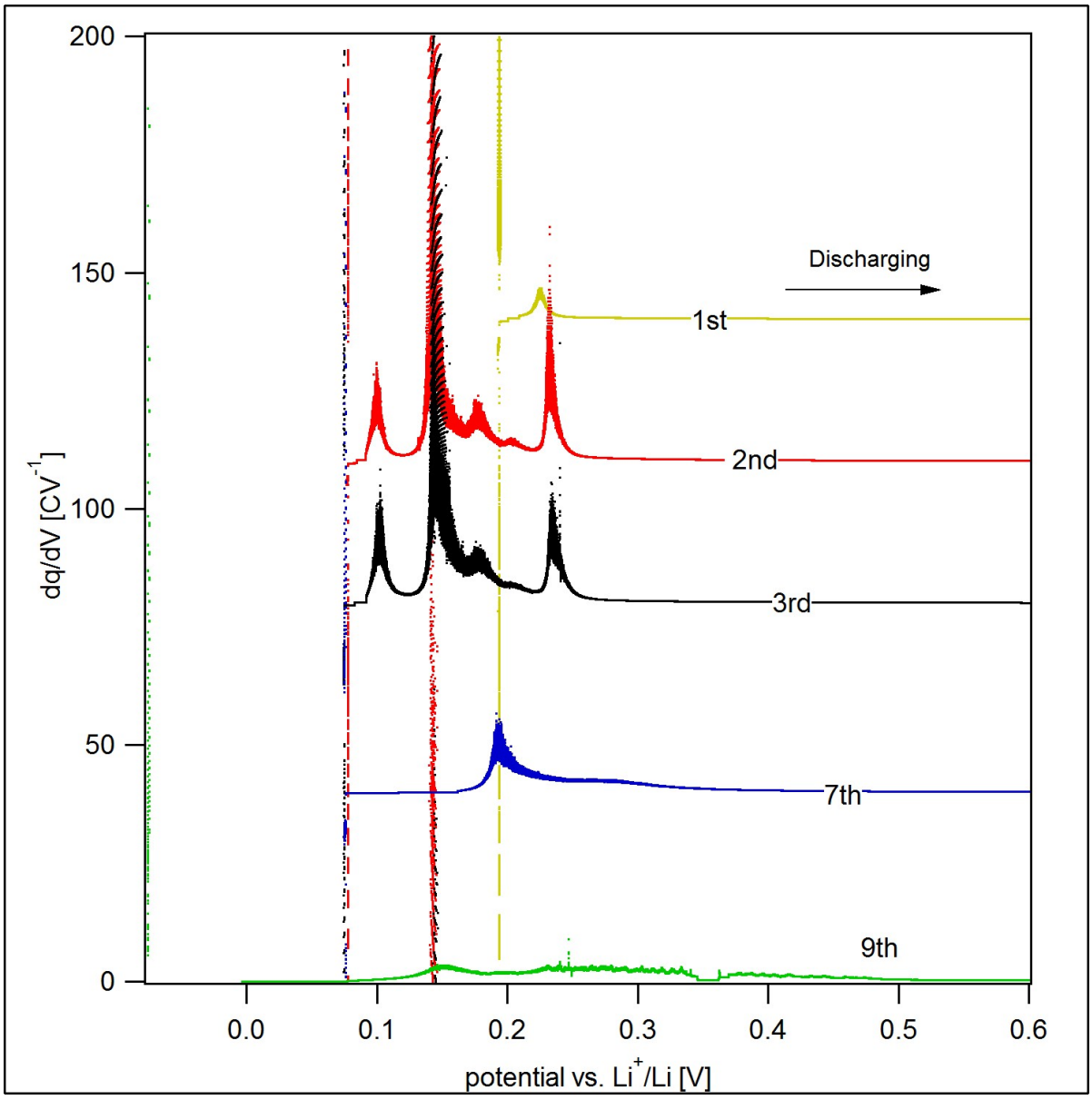


Figure 6.11. – Differential capacity vs. cell potential curves of the discharging in different cycles based on Figure 6.2.

4, stage 3-stage 2L, stage 2L-stage 2 and stage 2-stage 1, respectively. Peak B can be observed with a higher resolution, as shown in Figure 6.7. It may result from the phase transition of stage 4 and stage 3. When the corresponding potential positions of the peaks were compared with the potential profile, the peaks in the curve of differential capacity agreed with the steps in the potential profile.

Figure 6.8 and Figure 6.9 shows the differential capacity for the second discharging. Five peaks were observed, for which the potential positions were more positive than that for charging. Differential capacities of several charging and discharging cycles are shown in Figure 6.10 and Figure 6.11, respectively. The figure demonstrated good reproducibility when the third cycle (including charging and discharging process) was compared with the second cycle. When the graphite electrode was cycled to the seventh cycle, the peaks became weak for charging and disappeared for discharging, with an exception that peak B was still present. During the ninth cycle, no peaks due to phase transition were observed when there was lithium plating.

### 6.2.2. Microcalorimetric measurements at fixed charging states of the graphite WE

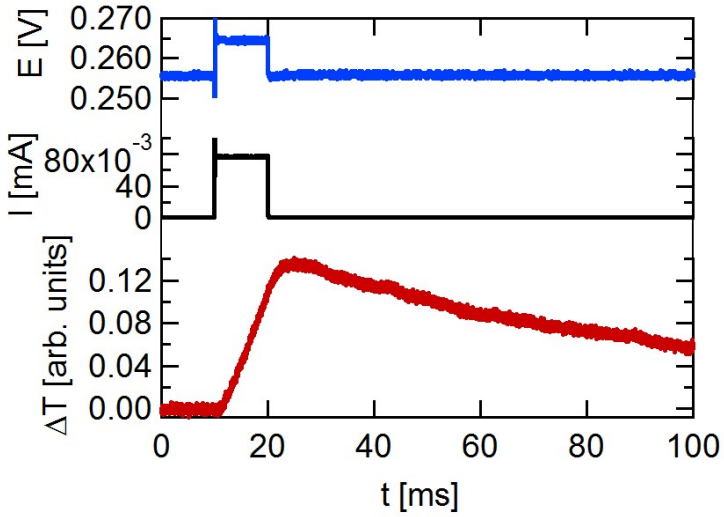


Figure 6.12. – A typical current pulse including transients of potential (top, blue), current (middle, black) and temperature (bottom, red) was applied at about 0.25 V during charging using graphite as working electrode, Li as reference and counter electrode and 1 M $LiPF_6$ solution (in EC and DMC) as electrolyte.

When the graphite electrode was charged or discharged to a certain potential, the cell was switched to OCP and microcalorimetric measurements were conducted by applying current pulses with increasing amplitudes. In Figure 6.12, a typical pulse experiment is shown, including transients of potential (top, blue), current (middle, black) and tempe-

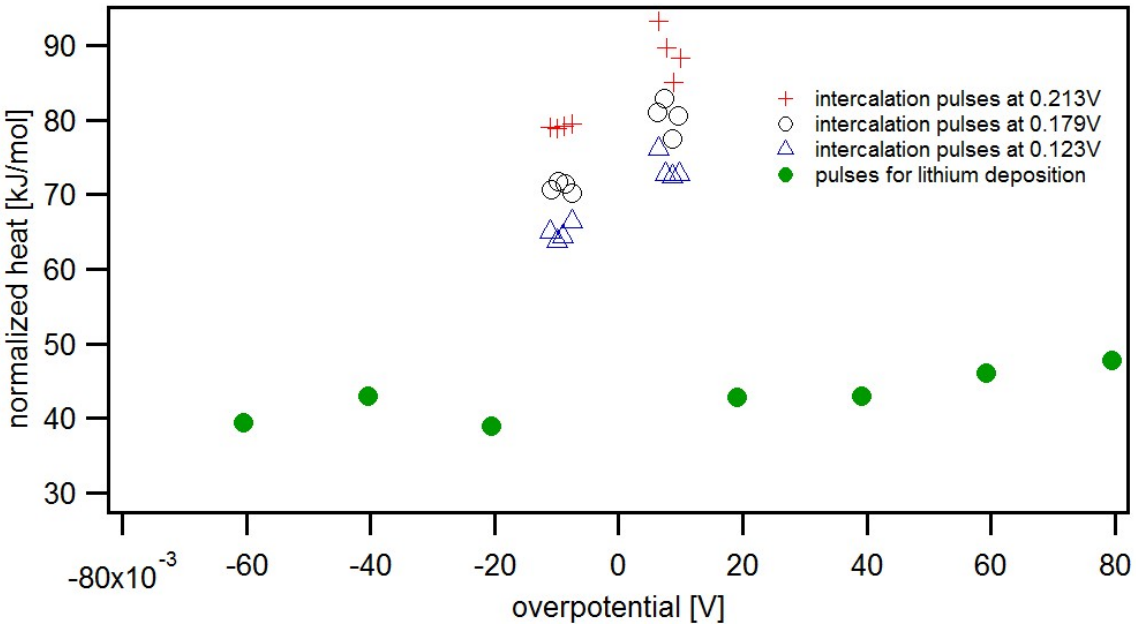


Figure 6.13. – Normalized heat of pulses at different potential during charging calibrated with lithium deposition.

rature (bottom, red) applied at about 0.25 V during charging, using graphite as working electrode, Li as reference and counter electrode and 1 M $LiPF_6$ solution (in EC and DMC) as electrolyte. The spikes at $t = 10\ ms$ of the potential and current transient were due to artifacts from the potentiostat.

Figure 6.13 shows the normalized heat of pulses obtained at different cell potential during charging. As can be seen, the normalized heat of graphite intercalation depends on the open cell potential. As mentioned in section 3.3.1, the microcalorimetric measurements of lithium intercalation were calibrated by lithium deposition. After the graphite was fully charged, ca. 2800 mononlayers of lithium were deposited on graphite. Then pulses were conducted on the lithium surface. The Peltier coefficient, used for calibration was 45 kJ/mol according to chapter 5.

According to Equation (2.19) in chapter 2, the slope of the regression curves in Figure 6.13 can be compared with the Faraday constant. The slope for lithium deposition was 110% of the Faraday constant. However, the slope for lithium intercalation was about 8 times the Faraday constant. The deviation of the slope from Faraday constant may result from charging of the double layer capacitance[52]. In addition, errors from calibration also affect the value of the measured Faraday constant.

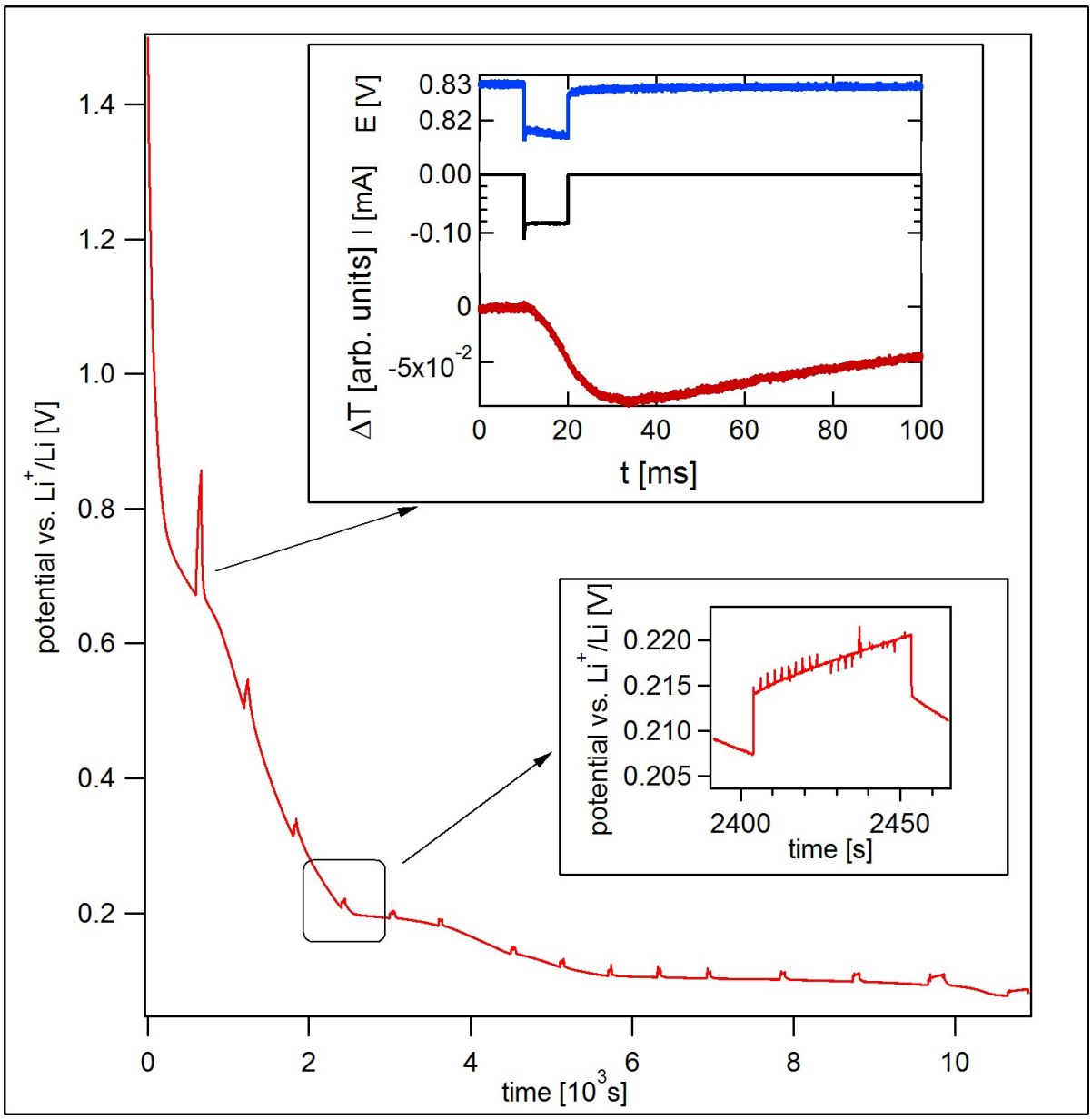


Figure 6.14. – The potential curve for the first charging of a graphite working electrode with graphite as working electrode, Li as reference and counter electrode, 1 M $LiPF_6$ solution (in EC and DMC) as electrolyte (a set of current pulses were applied in between). The current for charging was −40 µA.

### 6.2.3. Microcalorimetric measurements of a graphite electrode during charging and discharging

In this chapter, the microcalorimetric measurements were conducted by applying current pulses during charging and discharging. Different from the experiments in chapter 4 and chapter 5, where potential pulses were applied due to the good control of the cell potential, current pulses were applied here since the current was controlled during charging/discharging while the potential of the cell still relaxed when the cell was switched to OCP.

Before applying current pulses, the open cell potential was about 3.5 V. The cell was charged with a small current to 1.5 V and then charged and discharged automatically, controlled by a procedure based on Igor Pro. The procedure was developed by our group, which allowed us to integrate the microcalorimetric measurement into the galvanostatic measurement of charging and discharging. To record galvanostatic data and microcalorimetric data from charging/discharging simultaneously, two National Instruments Cards were used.

Figure 6.14 shows the potential curve for the first charging of the graphite working electrode with a constant current of 40 µA, during which a set of current pulses were applied. Pulses were applied after the graphite was charged to a certain potential and the cell was switched to OCP by the programmed procedure, as can be seen from the spike at the potential curve in Figure 6.14. When the cell was switched to OCP, the potential of the cell relaxed to its equilibrium potential leading to a spike at the potential curve. The spike at about 0.7 V was due to the relaxation of the potential. An enlarged version of spikes were also shown in Figure 6.14. However, the relaxation had no influence on pulses, as can be seen from the pulse at 0.7 V. The overall change of the potential was similar to that for the cycling, as shown in Figure 6.2. This indicated that the short interruption of the charging and the pulses didn't influence the charging processes.

To further examine the potential change during the pulses, a potential curve during charging at about 0.18 V was enlarged, as shown in Figure 6.15. When the cell was switched to OCP, the potential relaxed by about 0.008 V. The increase of the potential was not significant compared with that of the pulses at 0.7 V, which indicated the intercalation of the graphite. In this measurement, 10 pulses with positive overpotential were applied firstly, followed by applying 10 pulses with negative overpotential. During the pulses, the potential of the cell only relaxed about 0.003 V. After the pulses, the cell was continued to charge until the time limit or the potential limit, where the next series of pulses would be applied.

The current curve for the first charging, interrupted by microcalorimetric measurements with pulses, is shown in Figure 6.16. According to this figure, a current of $-40$ µA was well controlled during charging. Before the pulses, the current returned to zero when

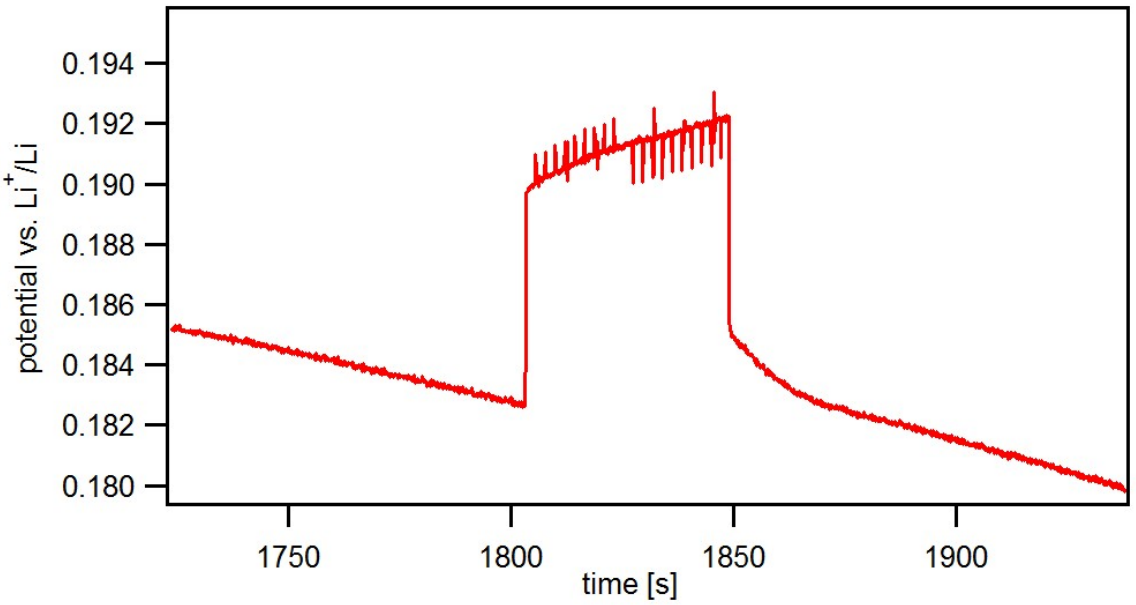


Figure 6.15. – The enlarged potential curve at 0.18 V for the first charging of a graphite working electrode with Li as reference and counter electrode, 1 M $LiPF_6$ solution (in EC and DMC) as electrolyte (the part when a current pulses were applied in between).

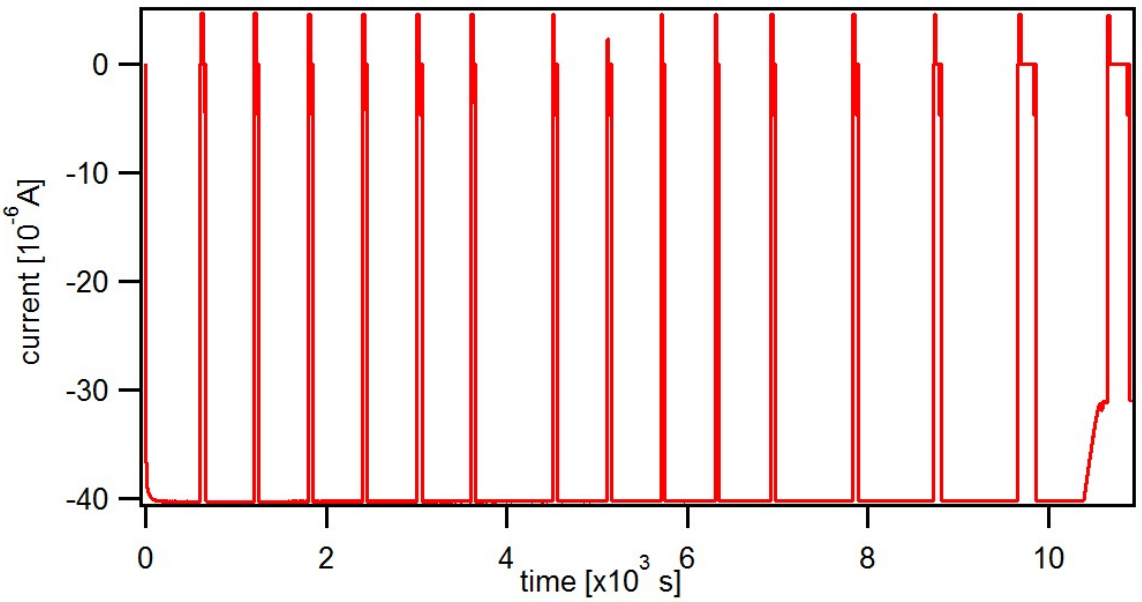


Figure 6.16. – The current curve for the first charging of a graphite working electrode with Li as reference and counter electrode, 1 M $LiPF_6$ solution (in EC and DMC) as electrolyte (a set of current pulses were applied in between).

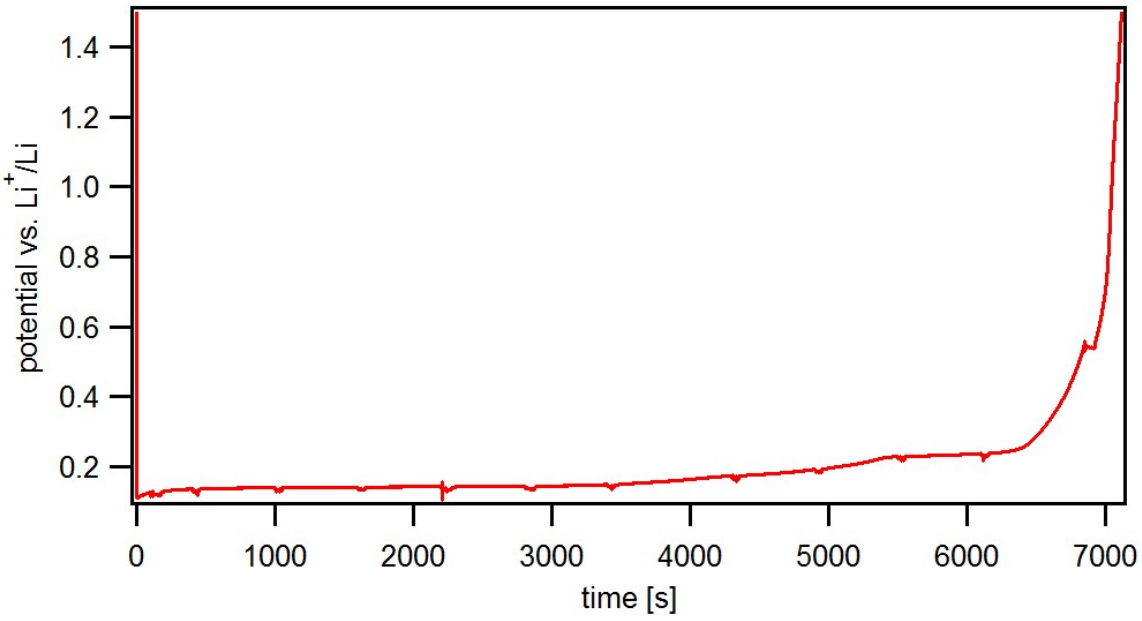


Figure 6.17. – The potential curve for the first discharging of a graphite working electrode with Li as reference and counter electrode, 1 M $LiPF_6$ solution (in EC and DMC) as electrolyte (a set of current pulses were applied in between).

the cell was switched to OCP, controlled by the procedure. When the current pulses for microcalorimetry were applied, the maximum change of current was about 8 µA. After the pulses, the current went back to −40 µA.

Figure 6.17 shows the potential curve with microcalorimetric measurements for the first discharging of a graphite working electrode with lithium as CE, RE and $LiPF_6$ solution (in EC and DMC) as electrolyte. When the cell was switched to OCP for conducting microcalorimetric measurements, the potential decreased by about 0.005 V, as shown in Figure 6.18. This decrease of the potential was comparatively small, which indicated that the deintercalation of the graphite was not completed yet.

The potential dependence of the Peltier coefficient for charging is shown in Figure 6.19. When the potential decreased from 0.23 V to 0.1 V, the normalized heat decreased by about 25 kJ/mol. The change of the Peltier coefficient with the potential was approximately linear, which agreed with that from M. Schmid[23]. An exception was that an inconspicuous slope change was observed between 0.13 V and 0.17 V. From 0.22 V to 0.35 V, a plateau appeared. An extended figure (between 0.1 V and 0.6 V) of the potential dependence of the Peltier coefficient is shown in Figure 6.20. A significant plateau (or a slope) can be observed. The Peltier coefficient decreased by about 35 kJ/mol while the potential decreased from 0.55 V to 0.1 V.

The difference of normalized heat and the corresponding Peltier coefficient between charging (red) and discharging (blue) was explored, as shown in Figure 6.21. The points symbolized the overpotential dependence of the normalized heat and the circles and squa-

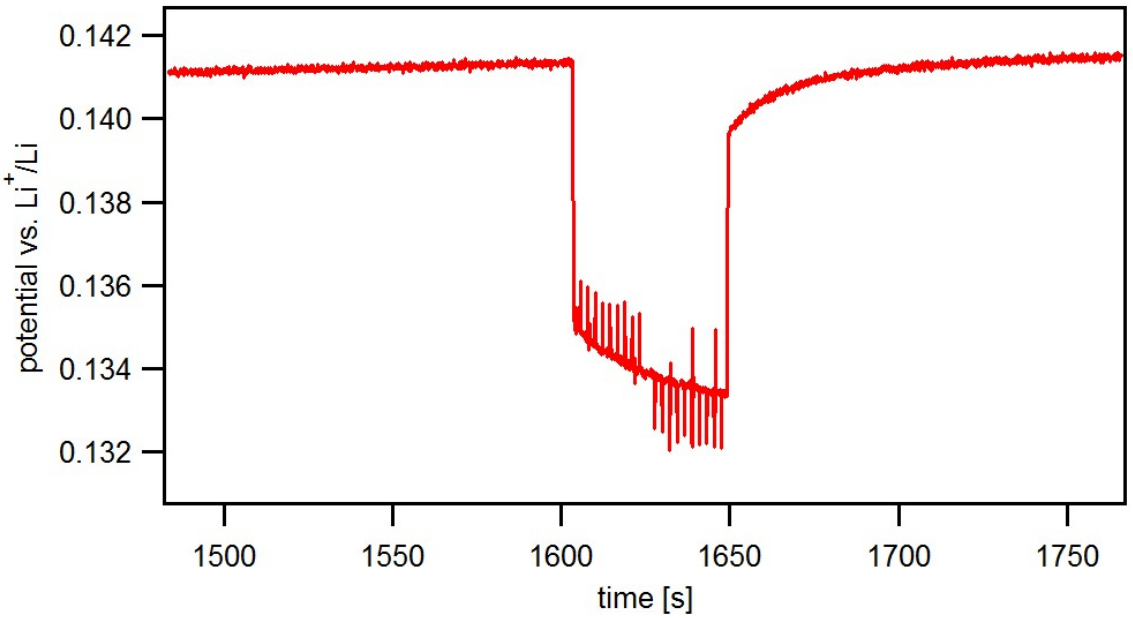


Figure 6.18. – The enlarged potential curve for the first discharging of a graphite working electrode with Li as reference and counter electrode, 1 M $LiPF_6$ solution (in EC and DMC) as electrolyte (the part when a current pulses were applied in between).

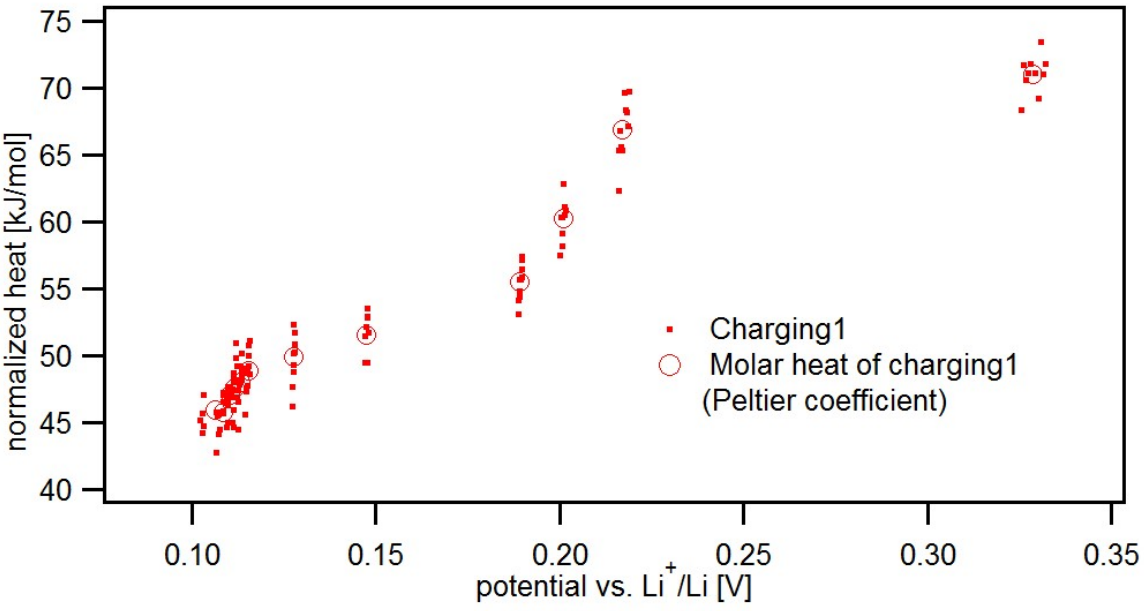


Figure 6.19. – The change of the Peltier coefficient for the charging of graphite versus potential (between 0.1 V and 0.35 V) with graphite as working electrode, Li as reference and counter electrode, 1 M $LiPF_6$ solution (in EC and DMC) as electrolyte. The current for charging was −40 mA.

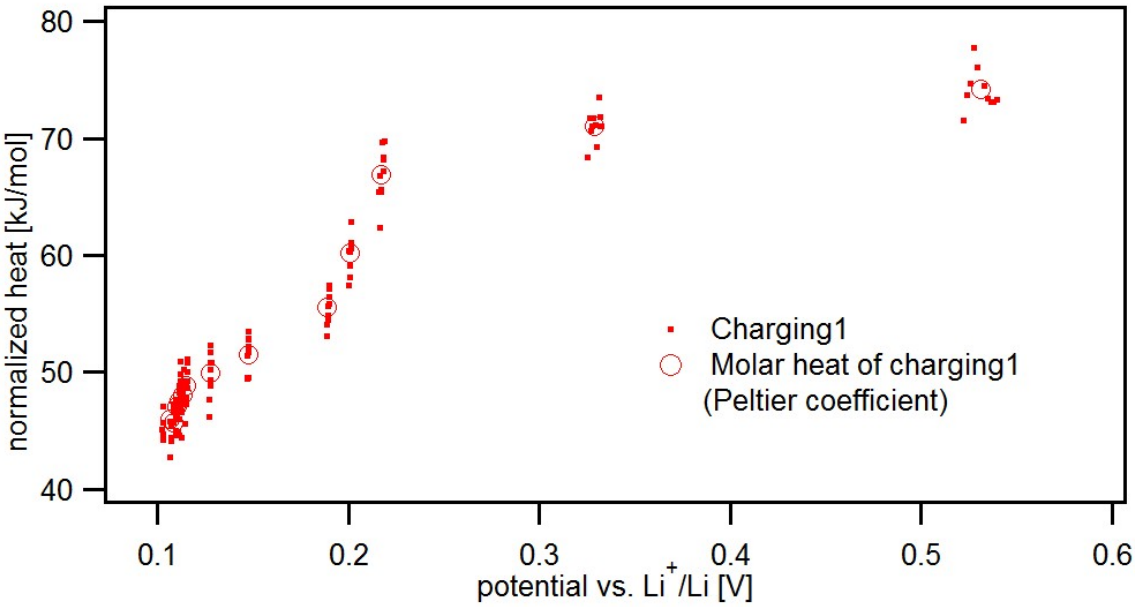


Figure 6.20. – The change of the Peltier coefficient for the charging of graphite versus potential (between 0.1 V and 0.6 V) with graphite as working electrode, Li as reference and counter electrode, 1 M $LiPF_6$ solution (in EC and DMC) as electrolyte.

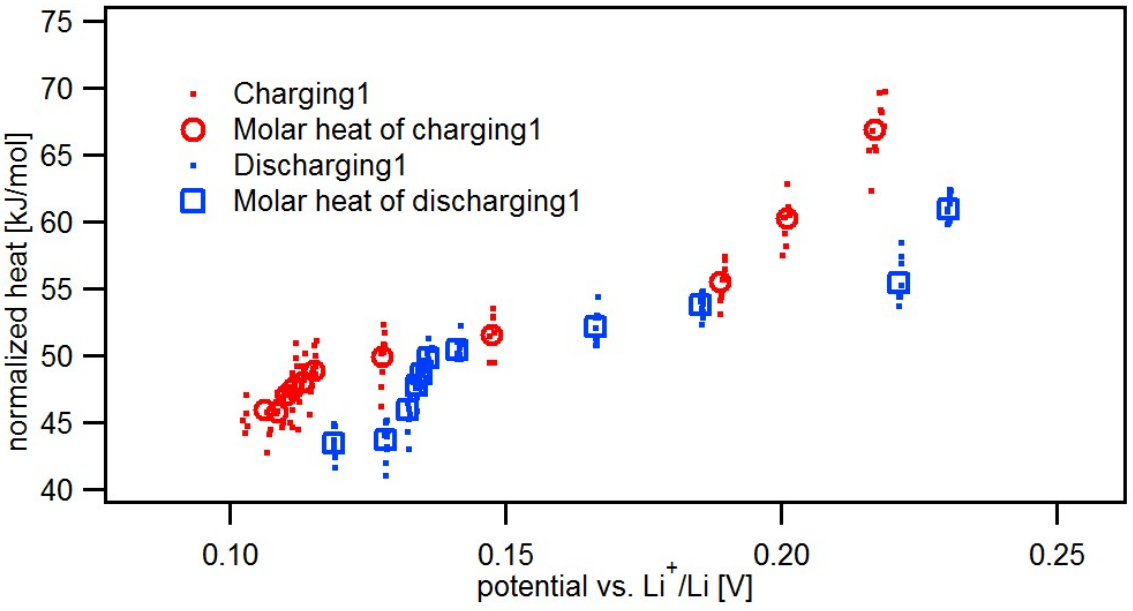


Figure 6.21. – Calibrated heat of the applied pulses during the first charging and discharging of graphite versus potential with graphite as working electrode, Li as reference and counter electrode, 1 M $LiPF_6$ solution (in EC and DMC) as electrolyte.

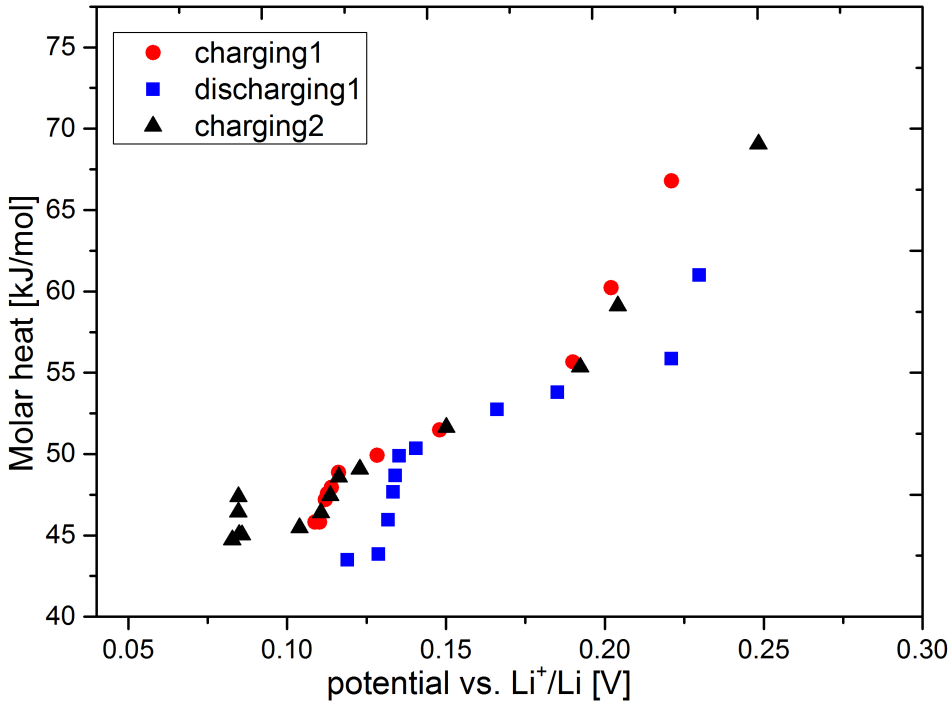


Figure 6.22. – The change of the Peltier coefficient with potential for two charging and one discharging processes of graphite with graphite as working electrode, Li as reference and counter electrode, 1 M $LiPF_6$ solution (in EC and DMC) as electrolyte.

res were the Peltier coefficient obtained by extrapolating the overpotential of the pulses to zero. The Peltier coefficients for the pulses during charging and discharging overlapped from 0.14 V to 0.18 V. The difference was that the change of slope started at different potential. For discharging, the slope changed at about 0.14 V and 0.23 V, i.e., the plateau was between 0.14 V and 0.23 V. But for charging, as shown in Figure 6.19, the potentials where the slope started to change were 0.13 V and 0.20 V.

To testify the reproducibility, the potential dependence of the Peltier coefficient for two charging and one discharging processes of graphite are shown in Figure 6.22. The extent of the Peltier coefficient change was about 25 kJ/mol between 0.08 V and 0.25 V for both charging and discharging, which agreed with that in Figure 6.19. It demonstrated good reproducibility for the first and the second charging. Both the first charging and the second charging had a plateau between 0.13 V and 0.20 V. In the second cycle, the charging was conducted till 0.08 V, where a peak of the the Peltier coefficient $\Pi$ was observed at about 0.09 V. Figure 6.23 exhibited the potential dependence of the Peltier coefficient for two charging and one discharging processes of graphite in the long potential range (between

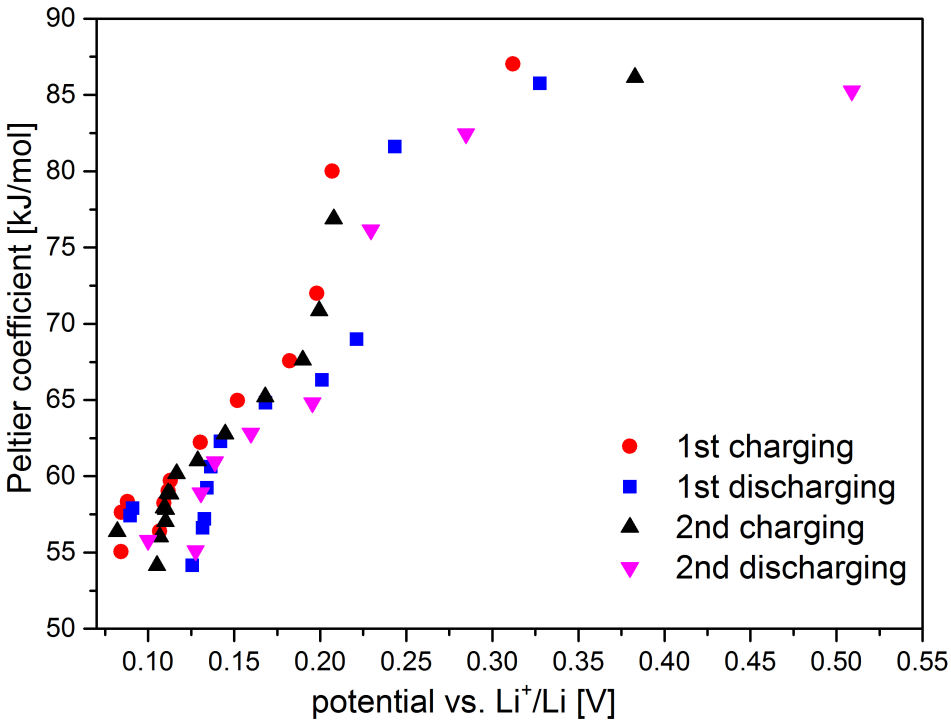


Figure 6.23. – The change of the Peltier coefficient for two charging and one discharging processes of graphite in the long potential range using graphite as working electrode, Li as reference and counter electrode, 1 M $LiPF_6$ solution (in EC and DMC) as electrolyte. The current was ±40 µA.

0.08 V and 0.55 V). The Peltier coefficient was almost constant between 0.25 V and 0.55 V. From 0.25 V to 0.08 V, the Peltier coefficient decreased about 30 kJ/mol.

More information about the change of the Peltier coefficient could be obtained between 0.08 V and 0.15 V, if more data points were applied in this range. The enlarged version for Figure 6.23 is shown in Figure 6.24. The peak at about 0.09 V also appeared in the second charging with an amplitude of 5 kJ/mol. It demonstrated good reproducibility for the first and the second charging. In the discharging process, it's expected that there was also a peak at about 0.1 V. The potential, where the slope of the Peltier coefficient curve changed or the peaks appeared, agreed with the trends of the potential curves for charging and discharging in Figure 6.14 and Figure 6.17.

With an improved procedure and setup, more current pulses were applied every 2 or 3 minutes during charging and discharging. Figure 6.25 shows the potential curve for the first charging of the graphite working electrode with current pulses (using a current of −50 µA). The spike at about 0.7 V was mainly due to the relaxation of potential when the cell was switched to OCP for about 200 s. The corresponding potential dependence of the Peltier coefficients for the pulses is shown in Figure 6.26. It demonstrated a good

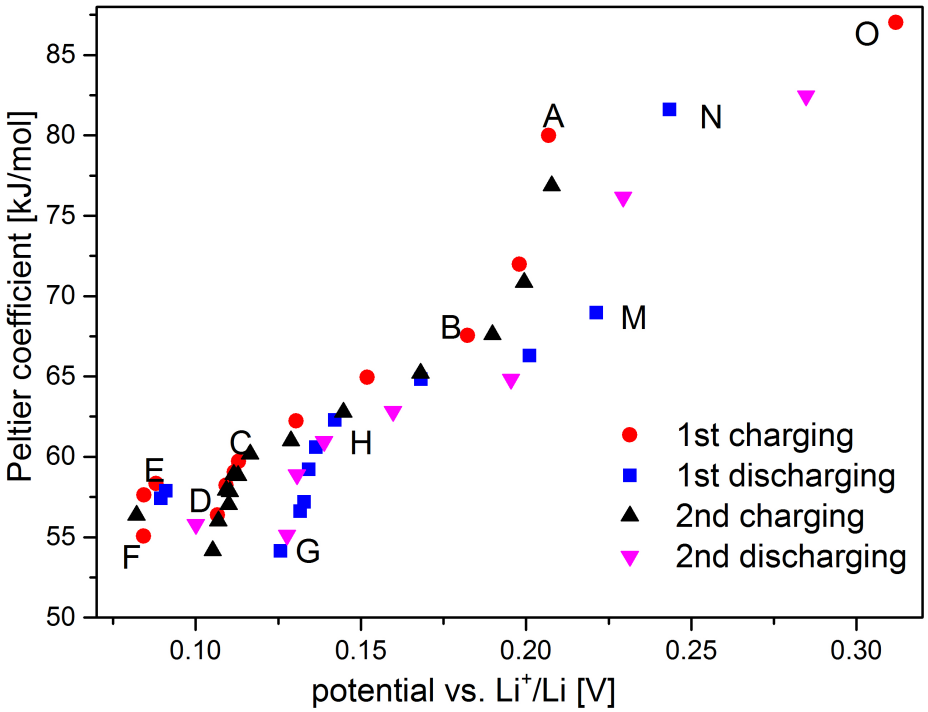


Figure 6.24. – The change of the Peltier coefficient with potential for two charging and one discharging processes of graphite in the short potential range using graphite as working electrode, Li as reference and counter electrode, 1 M $LiPF_6$ solution (in EC and DMC) as electrolyte. The current was ±40 µA.

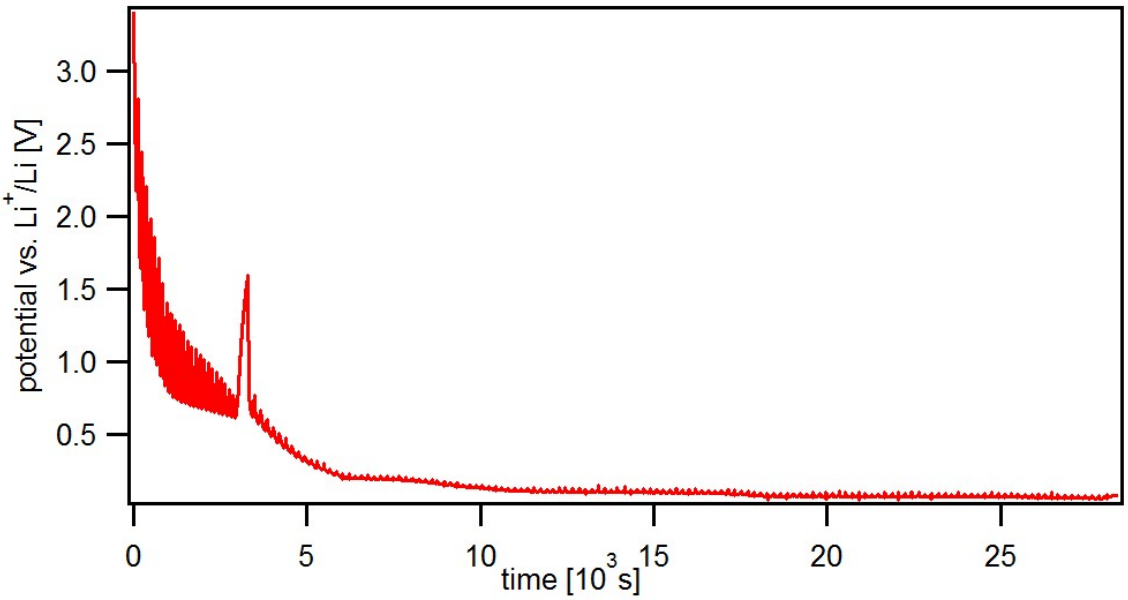


Figure 6.25. – The potential curve for the first charging of a graphite working electrode with current pulses applied in every 2 or 3 minutes.

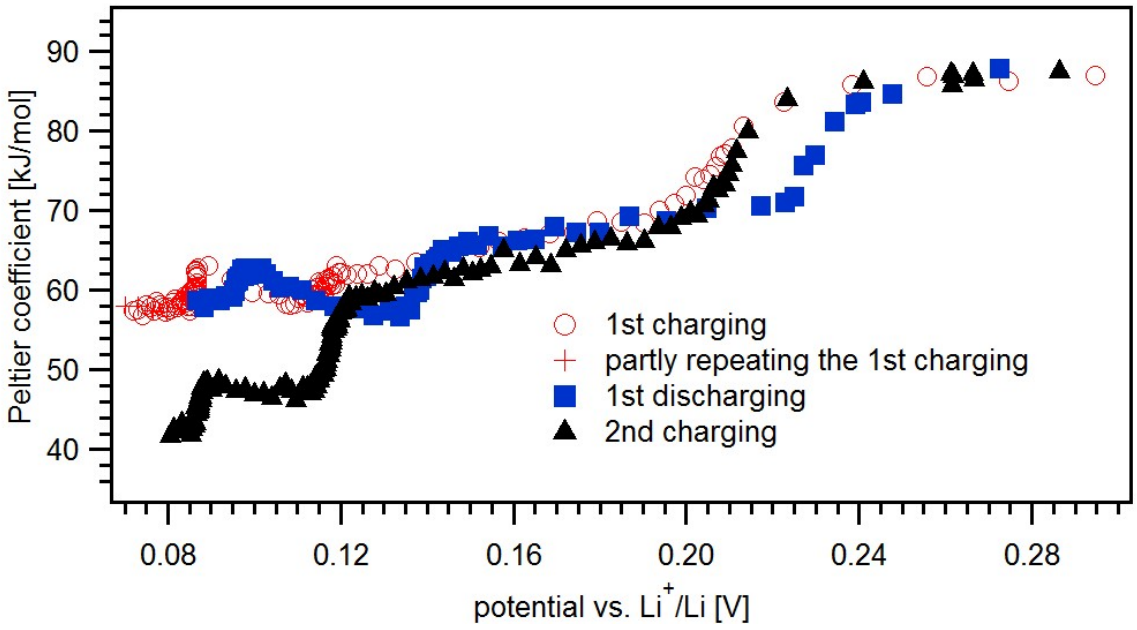


Figure 6.26. – The change of the Peltier coefficient with potential for two charging and one discharging processes of graphite with current pulses applied in every 2 or 3 minutes (Li as reference and counter electrode, 1 M $LiPF_6$ solution in EC and DMC as electrolyte).

reversibility between the first charging and discharging at potential above 0.12 V. There was significant deviation for the second charging between 0.08 V and 0.13 V, which resulted from the aging effect of the graphite working electrode and the exfoliation of the graphite from the copper foil, as found after dismantling the cell.

### 6.2.4. The decomposition of the electrolyte and formation of the SEI layers

It was reported that the decomposition of electrolyte and the formation of a solid electrolyte interphase layer (SEI layer) occurred around 0.8 V [137]. To show the change of the Peltier coefficient during the formation of SEI, we performed microcalorimetric measurements for charging and discharging between between 0.05 V and 2.75 V under a current of −40 µA for charging and 40 µA for discharging, respectively, as shown in Figure 6.27. The points symbolize the normalized heat of the pulses, while the filled circles, triangles and squares denote the corresponding Peltier coefficient for each set of the pulses. The Peltier coefficient for the pulses applied during the first charging between 1.75 V and 2.75 V was almost constant with a value of 10 kJ/mol. A typical pulse including transients of potential (top, blue), current (middle, black) and temperature (bottom, red) applied at about 2.7 V is shown in Figure 6.28. For this current pulse, a current difference of −70 µA was applied leading to an overpotential of −8 mV and a heat flow of -0.015 in arbitrary units.

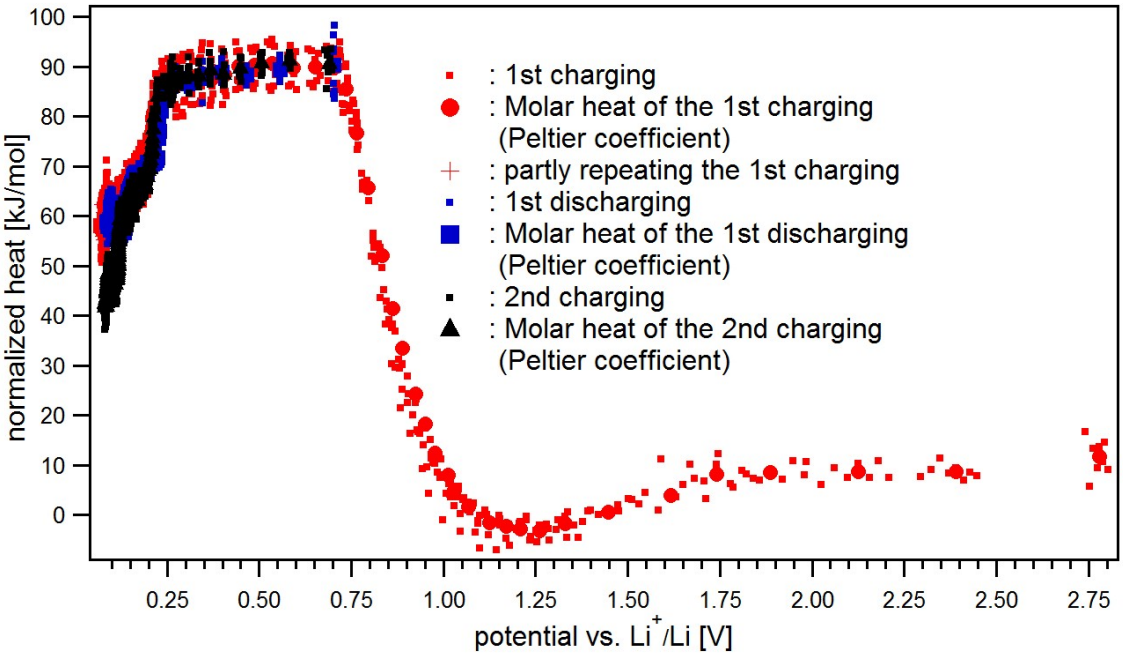


Figure 6.27. – The change of the Peltier coefficient with potential for two charging and one discharging processes of graphite with current pulses applied in every 2 or 3 minutes (Li as reference and counter electrode, 1 M $LiPF_6$ solution in EC and DMC as electrolyte).

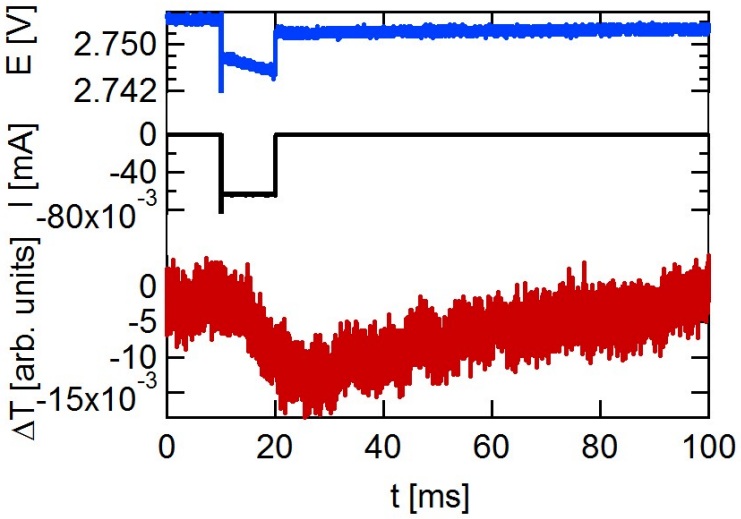


Figure 6.28. – A typical current pulse including transients of potential (top, blue), current (middle, black) and temperature (bottom, red) was applied at about 2.7 V during charging using graphite as working electrode, Li as reference and counter electrode and 1 M $LiPF_6$ solution (in EC and DMC) as electrolyte.

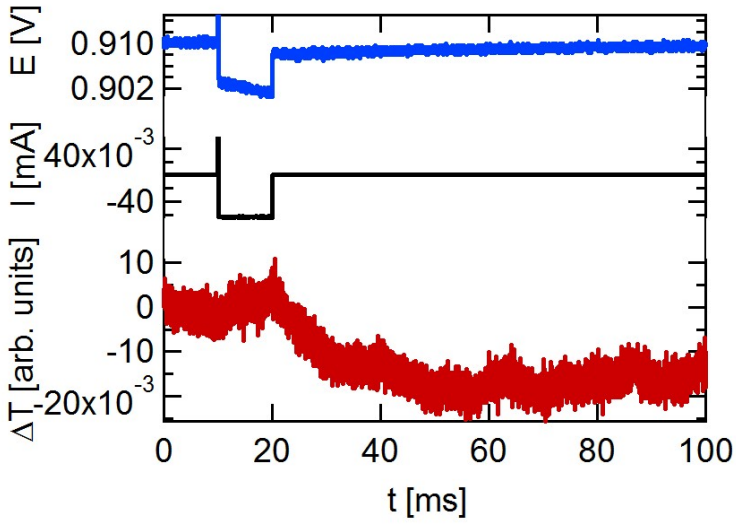


Figure 6.29. – A typical current pulse including transients of potential (top, blue), current (middle, black) and temperature (bottom, red) was applied at about 0.9 V during charging using graphite as working electrode, Li as reference and counter electrode and 1 M $LiPF_6$ solution (in EC and DMC) as electrolyte.

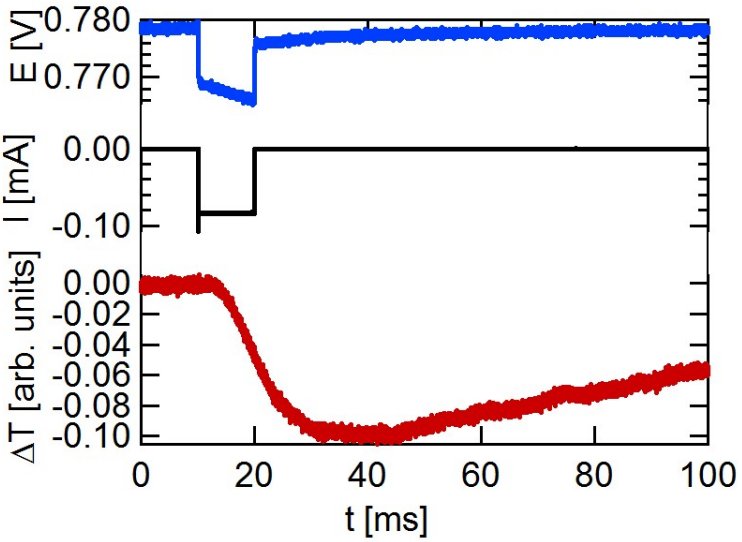


Figure 6.30. – A typical current pulse including transients of potential (top, blue), current (middle, black) and temperature (bottom, red) was applied at about 0.8 V during charging using graphite as working electrode, Li as reference and counter electrode and 1 M $LiPF_6$ solution (in EC and DMC) as electrolyte.

Only small delayed heat evolution was found, as shown from the temperature transient in Figure 6.28.

As the potential decreased, the Peltier coefficient started to decrease and reached its minimum (0 kJ/mol) at about 0.9 V. A typical pulse including transients of potential (top, blue), current (middle, black) and temperature (bottom, red) applied at about 0.9 V, is shown in Figure 6.29. For this current pulse, a current difference of −40 µA was applied leading to an overpotential of about −8 mV and a heat flow of -0.020 in arbitrary units. Compared with the current pulse at 2.75 V, the current transient possessed smaller current. The temperature transient in Figure 6.29 reached its minimum at about $t = 60\ ms$ and showed significant delayed heat evolution when the overpotential was stopped at $t = 20\ ms$.

As the charging went on, the Peltier coefficient started to increase until a potential of 0.75 V, where the Peltier coefficient reached the maximum. Figure 6.30 shows a typical pulse including transients of potential (top, blue), current (middle, black) and temperature (bottom, red) applied at about 0.8 V during charging. For this current pulse, a current difference of −100 µA was applied leading to an overpotential about −10 mV and a heat flow of -0.1 in arbitrary units. With a similar amplitude of the overpotential, the amplitude of the current transient at 0.8 V was −100 µA and the delayed heat evolution, as shown from the temperature transient, was smaller.

## 6.3. Discussion

### 6.3.1. Potential dependence of reaction entropy

Measurements of molar entropy change $\Delta_R S$, based on the temperature response of the open circuit potention $E$, show that the contribution of enthalpy can be neglected. Therefore, the reaction entropy changed linearly with the zero-current cell potential according to Equation (2.12). As mentioned in chapter 2, the entropy consists two parts: the reaction entropy and the transport entropy. However, the transport entropy can be neglected according to the discussion in subsection 5.3.2. Therefore, the reaction entropy can be calculated according to the Peltier coefficient. Figure 6.24 shows the change of the Peltier coefficient with potential for two charging and two discharging processes of graphite in the short potential range. The red circles and the black triangles denote the change of the Peltier coefficient with potential for the charging process of the first and the second cycles, respectively. The blue squares and the pink triangles symbolize the change of the Peltier coefficient with potential for the discharging process of the first and the second cycles, respectively. In the range of OF in Figure 6.24, the Peltier coefficient decreased on the average about linearly with the potential, ignoring the variations due to the phase transitions between the intercalation stages. The slope of the curve of the

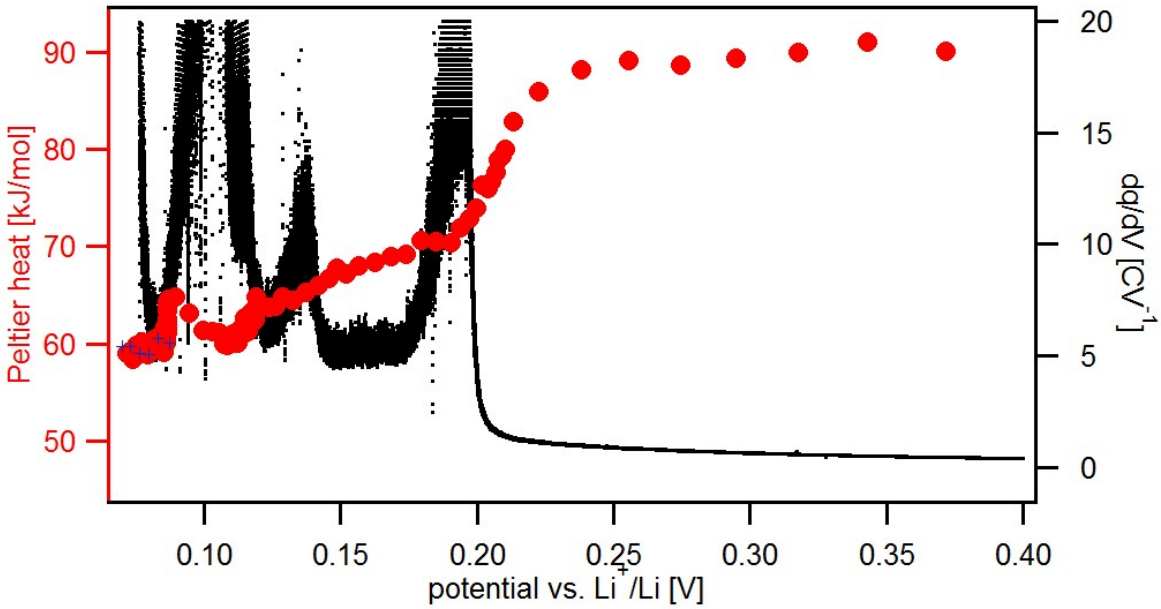


Figure 6.31. – The potential dependence of differential capacity and the Peltier coefficient during charging. The data of the differential capacity during charging is from Figure 6.6. The data of the Peltier coefficient during charging is shown in Figure 6.26.

Table 6.1. – The Peltier coefficient of phase transition in graphite working electrodes, obtained by microcalorimeter measurement using 1 M $LiPF_6$ as the electrolyte and lithium as RE and CE. The regions were denoted according to Figure 6.24

| **1st Charging** | | | **1st Discharging** | | |
|---|---|---|---|---|---|
| region | phase transition | change of Peltier coefficient (kJ/mol) | region | composition change | change of Peltier coefficient (kJ/mol) |
| AB | 1' to 4 | -15 | MN | 4 to 1' | 15 |
| CD | 2L to 2 | -5 | GH | 2 to 2L | 10 |
| EF | 2 to 1 | -5 | FE | 1 to 2 | 5 |

Peltier coefficient ($\Pi = T \cdot \Delta\Delta_R S$) vs potential is about 118% of the Faraday constant. In other measurement, 114% was found[23]. That is $F \approx \frac{T \cdot \Delta\Delta_R S}{\Delta E}$. Since the charge number of ion $z = 1$, the relation between the potential and the variation of reaction entropy agrees with Equation (2.12) and the contribution of enthalpy change with potential is small.

## 6.3.2. Entropy change during phase transition

The potential dependence of the Peltier coefficient for charging and discharging is compared with the corresponding differential capacity $\partial q/\partial V$, as shown in Figure 6.31 and

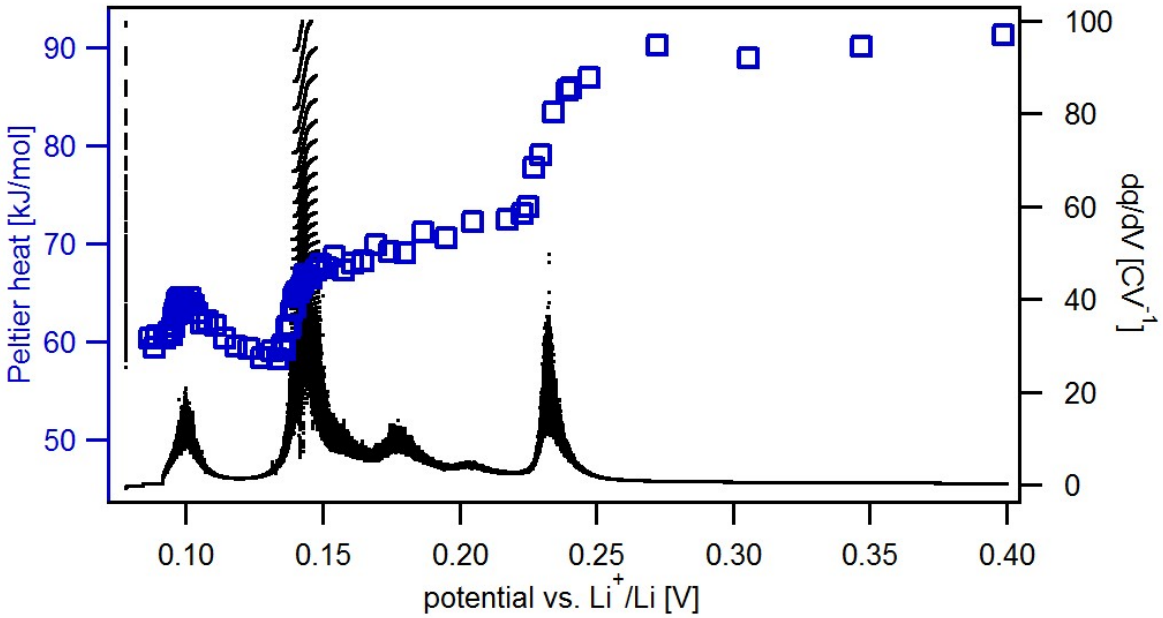


Figure 6.32. – The potential dependence of differential capacity and the Peltier coefficient during discharging. The data of the differential capacity during discharging is from Figure 6.8. The data of the Peltier coefficient during discharging is shown in Figure 6.26.

Figure 6.32. The steps in the plots of Peltier coefficient vs. potential and the peaks at the differential capacity curve appear at almost the same potential. Steps corresponding to some phase transitions in Figure 6.6 and Figure 6.8, such as the phase transition from stage 3 to stage 2L, are not observed at the curve of the potential dependence of the Peltier coefficient. According to section 2.1, at the step region, where the cell potential don't change significantly during charging and discharging, the change of the free enthalpy is zero ($\Delta\Delta_R G = 0$, see Equation (2.7)). Hence the variations of the Peltier coefficient $\Pi$ at the steps result from the phase transition of staged phases in the graphite electrodes, which is also confirmed by the differential capacity curve, as can be seen in Figure 6.6 and Figure 6.8. The change of the Peltier coefficient (or molar heat) and corresponding entropy change for phase transition are listed in Table 6.1. The negative sign means that the Peltier coefficient decreases and vice versa.

### 6.3.3. Comparison with other studies of reaction entropy of lithium intercalation

Several studies about the heat effect of lithium intercalation in graphite have been published. They are summarized in Figure 6.33 to compare with the result from this chapter.

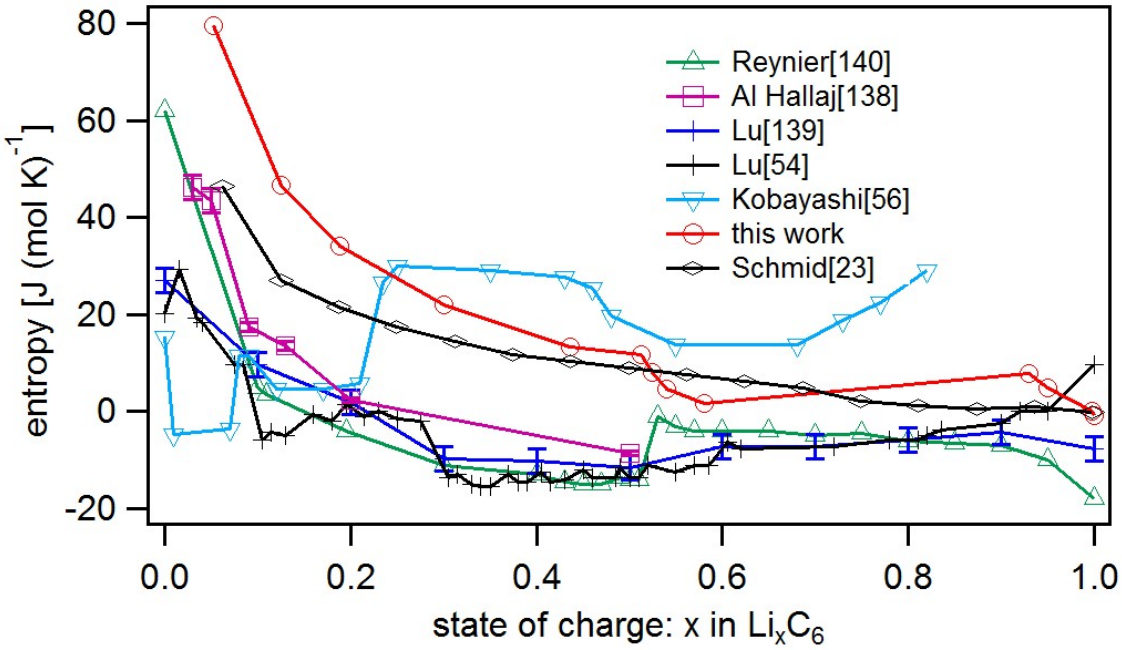


Figure 6.33. – The literature review of the reaction entropy of lithium intercalation in graphite. The reaction entropy in this work was calculated according to the Peltier coefficient of the first charging in Figure 6.22. The reaction entropy from References [23, 54, 56, 138–140] were translated in $J/(mol \cdot K)$ and plotted versus state of charge of graphite electrode according to Reference [23]. State of charge $x$ describes the percent of occupation compared with the available lithium hosts in graphite. Hence, $x$ is between 0 and 1.

Using accelerating rate calorimeter, Hallaj *et al.*[138] studied a commercial button battery with lithium and mesocarbon microbeads (MCMB)-graphite as electrodes. The reaction entropy varied from 43 J/(mol K) to −7 J/(mol K), when the state of charge changed from 0.05 to 0.5. A sharp decrease at about $x = 0.1$ may result from the ordering process of 4L phase. By conducting calorimetric measurements, Lu investigated an Li/MCMB-graphite button cell[139]. Through measuring of the temperature dependence of open cell voltage, they obtained a reaction entropy change between 27 J/(mol K) and −9.6 J/(mol K) for lithium intercalation in graphite. The positive entropy at the beginning leads to an ordering/disordering transition and a structure change of the stacked graphite layers from $AB$ to $AA$[139].

Lithium deposition in different types of graphites[20, 140, 141] were investigated by Reynier *et al.* An entropy change of about 62 J/(mol K) between $x = 0$ (state of charge) and $x = 0.2$ was obtained by measuring temperature dependence of open cell voltage. They interpreted the decrease of entropy at the beginning of charging by considering the configuration entropy. Then a negative reaction entropy from −4 J/(mol K) to −12 J/(mol K) was observed. An sharp increase of entropy was found at about $x = 0.5$.

With a method of isothermal Calvet Type Heat Flow Microcalorimeter, Kobayashi *et al.* measured the heat effect of Li-ion batteries using a Li/graphite electrode (or graphite-$LiCoO_2$) during charging and discharging[56]. Both warming and cooling effect were observed because of the different heat effect (endothermal and exothermal) for different phase transition. Maeda studied the intercalation of $Li^+$, $K^+$ and $BF_4^-$ ions in graphite[57]. Their results showed a warming effect for lithium intercalation in graphite probably due to a greater contribution from the irreversible heat. Since a high current of 17 $mA/cm^2$ was used, the Joule heat may over compensate the reversible heat.

In comparison with the results from literature, our result is close to that from literature. There was a abrupt decrease of reaction entropy until $x = 0.2$. Similar trend was found from the literature results. Around $x = 0.5$, the reaction entropy decreased about 10 J/(mol K) and then increased slightly before deceasing again. When the state of charge was high, the reaction entropy was close to the reaction entropy of lithium bulk deposition.

### 6.3.4. Interpretation of the reaction entropy of lithium intercalation in graphite based on lattice-gas model

The following discussion was based the work of Reynier *et al.* [20, 140] and Schmid[23]. Using a lattice-gas model, the contributions of configuration entropy and vibration entropy to the reaction entropy were considered.

A study demonstrates that the change of vibrational entropy between two solid phases contributes to the entropy of solid-solid phase transitions[142]. It depends on the Debye temperature of the phonon spectra, which consists of two parts: $\theta_{D\perp}$ and $\theta_{D\parallel}$ for motion perpendicular (the first term in Equation (6.1)) and parallel to the graphite sheets. Therefore, the vibrational entropy, which is responsible for the phase transition between staged 2 and staged 1, can be denoted by the following equation with $\theta_{D0}$ as the Debye temperature for lithium metal (bcc)[140]:

$$\Delta S_{2\to 1} \approx \Delta S_{vib} = k_B \cdot ln\left(\frac{\theta_{D0}}{\theta_{D\perp}}\right) + 2 \cdot k_B \cdot ln\left(\frac{\theta_{D0}}{\theta_{D\parallel}}\right) \tag{6.1}$$

For both $LiC_6$ and $LiC_{12}$, Reynier used $\theta_{D\parallel} = 392\ K$ and $\theta_{D\perp} = 893\ K$ according to the calculations in the literature[140]. For lithium metal with a body-centered cubic (bcc) structure, an experimental temperature of $\theta_{D0} = 380\ K$ was used. It is assumed that the carbon phonon modes aren't significantly affected by the intercalation of lithium. Using these parameters, a vibration entropy of about $-7.6$ J/(mol K) for phase transition between staged 2 and staged 1 is obtained. Through calculation, we know that the first term of Equation (6.1) has a much larger contribution to the vibration entropy in comparison with the second term. The negative sign of vibration entropy indicates

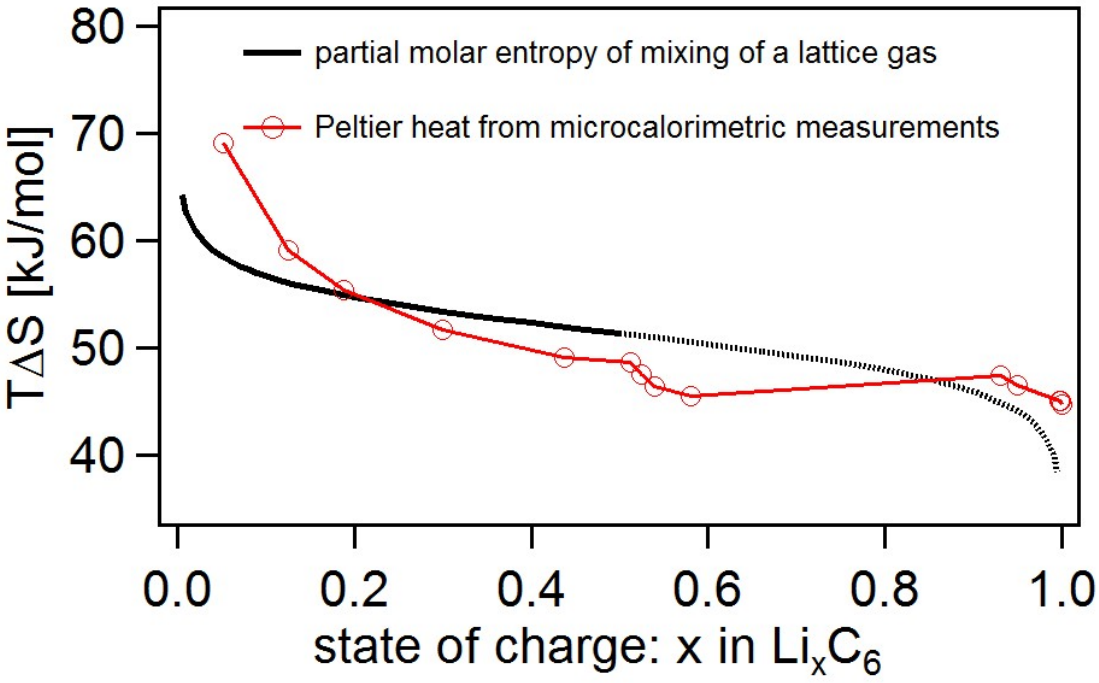


Figure 6.34. – The Peltier coefficient of lithium intercalation in graphite from the second charging in Figure 6.22 and the calculated Peltier coefficient according to partial configuration entropy.

that the vibration entropy functions as a restriction to the movement of lithium atom perpendicular to the lattice layers. The vibration entropy of electrons can be neglected[23].

In the lattice-gas model, the interlayers of the graphite sheets were treated as 2D lattices. The lithium atoms between lattices are regarded as the lattice gas. Therefore, the entropy of mixing, also called the configuration entropy in this case, is dependent of the state of charge $x$:

$$S_{config}(x) = -k_B[x \cdot ln(x) + (1-x) \cdot ln(1-x)] \tag{6.2}$$

Instead of the calculation of absolute configuration entropy, the partial configuration entropy was calculated in this work according to the following equation[47, 140]:

$$\frac{dS_{config}}{dx} = -k_B \cdot ln\left(\frac{1-x}{x}\right) \tag{6.3}$$

The reaction entropy of lithium intercalation is close to that from the calculation based on lattice-gas model, as can be seen in Figure 6.34. As shown in Figure 6.34, there is a deviation between the measured and the calculated Peltier coefficient, where the state of charge is small than 0.2 ($x < 0.2$) and close to 0.5 ($x \approx 0.5$). As $x$ is larger than 0.5, the phase transition from staged phase 2 to 1 occurr[136]. Since the staged phase 1 and 2 are highly ordered phases, the calculation of configuration entropy based on a statistical distribution of atoms at a lattice is not applicable. The experimental

Peltier coefficient decreases with the increase of state of charge, when $x$ is larger than 0.5. Here, the state of charge $x$ is calculated from the charge. In detail, the charge at the potential where pulses are applied, are divided by the overall charge during charging. The relation between the charge state $x$ and corresponding potential agree with the results in literature[136, 143, 144].

Reynier[140] argued that the lattice-gas model was feasible only when there was random lithium intercalation in graphite electrode and no ordered phase started to formed. They introduced a solubility limit of the disordered phase $x_0$ to modify Equation (6.4), so they obtained:

$$\frac{dS_{config}}{dx} = -k_B \cdot ln\left(\frac{x_0 - x}{x}\right) \tag{6.4}$$

With a solubility limit of the disordered phase of $x_0 = 0.3$, Reynier[140] found a good agreement between that calculated and the experimental results. However, Equation (6.4) isn't a general form. In some circumstances, it may cause problem when Equation (6.4) is used, such as the reduce of the available lattice for intercalation[23]. Therefore, we used the general form (Equation (6.3)) for the calculation of the Peltier coefficient.

### 6.3.5. The change of the Peltier coefficient during the formation of SEI layers

As mentioned, when a graphite electrode was charged, during the first charging cycle, decomposition of the solvent of the electrolyte occurred and simultaneously SEI layers formed before lithium intercalation. Reports showed that the decomposition of electrolyte and the formation of solid electrolyte interphase layer (SEI layer) occurred around 0.8 V [137]. Several possible reactions for the formation of SEI layers are listed[88]:

$$\begin{aligned}
2\,EC + 2\,Li^+ + 2\,e^- &\longrightarrow (CH_2OCO_2Li)_2 + C_2H_4 \\
Li_2O + EC &\longrightarrow LiOCH_2CH_2OCO_2Li \\
RO^- + EC + Li^+ &\longrightarrow ROCH_2CH_2OCO_2Li \\
RO^- + ROCH_2CH_2OCO_2Li+ &\longrightarrow ROCH_2CH_2OR + CO_3^{2-} + Li^+ \\
EC + 2\,e^- + Li^+ &\longrightarrow C_2H_4 + CO_3^{2-} + Li^+
\end{aligned} \tag{6.5}$$

Figure 6.27 demonstrates an increase of the Peltier coefficient for a graphite electrode during the formation of SEI layers between 0.8 V to 0.3 V. A Peltier coefficient can be measured only when reversible reactions are measured. Therefore, there should be reversible reactions during the formation of SEI layers. In addition, Schmid argued that there was cooling effect when a graphite was charged from 0.8 V to 0.3 V , which might be due to reversible reactions, since irreversible reaction only caused warming effect[23].

Future endeavors are the identification and mechanism studies of the reversible reactions for the formation of the SEI layers.

## 6.4. Conclusion and outlook

In this chapter, the reaction entropy for lithium intercalation in graphite was determined with the help of a microcalorimeter. By a combination of galvanostatic measurement and microcalorimetric measurement, it's possible to obtain the reaction entropy for lithium intercalation at various open-circuit voltages, which corresponded to different state of charge of graphite working electrode.

The Peltier coefficient (i.e. the molar heat) was obtained for both the charging and discharging of Li-graphite half cell. The molar exchanged heat was found to change linearly on the average with the open circuit voltage between 0.3 V to 0.07 V. The slope for the curve of the molar heat vs. open circuit voltage was close to the Faraday constant. When the contribution of enthalpy was neglected because of its small value, the relation between the change of reaction entropy $\Delta\Delta_R S$ and the change of open circuit voltage $\Delta E$ was found to be $\Delta E \approx \frac{T \cdot \Delta\Delta_R S}{F}$.

Phase transitions of the co-existing staged phases in graphite working electrodes were found during charging and discharging of graphite electrode, which agreed with the work of Heß[136] and Dahn[118]. The reversible heat for the phase transitions were determined by pulses measurement with microcalorimeter, which corresponded to the contribution of reaction enthalpy during phase transitions (the free enthalpy $\Delta G = 0$).

The change of reaction entropy was interpreted with lattice-gas model, where the graphite layers were treated as lattice and lithium atoms as lattice gas. Within this model, the reaction entropy for statistical intercalation of lithium was regarded as the molar entropy of mixing. When the state of charge was between 20% and 50%, the change of reaction entropy, obtained from experiment, was of the same order of magnitude with the calculated results based on lattice-gas model. Since there was phase transition of ordered phases between stage 2 and stage 1 when the stage of charge was between 50% and 100%, lattice-gas model was not applicable in this range[23]. When the stage of charge of graphite electrode was below 20%, the experimental results were larger than the calculated results based on the lattice-gas model. This indicated that some side reaction, such as the formation of SEI layers, might occurred during lithium intercalation. Since a good reproducibility was found for the reaction entropy of the first and the second cycle, there was still the formation of SEI layers after the first cycle and some reversible processed might be involved in the formation of SEI layers.

During the formation of SEI layers, a cooling effect on the graphite electrode was found, which also indicated some reversible reactions were involved, since an irreversible only

cause warming effect of the electrode. To study the reversible processes during the formation of SEI layers, more research is needed.

# 7. Summary

In this work, we studied the concentration effects on the reaction entropy of electrochemical Al and Li deposition and the reaction entropy of phase transitions during lithium intercalation/deintercalation in graphite. In addition to potentiostatic and galvanostatic measurements, information of heat evolution and entropy change during electrode reaction is also important for the understanding of the mechanism of energy storage devices.

The change of reaction entropy was measured with an electrochemical microcalorimeter in a glove box. With this microcalorimeter, it was possible to conduct both potentiostatic/galvanostatic measurements and measurements of temperature change during an electrode reaction with a conversion of submonolayer.

Firstly, aluminium deposition was conducted in $AlCl_3$/1-Butyl-3-methylimidazolium chloride (BMIMCl) ionic liquids with different ratio of $AlCl_3$ to BMIMCl (from 1.1:1 to 1.7:1). The Peltier coefficient for aluminum deposition/dissolution process was about 10 kJ/mol (corresponding reaction entropy: 33 J/(mol K)) when the ratio of $AlCl_3$ to BMIMCl was 1.7:1. It demonstrated cooling effect for aluminium deposition and warming effect for aluminium dissolution. As the ratio of $AlCl_3$ to BMIMCl decreased, the Peltier coefficient and corresponding reaction entropy for the aluminium deposition decreased. The change of reaction entropy could be partly due to the dilution entropy. Other contribution, such as the adsorption of ions on working electrode, might be involved.

Secondly, we studied the concentration effects on the reaction entropy of lithium deposition using $LiPF_6$ ($EC : DMC = 1 : 1$) with different concentration (0.01 M, 0.1 M and 1 M) as electrolyte. As the concentration of the $LiPF_6$ electrolyte decreased, the corresponding Peltier coefficient and reaction entropy decreased accordingly. The decrease of the Peltier coefficient for lithium deposition with the decrease of concentration of $LiPF_6$ mainly resulted from the entropy change of the solvated $Li^+$ ion upon dilution. The change of Peltier coefficient was about 5 kJ/mol when the dilution factor was 10 and 10 kJ/mol when the dilution factor was about 100. We neither expected strong changes of the activity coefficient nor of the inner shell coordination number of the $Li^+$ ions among the investigated $Li^+$ concentrations. Furthermore, although the formation of ion contact pairs has been reported for electrolytes similar to the one used in this study, we find no evidence of changes in the solvation entropy for lithium ions. This suggests that ion contact pairs are similarly solvated as lithium ions from $Li^+$ concentrations of 1 M to 0.01 M.

With lithium deposition in 1 M $LiPF_6$ ($EC : DMC = 1 : 1$) as a calibration reaction, we studied the Peltier coefficient and reaction entropy of lithium intercalation/deintercalation during the charging and discharging of lithium-graphite half cells. The reversible heat was found to change linearly on the average (between 0.3 V to 0.07 V). The slope for the curve of the reversible heat vs. open circuit voltage was close to the Faraday constant. When the contribution of enthalpy was neglected because of its small value, the relation between the change of reaction entropy $\Delta\Delta_R S$ and the change of open circuit voltage $\Delta E$ was found to be $\Delta E \approx \frac{T \cdot \Delta\Delta_R S}{F}$. Phase transitions of the co-existing staged phases in graphite were found during charging and discharging of graphite electrode, which agreed with the work of Heß[136] and Dahn[118]. The reversible heat and the reaction entropy for the phase transitions were determined by pulse measurements with microcalorimeter, which corresponded to the contribution of reaction enthalpy during phase transitions.

The change of reaction entropy was interpreted with a lattice-gas model, where the graphite layers were treated as lattice and lithium atoms as the lattice gas. Within this model, the reaction entropy for statistical intercalation of lithium was regarded as the molar entropy of mixing. When the state of charge was between 20% and 50%, the change of reaction entropy, obtained from experiment, was of the same order of magnitude as the calculated results based on the lattice-gas model. Since there was a phase transition of ordered phases between stage 2 and stage 1 when the stage of charge was between 50% and 100%, the lattice-gas model was not applicable in this range[23]. When the stage of charge of the graphite electrode was below 20%, the experimental entropy was larger than the calculated results based on the lattice-gas model. This indicated that some side reaction, such as the formation of SEI layers, might have occurred during lithium intercalation. Since a good reproducibility was found for the reaction entropy of the first and the second cycle, there was still the formation of SEI layers after the first cycle and some reversible processes might be involved in the formation of SEI layers. During the formation of SEI layers, a cooling effect on the graphite electrode was found, which also indicated that some reversible reactions occurred, since an irreversible one would only cause a warming effect of the electrode. To study the reversible processes during the formation of SEI layers, more research is needed.

# A. Bibliography


[1] J. M. Tarascon and M. Armand. Issues and challenges facing rechargeable lithium batteries. *Nature*, 414(6861):359–367, 2001.

[2] H Takeshita. Portable Li-ion, worldwide. In *Proc. Conf. Power*, 2000.

[3] Yoshio Nishi. Lithium ion secondary batteries; past 10 years and the future. *Journal of Power Sources*, 100(1-2):101–106, 2001.

[4] Gints Kucinskis, Gunars Bajars, and Janis Kleperis. Graphene in lithium ion battery cathode materials: A review. *Journal of Power Sources*, 240:66 – 79, 2013.

[5] Hao Sun, Ye Zhang, Jing Zhang, Xuemei Sun, and Huisheng Peng. Energy harvesting and storage in 1D devices. *Nature Reviews Materials*, 2:17023, 2017.

[6] Christopher L. Berhaut, Patrice Porion, Laure Timperman, Grégory Schmidt, Daniel Lemordant, and Mériem Anouti. LiTDI as electrolyte salt for Li-ion batteries: transport properties in EC/DMC. *Electrochimica Acta*, 180:778–787, 2015.

[7] Atetegeb Meazah Haregewoin, Aselefech Sorsa Wotango, and Bing-Joe Hwang. Electrolyte additives for lithium ion battery electrodes: progress and perspectives. *Energy & Environmental Science*, 9(6):1955–1988, 2016.

[8] E. Peled, C. Menachem, D. BarTow, and A. Melman. Improved graphite anode for lithium ion batteries chemically. *Journal of The Electrochemical Society*, 143(1): L4–L7, 1996.

[9] Yoshio Masaki, Wang Hongyu, and Fukuda Kenji. Spherical carbon-coated natural graphite as a lithium-ion battery-anode material. *Angewandte Chemie*, 115(35): 4335–4338, 2003.

[10] G. Cohn, L. Ma, and L. A. Archer. A novel non-aqueous aluminum sulfur battery. *Journal of Power Sources*, 283:416–422, 2015.

[11] Stephen Tait and RA Osteryoung. Infrared study of ambient-temperature chloroaluminates as a function of melt acidity. *Inorganic Chemistry*, 23(25):4352–4360, 1984.

[12] CJ Dymek Jr, JS Wilkes, M-A Einarsrud, and HA Øye. Spectral identification of $Al_3Cl_{10}$ in 1-methyl-3-ethylimidazolium chloroaluminate molten salt. *Polyhedron*, 7 (13):1139–1145, 1988.

[13] S Takahashi, LA Curtiss, D Gosztola, N Koura, and Marie-Louise Saboungi. Molecular orbital calculations and raman measurements for 1-ethyl-3-methylimidazolium chloroaluminates. *Inorganic Chemistry*, 34(11):2990–2993, 1995.

[14] S Takahashi, K Suzuya, S Kohara, N Koura, LA Curtiss, and M-L Saboungi. Structure of 1-ethyl-3-methylimidazolium chloroaluminates: Neutron diffraction measurements and ab initio calculations. *Zeitschrift für Physikalische Chemie*, 209(2): 209–221, 1999.

[15] Z. L. Zhang, M. H. Zhong, F. M. Liu, F. P. Zhong, and F. Wu. In-situ study of charge and discharge of Ni-MH battery using the combined method of electrochemistry and microcalorimetry. *Journal of Thermal Analysis and Calorimetry*, 58(2):413–419, 1999.

[16] M. M. Huie, D. C. Bock, L. Wang, A. C. Marschilok, K. J. Takeuchi, and E. S. Takeuchi. Lithiation of magnetite ($Fe_3O_4$): Analysis using isothermal microcalorimetry and operando X-ray absorption spectroscopy. *Journal of Physical Chemistry C*, 122(19):10316–10326, 2018.

[17] S. L. Glazier, L. E. Downie, J. Xia, A. J. Louli, and J. R. Dahn. Effects of fluorinated carbonate solvent blends on high voltage parasitic reactions in lithium ion cells using OCV isothermal microcalorimetry. *Journal of the Electrochemical Society*, 163(10): A2131–A2138, 2016.

[18] D. S. Hall, S. L. Glazier, and J. R. Dahn. Isothermal microcalorimetry as a tool to study solid-electrolyte interphase formation in lithium-ion cells. *Physical Chemistry Chemical Physics*, 18(16):11383–11390, 2016.

[19] L. E. Downie and J. R. Dahn. Determination of the voltage dependence of parasitic heat flow in lithium ion cells using isothermal microcalorimetry. *Journal of the Electrochemical Society*, 161(12):A1782–A1787, 2014.

[20] Y. F. Reynier, R. Yazami, and B. Fultz. Thermodynamics of lithium intercalation into graphites and disordered carbons. *Journal of the Electrochemical Society*, 151 (3):A422–A426, 2004.

[21] X. F. Zhang, Y. Zhao, Y. Patel, T. Zhang, W. M. Liu, M. Chen, G. J. Offer, and Y. Yan. Potentiometric measurement of entropy change for lithium batteries. *Physical Chemistry Chemical Physics*, 19(15):9833–9842, 2017.

[22] P. J. Osswald, M. del Rosario, J. Garche, A. Jossen, and H. E. Hoster. Fast and accurate measurement of entropy profiles of commercial lithium-ion cells. *Electrochimica Acta*, 177:270–276, 2015.

[23] Matthias Schmid. *Wärmeeffekte bei der Lithiumabscheidung und -interkalation - Mikrokalorimetrische Untersuchungen zur Reaktionsentropie in Lithium/Graphit-Halbzellen*. PhD thesis, Institut für Physikalische Chemie (IPC), 2014.

[24] Hubert H Girault. The water/oil/water thermocouple and the ionic Seebeck effect. *Journal of the Chemical Society, Faraday Transactions 1: Physical Chemistry in Condensed Phases*, 84(6):2147–2154, 1988.

[25] Franz X. Eder. *Arbeitsmethoden der Thermodynamik*. Springer-Verlag Berlin Heidelberg, 1981.

[26] H. Helmholtz. Die Thermodynamik chemischer Vorgänge. *Sitzungsberichte der Königlich Preussischen Akademie der Wissenschaften zu Berlin*, 1:22–39, 1882.

[27] J. W. Gibbs. On the equilibrium of heterogeneous substances. *Transactions of the Conneticut Academy of Arts and Sciences*, 3(10):343–524, 1878.

[28] Carl Wagner. Über die thermodynamische Behandlung stationärer Zustände in nicht isothermen Systemen. *Annalen der Physik*, 395(5):629–687, 1929.

[29] Carl Wagner. Über die thermodynamische Behandlung stationärer Zustände in nicht isothermen Systemen II Berichtigung und Ergänzung. *Annalen der Physik*, 398(3):370–390, 1930.

[30] E. Lange and Th Hesse. Concerning the existence of the so-called heats of transfer (Q* values) in Peltier heats. *Journal of the American Chemical Society*, 55(2): 853–855, 1933.

[31] E. Lange and K. P. Miscenko. Zur Thermodynamik der Ionensolvatation. *Zeitschrift für Physikalische Chememie Abt. A*, 149:1, 1930.

[32] Philippe Boudeville. Thermometric determination of electrochemical Peltier heat (thermal effect associated with electron transfer) of some redox couples. *Inorganica Chimica Acta*, 226(1):69 – 78, 1994.

[33] Philippe Boudeville and Andre Tallec. Electrochemistry and calorimetry coupling: IV. determination of electrochemical Peltier heat. *Thermochimica Acta*, 126(0): 221–234, 1988.

[34] Toru Ozeki, Iwao Watanabe, and Shigero Ikeda. The application of the thermistor-electrode to Peltier heat measurement. *Journal of Electroanalytical Chemistry and Interfacial Electrochemistry*, 96(1):117–121, 1979.

[35] M. F.-M. Raoult. Recherches sur les forces électromotrices. *Annales de Chimie et de Physique*, 4:246–469, 1865.

[36] Julius Thomsen. Chemische Energie und electromotorische Kraft verschiedener galvanischer Combinationen. *Annalen der Physik*, 247(10):246–269, 1880.

[37] M. E. Bouty. Sur un phénomène analogue au phénomène de Peltier. *Journal de Physique Théorique et Appliquée*, 8(1):341–346, 1879.

[38] E. Lange and J. Monheim. Über elektrolytische Peltier-Wärmen und ihre Messung mittels isotherm-adiabatischer Differentialcalorimetrie. *Zeitschrift für physikalische Chemie Abt. A*, 150(3/4):177–202, 1930.

[39] J. M. Sherfey and Abner Brenner. Electrochemical calorimetry. *Journal of the Electrochemical Society*, 105(11):665–672, 1958.

[40] J. M. Sherfey. Calorimetric determination of half-cell entropy changes. *Journal of The Electrochemical Society*, 110(3):213–221, 1963.

[41] Stefan Frittmann, Vadym Halka, and Rolf Schuster. Identification of non-faradaic processes by measurement of the electrochemical Peltier heat during the silver underpotential deposition on Au(111). *Angewandte Chemie International Edition*, 55 (15):4688–4691, 2016.

[42] Matthias J. Schmid, Katrin R. Bickel, Petr Novák, and Rolf Schuster. Mikrokalorimetrische Messung des Lösungsmittelbeitrags zur Entropieänderung bei der elektrochemischen Lithiumvolumenabscheidung. *Angewandte Chemie*, 125(50):13475–13479, 2013.

[43] PW Atkins. *Physical chemistry 5th ed.* Oxford University Press, Oxford, 1994.

[44] J. N. Agar. *Thermogalvanic Cells*, volume 3. Interscience Publishers, London, 1963.

[45] Allen J. Bard and Larry R. Faulkner. *Electrochemical Methods*. Wiley, New York, 2001.

[46] J. Michael Gottfried and Rolf Schuster. Surface microcalorimetry. In Klaus Wandelt, editor, *Surface and Interface Science*, pages 73–126. Wiley-VCH Verlag GmbH & Co. KGaA, Weinheim, Germany, 2016.

[47] M. P. Mercer, S. Finnigan, D. Kramer, D. Richards, and H. E. Hoster. The influence of point defects on the entropy profiles of lithium ion battery cathodes: a lattice-gas Monte Carlo study. *Electrochimica Acta*, 241:141–152, 2017.

[48] Wandelt Klaus and Andrea Vezzoli. Surface and interface science. Volume 5: Solid–gas interfaces I/Volume 6: Solid–gas interfaces II. *Chromatographia*, 81(1):171–171, Jan 2018.

[49] E. D. Eastman. Thermodynamics of non-isothermal systems. *Journal of the American Chemical Society*, 48(6):1482–1493, 1926.

[50] T. Ozeki, N. Ogawa, K. Aikawa, I. Watanabe, and S. Ikeda. Thermal analysis of electrochemical reactions: Influence of electrolytes on Peltier heat for Cu(0)/Cu(II) and Ag(0)/Ag(I) redox systems. *Journal of Electroanalytical Chemistry and Interfacial Electrochemistry*, 145(1):53–65, 1983.

[51] E. D. Eastman. Theory of the Soret effect. *Journal of the American Chemical Society*, 50(2):283–291, 1928.

[52] Katrin R. Bickel, Kai D. Etzel, Vadym Halka, and Rolf Schuster. Microcalorimetric determination of heat changes caused by overpotential upon electrochemical Ag bulk deposition. *Electrochimica Acta*, 112:801 – 812, 2013.

[53] Kai D. Etzel, Katrin R. Bickel, and Rolf Schuster. A microcalorimeter for measuring heat effects of electrochemical reactions with submonolayer conversions. *Review of Scientific Instruments*, 81(3):034101, 2010.

[54] Wenquan Lu, Hui Yang, and Jai Prakash. Determination of the reversible and irreversible heats of $LiNi_{0.8}Co_{0.2}O_2$/mesocarbon microbead Li-ion cell reactions using isothermal microcalorimetery. *Electrochimica Acta*, 51(7):1322–1329, 2006.

[55] Y. Saito, K. Kanari, K. Takano, and T. Masuda. A calorimetric study on a cylindrical type lithium secondary battery by using a twin-type heat conduction calorimeter. *Thermochimica Acta*, 296(1-2):75–85, 1997.

[56] Y. Kobayashi, H. Miyashiro, K. Kumai, K. Takei, T. Iwahori, and I. Uchida. Precise electrochemical calorimetry of $LiCoO_2$/graphite lithium-ion cell. *Journal of The Electrochemical Society*, 149(8):A978–A982, 2002.

[57] Yasuhisa Maeda. Thermal behavior on graphite due to electrochemical intercalation. *Journal of The Electrochemical Society*, 137(10):3047–3052, 1990.

[58] W. R. McKinnon and et al. Entropy of intercalation compounds. II. Calorimetry of electrochemical cells of the Chevrel compound $Li_xMo_6Se_8$ for $0 \leq x \leq 4$. *Journal of Physics C: Solid State Physics*, 19(26):5135, 1986.

[59] Rolf Schuster. Electrochemical microcalorimetry at single electrodes. *Current Opinion in Electrochemistry*, 1(1):88 – 94, 2017.

[60] Stefan Frittmann. *Der Einfluss der Anionen auf die elektrochemische Silber- und Kupfer-Abscheidung auf Au(111) - Mikrokalorimetrische Untersuchungen zur Identifikation ladungsneutraler Adsorptionsprozesse*. PhD thesis, Karlsruher Institut für Technologie (KIT), 2017.

[61] Kwan Chi Kao. *Dielectric Phenomena in Solids*. Elsevier Academic Press, 2004.

[62] SB Lang. Sourcebook of pyroelectricity (Gordon and Breach, New York, 1974). *Google Scholar*, page 74, 2010.

[63] Eustace L Dereniak and Glenn D Boreman. *Infrared detectors and systems*. Wiley, 1996.

[64] S Efthymiou and K B Ozanyan. Pulsed performance of pyroelectric detectors. *Journal of Physics: Conference Series*, 178(1):012044, 2009.

[65] Andrew P. Abbott, Fulian Qiu, Hadi M. A. Abood, M. Rostom Ali, and Karl S. Ryder. Double layer, diluent and anode effects upon the electrodeposition of aluminium from chloroaluminate based ionic liquids. *Physical Chemistry Chemical Physics*, 12 (8):1862–1872, 2010.

[66] M. Armand and J. M. Tarascon. Building better batteries. *Nature*, 451:652, 2008.

[67] Qingfeng Li and Niels J Bjerrum. Aluminum as anode for energy storage and conversion: a review. *Journal of Power Sources*, 110(1):1–10, 2002.

[68] Meng-Chang Lin, Ming Gong, Bingan Lu, Yingpeng Wu, Di-Yan Wang, Mingyun Guan, Michael Angell, Changxin Chen, Jiang Yang, Bing-Joe Hwang, and Hongjie Dai. An ultrafast rechargeable aluminium-ion battery. *Nature*, 520(7547):324–328, 2015.

[69] Xingwen Yu and Arumugam Manthiram. Electrochemical energy storage with a reversible nonaqueous room-temperature aluminum-sulfur chemistry. *Adv. Energy Mater.*, page Ahead of Print, 2017.

[70] Endres Frank. Ionic liquids: Solvents for the electrodeposition of metals and semiconductors. *ChemPhysChem*, 3(2):144–154, 2002.

[71] HA Oye, M Jagtoyen, T Oksefjell, and JS Wilkes. Vapour pressure and thermodynamics of the system 1-methyl-3-ethyl-imidazolium chloride-aluminium chloride. In *Materials Science Forum*, volume 73, pages 183–190. Trans Tech Publ, 1991.

[72] S. Takahashi, N. Koura, S. Kohara, M. L. Saboungi, and L. A. Curtiss. Technological and scientific issues of room-temperature molten salts. *Plasmas & Ions*, 2(3–4):91–105, 1999.

[73] T Jiang, MJ Chollier Brym, G Dubé, A Lasia, and GM Brisard. Electrodeposition of aluminium from ionic liquids: Part I—electrodeposition and surface morphology of aluminium from aluminium chloride $AlCl_3$-1-ethyl-3-methylimidazolium chloride ([EMIm]Cl) ionic liquids. *Surface and Coatings Technology*, 201(1-2):1–9, 2006.

[74] John S Wilkes, Joseph A Levisky, Robert A Wilson, and Charles L Hussey. Dialkylimidazolium chloroaluminate melts: a new class of room-temperature ionic liquids for electrochemistry, spectroscopy and synthesis. *Inorganic Chemistry*, 21 (3):1263–1264, 1982.

[75] M. J. Schmid, J. Xu, J. Lindner, P. Novak, and R. Schustert. Concentration effects on the entropy of electrochemical lithium deposition: Implications for $Li^+$ solvation. *Journal of Physical Chemistry B*, 119(42):13385–13390, 2015.

[76] Chiara Ferrara, Valentina Dall'Asta, Vittorio Berbenni, Eliana Quartarone, and Piercarlo Mustarelli. Physicochemical characterization of $AlCl_3$–1-ethyl-3-methylimidazolium chloride ionic liquid electrolytes for aluminum rechargeable batteries. *The Journal of Physical Chemistry C*, 121(48):26607–26614, 2017.

[77] S. Takahashi, N. Koura, S. Kohara, M. L. Saboungi, and L. A. Curtiss. Technological and scientific issues of room-temperature molten salts. *Plasmas and Ions*, 2(3–4): 91–105, 1999.

[78] Philipp Keil and Axel König. Enthalpies of solution of 1-ethyl-3-methyl-imidazolium chloride and aluminum chloride in molten chloroaluminate ionic liquids. *Thermochimica Acta*, 524(1):202–204, 2011.

[79] L Bai and BE Conway. Complex behavior of Al dissolution in non-aqueous medium as revealed by impedance spectroscopy. *Journal of the Electrochemical Society*, 137 (12):3737–3747, 1990.

[80] Peipei Huang, Patrick C. Howlett, and Maria Forsyth. Electrochemical etching of AA5083 aluminium alloy in trihexyl(tetradecyl)phosphonium bis(trifluoromethylsulfonyl)amide ionic liquid. *Corrosion Science*, 80:120 – 127, 2014.

[81] QX Liu, S Zein El Abedin, and F Endres. Electroplating of mild steel by aluminium in a first generation ionic liquid: A green alternative to commercial Al-plating in organic solvents. *Surface and Coatings Technology*, 201(3-4):1352–1356, 2006.

[82] Katrin Regine Bickel. *Mikrokalorimetrische Untersuchungen elektrochemisch induzierter Adsorptions- und Abscheidungsprozesse von Ionen, Komplexen und Amphiphilen*. PhD thesis, Karlsruher Institut für Technologie, 2012.

[83] Michael Angell, Chun-Jern Pan, Youmin Rong, Chunze Yuan, Meng-Chang Lin, Bing-Joe Hwang, and Hongjie Dai. High coulombic efficiency aluminum-ion battery using an $AlCl_3$-urea ionic liquid analog electrolyte. *Proceedings of the National Academy of Sciences*, 114(5):834–839, 2017.

[84] P.K. Lai and M. Skyllas-Kazacos. Aluminium deposition and dissolution in aluminium chloride—n-butylpyridinium chloride melts. *Electrochimica Acta*, 32(10):1443 – 1449, 1987.

[85] P. K. Lai and M. Skyllas-Kazacos. Electrodeposition of aluminium in aluminium chloride/1-methyl-3-ethylimidazolium chloride. *Journal of Electroanalytical Chemistry and Interfacial Electrochemistry*, 248(2):431–440, 1988.

[86] Rakesh K. Jain, Harish C. Gaur, and Barry J. Welch. Chronopotentiometry: A review of theoretical principles. *Journal of Electroanalytical Chemistry and Interfacial Electrochemistry*, 79(2):211 – 236, 1977.

[87] K. Xu. Electrolytes and interphases in Li-ion batteries and beyond. *Chem. Rev.*, 114:11503, 2014.

[88] D. Aurbach, Y. Talyosef, B. Markovsky, E. Markevich, E. Zinigrad, L. Asraf, J. S. Gnanaraj, and H.-J. Kim. Design of electrolyte solutions for Li and Li-ion batteries: A review. *Electrochim. Acta*, 50:247, 2004.

[89] Z. Wang, B. Huang, R. Xue, L. Chen, and X. Huang. Ion association and solvation studies of $LiClO_4$/ethylene carbonate electrolyte by Raman and infrared spectroscopy. *J. Electrochem. Soc.*, 145:3346, 1998.

[90] M. Castriota, E. Cazzanelli, I. Nicotera, L. Coppola, C. Oliviero, and G. A. Ranieri. Temperature dependence of lithium ion solvation in ethylene carbonate–$LiClO_4$ solutions. *J. Chem. Phys.*, 118:5537, 2003.

[91] O. O. Postupna, Y. V. Kolesnik, O. N. Kalugin, and O. V. Prezhdo. Microscopic structure and dynamics of $LiBF_4$ solutions in cyclic and linear carbonates. *J. Phys. Chem. B*, 115:14563, 2011.

[92] X. Bogle, R. Vazquez, S. Greenbaum, A. v. W. Cresce, and K. Xu. Understanding $Li^+$ solvent interaction in nonaqueous carbonate electrolytes with 170 NMR. *J. Phys. Chem. Lett.*, 4:1664, 2013.

[93] K. Tasaki, K. Kanda, S. Nakamura, and M. Ue. Decomposition of $LiPF_6$ and stability of $PF_5$ in Li-ion battery electrolytes: Density functional theory and molecular dynamics studies. *J. Electrochem. Soc.*, 150:A1628, 2003.

[94] D. M. Seo, S. Reininger, M. Kutcher, K. Redmond, W. B. Euler, and B. L. Lucht. Role of mixed solvation and ion pairing in the solution structure of lithium ion battery electrolytes. *J. Phys. Chem. C*, 119:14038, 2015.

[95] M. Salomon and E. Plichta. Conductivities and ion association of 1:1 electrolytes in mixed aprotic solvents. *Electrochim. Acta*, 28:1681, 1983.

[96] A. V. Cresce and K. Xu. Preferential solvation of $Li^+$ directs formation of interphase on graphitic anode. *Electrochem. Solid-State Lett.*, 14:A154, 2011.

[97] Stefan Frittmann and Rolf Schuster. Role of anions during the Cu underpotential deposition on Au(111): A microcalorimetric investigation. *The Journal of Physical Chemistry C*, 120(38):21522–21535, 2016.

[98] Perla B Balbuena and Yixuan Wang. *Lithium-ion batteries: solid-electrolyte interphase*. Imperial college press, 2004.

[99] Zhiyuan Zeng, Wen-I Liang, Hong-Gang Liao, Huolin L. Xin, Yin-Hao Chu, and Haimei Zheng. Visualization of electrode–electrolyte interfaces in $LiPF_6$/EC/DEC electrolyte for lithium ion batteries via in situ TEM. *Nano Letters*, 14(4):1745–1750, 2014.

[100] WR Torres, AY Tesio, and EJ Calvo. Solvent co-deposition during oxygen reduction on Au in DMSO $LiPF_6$. *Electrochemistry Communications*, 49:38–41, 2014.

[101] L. H. S. Gasparotto, N. Borisenko, N. Bocchi, S. Zein El Abedin, and F. Endres. In situ STM investigation of the lithium underpotential deposition on Au(111) in the air- and water-stable ionic liquid 1-butyl-1-methylpyrrolidinium bis(trifluoromethylsulfonyl)amide. *Phys. Chem. Chem. Phys.*, 11:11140–11145, 2009.

[102] H. Buqa, A. Würsig, J. Vetter, M.E. Spahr, F. Krumeich, and P. Novák. SEI film formation on highly crystalline graphitic materials in lithium-ion batteries. *Journal of Power Sources*, 153(2):385 – 390, 2006.

[103] Yun Jung Lee, Youjin Lee, Dahyun Oh, Tiffany Chen, Gerbrand Ceder, and Angela M Belcher. Biologically activated noble metal alloys at the nanoscale: for lithium ion battery anodes. *Nano letters*, 10(7):2433–2440, 2010.

[104] Huolin L Xin, Julia A Mundy, Zhongyi Liu, Randi Cabezas, Robert Hovden, Lena Fitting Kourkoutis, Junliang Zhang, Nalini P Subramanian, Rohit Makharia, Frederick T Wagner, et al. Atomic-resolution spectroscopic imaging of ensembles of nanocatalyst particles across the life of a fuel cell. *Nano letters*, 12(1):490–497, 2011.

[105] R. A. (Robert Anthony) Robinson and R. H. (Robert Harold) Stokes. *Electrolyte solutions*. London : Butterworths, 2nd ed. rev edition, 1965.

[106] H. Qiao, X. Fang, H. Luan, Z. Zhou, Y. Wu, W. Yao, X. Wang, J. Li, and C Chen. Vibrational spectroscopic and density functional studies on ion solvation and ion association of lithium tetrafluoroborate in 4-methoxymethyl-ethylene carbonate. *J. Mol. Liq.*, 138:69, 2008.

[107] R. Aroca, M. Nazri, G. A. Nazri, A. J. Camargo, and M Trsic. Vibrational spectra and ion-pair properties of lithium hexafluorophosphate in ethylene carbonate based mixed-solvent systems for lithium batteries. *J. Solution Chem.*, 29:1047, 2000.

[108] R. J Blint. Competitive coordination of lithium ion. *J. Electrochem. Soc.*, 144:787, 1997.

[109] M. Morita, Y. Asai, N. Yoshimoto, and M Ishikawa. A raman spectroscopic study of organic electrolyte solutions based on binary solvent systems of ethylene carbonate with low viscosity solvents which dissolve different lithium salts. *J. Chem. Soc., Faraday Trans.*, 94:3451, 1998.

[110] Y. Yamada, M. Yaegashi, T. Abe, and A Yamada. A superconcentrated ether electrolyte for fast-charging Li-ion batteries. *Chem. Commun.*, 49:11194, 2013.

[111] Y. Yamada, K. Furukawa, K. Sodeyama, K. Kikuchi, M. Yaegashi, Y. Tateyama, and A Yamada. Unusual stability of acetonitrile-based superconcentrated electrolytes for fast-charging lithium-ion batteries. *J. Am. Chem. Soc.*, 136:5039, 2014.

[112] Bernd Fuchsbichler, Christoph Stangl, Harald Kren, Frank Uhlig, and Stefan Koller. High capacity graphite-silicon composite anode material for lithium-ion batteries. *Journal of power sources*, 196(5):2889–2892, 2011.

[113] A Robert Armstrong, Christopher Lyness, Pooja M Panchmatia, M Saiful Islam, and Peter G Bruce. The lithium intercalation process in the low-voltage lithium battery anode $Li_{1+x}V_{1-x}O_2$. *Nature materials*, 10(3):223, 2011.

[114] Christian Julien and Gholam-Abbas Nazri. *Solid state batteries: materials design and optimization*, volume 271. Springer Science & Business Media, 2013.

[115] Pedro A. Derosa and Perla B. Balbuena. A lattice gas model study of lithium intercalation in graphite. *Journal of The Electrochemical Society*, 146(10):3630–3638, 1999.

[116] Eduardo M Perassi and Ezequiel PM Leiva. A theoretical model to determine intercalation entropy and enthalpy: Application to lithium/graphite. *Electrochemistry Communications*, 65:48–52, 2016.

[117] Sumit Konar, Ulrich Häusserman, and Gunnar Svensson. Intercalation compounds from LiH and graphite: Relative stability of metastable stages and thermodynamic stability of dilute stage I-d. *Chemistry of Materials*, 27(7):2566–2575, 2015.

[118] JR Dahn. Phase diagram of $Li_xC_6$. *Physical Review B*, 44(17):9170, 1991.

[119] M Noel and R Santhanam. Electrochemistry of graphite intercalation compounds. *Journal of Power Sources*, 72(1):53–65, 1998.

[120] Tsutomu Ohzuku, Yasunobu Iwakoshi, and Keijiro Sawai. Formation of lithium-graphite intercalation compounds in nonaqueous electrolytes and their application as a negative electrode for a lithium ion (Shuttlecock) cell. *Journal of The Electrochemical Society*, 140(9):2490–2498, 1993.

[121] T. Zheng and J. R. Dahn. Effect of turbostratic disorder in graphitic carbon hosts on the intercalation of lithium. *Synthetic Metals*, 73(1):1–7, 1995.

[122] JE Fischer. Chemical physics of intercalation. *Plenum Press, New York*, pages 59–78, 1987.

[123] S. A. Safran. Phase diagrams for staged intercalation compounds. *Physical Review Letters*, 44(14):937–940, 1980.

[124] M. D. Levi, E. Markevich, C. Wang, and D. Aurbach. Chronoamperometric measurements and modeling of nucleation and growth, and moving boundary stages during electrochemical lithiation of graphite electrode. *Journal of Electroanalytical Chemistry*, 600(1):13–22, 2007.

[125] Atsushi Funabiki, Minoru Inaba, Takeshi Abe, and Zempachi Ogumi. Influence of defects on the phase-boundary movement in a stage transformation of lithium-graphite intercalation compounds. *Carbon*, 37(10):1591–1598, 1999.

[126] Mikhail D. Levi and Doron Aurbach. The mechanism of lithium intercalation in graphite film electrodes in aprotic media. part 1. high resolution slow scan rate cyclic voltammetric studies and modeling. *Journal of Electroanalytical Chemistry*, 421(1):79 – 88, 1997.

[127] Victor V. Avdeev, Alevtina P. Savchenkova, Ludmila A. Monyakina, Irina V. Nikol'skaya, and Alexey V. Khvostov. Intercalation reactions and carbide formation in graphite-lithium system. *Journal of Physics and Chemistry of Solids*, 57(6):947–949, 1996.

[128] J. S. Filhol, C. Combelles, R. Yazami, and M. L. Doublet. Phase diagrams for systems with low free energy variation: a coupled theory/experiments method applied to Li-graphite. *The Journal of Physical Chemistry C*, 112(10):3982–3988, 2008.

[129] Yujie Zhu and Chunsheng Wang. Galvanostatic intermittent titration technique for phase-transformation electrodes. *The Journal of Physical Chemistry C*, 114(6): 2830–2841, 2010.

[130] Kristin Persson, Yoyo Hinuma, Ying Shirley Meng, Anton Van der Ven, and Gerbrand Ceder. Thermodynamic and kinetic properties of the Li-graphite system from first-principles calculations. *Physical Review B*, 82(12), 2010.

[131] Vikram Pande and Venkatasubramanian Viswanathan. Thermodynamics of lithium intercalation into graphite studied using density functional theory calculations incorporating van der Waals correlation and uncertainty estimation. *Condens. Matter*, pages 1–9, 2016.

[132] Jun-Ichi Yamaki, Minato Egashira, and Shigeto Okada. Potential and thermodynamics of graphite anodes in Li-ion cells. *J. Electrochem. Soc.*, 147(2):460–465, 2000.

[133] Alejandro A. Franco. Multiscale modelling and numerical simulation of rechargeable lithium ion batteries: concepts, methods and challenges. *RSC Adv.*, 3:13027–13058, 2013.

[134] Manuel Landstorfer and Timo Jacob. Mathematical modeling of intercalation batteries at the cell level and beyond. *Chem. Soc. Rev.*, 42:3234–3252, 2013.

[135] Arnulf Latz and Jochen Zausch. Multiscale modeling of lithium ion batteries: thermal aspects. *Beilstein Journal of Nanotechnology*, 6:987–1007, 2015.

[136] M. Heß. *Kinetics of graphite for lithium-ion batteries*. PhD thesis, ETH Zürich, 2013.

[137] Kristina Edstroem, Marie Herstedt, and Daniel P. Abraham. A new look at the solid electrolyte interphase on graphite anodes in Li-ion batteries. *Journal of Power Sources*, 153(2):380 – 384, 2006.

[138] S. Al Hallaj, R. Venkatachalapathy, J. Prakash, and J. R. Selman. Entropy changes due to structural transformation in the graphite anode and phase change of the $LiCoO_2$ cathode. *Journal of The Electrochemical Society*, 147(7):2432–2436, 2000.

[139] W. Lu and J. Prakash. In situ measurements of heat generation in a Li/mesocarbon microbead half-cell. *Journal of the Electrochemical Society*, 150(3):A262–A266, 2003.

[140] Y. Reynier, R. Yazami, and B. Fultz. The entropy and enthalpy of lithium intercalation into graphite. *J. Power Sources*, 119-121:850–855, 2003.

[141] R. Yazami and Y. Reynier. Thermodynamics and crystal structure anomalies in lithium-intercalated graphite. *Journal of Power Sources*, 153(2):312–318, 2006.

[142] L. Anthony, J. K. Okamoto, and B. Fultz. Vibrational entropy of ordered and disordered $Ni_3Al$. *Phys. Rev. Lett.*, 70:1128–1130, Feb 1993.

[143] Chunsheng Wang, Xiang-wu Zhang, A. John Appleby, Xiaole Chen, and Frank E. Little. Self-discharge of secondary lithium-ion graphite anodes. *Journal of Power Sources*, 112(1):98–104, 2002.

[144] Martin Winter, Jürgen O. Besenhard, Michael E. Spahr, and Petr Novák. Insertion electrode materials for rechargeable lithium batteries. *Advanced Materials*, 10(10): 725–763, 1998.

# B. List of Figures

# C. Applied chemicals

| Name | Formel | Producer | Purity |
|---|---|---|---|
| Acetone | $CH_3COCH_3$ | Merck | p.A. |
| Dimethylcarbonate | $(CH_3O)_2CO$ | Alfa Aesar | 99% |
| Ethylencarbonate | $C_2H_4O_2CO$ | Alfa Aesar | 99% |
| 1-Butyl-3-methylimidazolium chloride | $C_8H_{15}ClN_2$ | Fluka Chemistry | 95% |
| Potassium ferricyanide(II) | $K_4[Fe(CN)_6]$ | Merck | p.A. |
| Potassium ferricyanide(III) | $K_3[Fe(CN)_6]$ | Merck | p.A. |
| LP 30: Lithium-hexafluoro-phosphat in Ethylencarbonate und Dimethyl-carbonate (50:50, weight percent) | $LiPF_6$, $C_2H_4O_2CO$, $(CH_3O)_2CO$ | Merck | battery grade |
| Sulfuric acid, 96% | $H_2SO_4$ | Merck | p.A. |
| Aluminium chloride | $AlCl_3$ | Fluka Chemistry | 99% |
| Hydrogen peroxide, 30% | $H_2O_2$ | Merck | p.A. |

# D. Publications

Schmid, M.J., **Xu, J.**, Lindner, J., Novák, P. and Schuster, R. Concentration Effects on the Entropy of Electrochemical Lithium Deposition: Implications for $Li^+$ Solvation. Journal of Physical Chemistry B, 2015. 119(42): p. 13385-13390.

# E. Acknowledgements

It's a challenge to study abroad and choose a new subject. Without the help of my colleagues and tutor, it would be much harder for me to finish this work. I learned a lot from them in this process.

Firstly, I appreciate the guide of Prof. Dr. Schuster. His patience and wisdom encouraged me to work harder and think more deeply and prudently. In the process of solving both technical and scientific problems, I obtained a lot of improvement.

I appreciate the help of my colleagues: Jeannette, Stefan and Matthias. When I started this work, they help me a lot with great patience in understanding the microcalorimetry method.

For the discussion and the time of working together, I appreciate my colleagues in our group: Alana, Axel, Daniela, Detlef, Janet, Jens, Katrin, Machel, Macro and Martin. It's a great pleasure to work together with them.

Mr. Dieter Waltz and all his colleagues in Mechanical workshop gave me many supports. I appreciate for their excellent work. I also thank Mr. Sebastian Kleinhans and Mr. Klaus Stree for their support of IT and electronic.

Prof. Dr. Petr Novák and Dr. Michael Heß from Paul Scherrer Institute provided graphite electrode in this work. I appreciate for their support and the illuminating discussion.

I appreciate the scholarship from China Scholarship Council, which provided financial support for me living in Germany. And I also appreciate the funding from Physical Chemistry Institute of Condensed Matter Division and Prof. Schuster for supporting me doing research and attending conferences.

I appreciate Huijuan and my parents for their support.